Theoretical investigation of novel binary nitrides M2N3 (M=Ta, Nb, V) as new high-pressure superconductors

Auteur : Dudzinski, Alexandra
Promoteur(s) : Verstraete, Matthieu; 10911
Faculté : Faculté des Sciences
Diplôme : Master en sciences physiques, à finalité approfondie
Année académique : 2019-2020
URI/URL : http://hdl.handle.net/2268.2/9303

Theoretical investigation of novel binary nitrides M_2N_3 (M=Ta, Nb, V) as new high-pressure superconductors

14.06.2020

A thesis submitted by

Alexandra Dudzinski [a,b] · Alexandra.Dudzinski@gmail.com

for obtaining the Master's double diploma of

Master of Physics

Master of Functionalized Advanced Materials Engineering (FAME+)

Supervised by

Andres Cano [a] · andres.cano@neel.cnrs.fr

Matthieu J. Verstraete [b] · matthieu.verstraete@uliege.be

Members of the evaluation panel

Eric Bousquet [b], Peter Schlagheck [b], Stéphane Dorbolo [b]

This is a joint project of the University of Liège, the Insitut Néel (CNRS) and Grenoble INP 2019-2020.

[a] Institut Néel, MCBT Department, TMC Group

[b] Université de Liège, Department of Physics

Abstract

Superconductivity at room temperature is a hundred year old problem of condensed matter physics. Since the recent discovery of SH_3 (200 GPa) and LaH_{10} (300 GPa), conventional superconductors under pressure play a major role in solid state physics. These BCS-superconductors can be described by theoretical tools and can be more and more synthesized experimentally with strenuous efforts. These classes of materials are especially interesting for they display outstanding parameters influencing the critical temperature. The extreme pressures they are synthesized in lead to completely new materials that would otherwise not spontaneously form in ambient pressures.[1] The following work is investigating possible superconducting properties of novel metal-nitrides that can be obtained via high-temperature and high-pressure synthesis techniques. They can be recovered at ambient temperatures with interesting parameters, making them versatile for industrial use. A focus is put on binary transition metal nitrides with the nitrogen to metal ratio 3:2, while a close look is taken on Group 5 metals. This material class does not only display superconductivity but also interesting mechanical properties. For all compounds, structural, electronic and vibrational properties are predicted and they are found to be in good agreement with literature. Firstly, the previously synthesized η-Ta_2N_3 compound is investigated and its experimentally found critical temperature of ≈ 3 K is theoretically confirmed in this work.[2] Similar superconductive parameter are found for the same material at 26.065 GPa. We compare the calculation of superconductive parameters from the software Abinit, which is used to obtain all results, with previous results from Quantum Espresso for the tetragonal Ta_2N_3 and it is found that the superconductive parameters, especially the logarithmic frequency, are generally underestimated with Abinit. It is proposed to calculate the critical temperature with the help of the more accurately calculated Debye-temperature. The tetragonal Ta_2N_3 is predicted to be a very low critical temperature superconductor, while it still might display no superconductivity at all. Furthermore, the orthorhombic Nb_2N_3 is investigated further, its electronic and vibrational parameters are found and it is predicted to have a very high electron phonon coupling that could potentially lead to a superconductivity at 30 K. The last Group 5 metal nitride in question is the V_2N_3. Previously, the instability of the orthorhombic V_2N_3 was found, which is confirmed by us through calculating the phonon dispersion and finding various imaginary frequencies.[3] Its stable trigonal form is investigated, its electronic structure and vibrational properties are discussed in the following. Superconductivity is either not present in this compound or it can be found at very low critical temperatures.

Acknowledgements

I would like to extend my sincere and heartfelt obligation towards all the personages who have helped me in this endeavor. Without their active guidance, help, cooperation and encouragement, I would not have made headway in the project.

First and foremost, I would like to express my sincere gratitude and appreciation for my supervisors Andres Cano at Institut Néel and Matthieu Verstraete at the University of Liège. I want to deeply thank you for introducing me and guiding me through the world of theoretical solid state physics and for showing and helping me with all kinds of questions and problems. The persistent help, remarks, encouragement and guiding majorly impacted a successful competition of this project. I am extremely thankful and indebted to the patience and time they both offered up for me.

Furthermore, I want to thank the members of the evaluation panel, Eric Bousquet, Peter Schlagheck and Stéphane Dorbolo for reading and grading my work.

I am particularly grateful to my loved ones; my mother, my family and my boyfriend for their unfailing support, for their motivation, love and patience showed to me throughout the whole process.

Moreover, I wish to acknowledge my teacher Dr. Paland, who was a main driving force behind me taking on scientific studies. His input in my late school years ignited my deep interest and passion for chemistry, physics and material science.

At last but not least gratitude goes to all of my friends who directly or indirectly not only helped me to complete this master thesis project, but also for making my studying time a wonderful time I will never forget.

The present research benefited from computational resources made available on the Tier-1 supercomputer of the Fédération Wallonie-Bruxelles, infrastructure funded by the Walloon Region under the grant agreement n°1117545. Computational resources have been also provided by the Consortium des Equipements de Calcul Intensif (CECI), funded by FRS-FNRS G.A. 2.5020.11.

I am grateful for my Erasmus+ Erasmus Mundus scholarship, that financed my participation in the FAME+ Master, that is a great, prestigious opportunity I am proud to have pursued.

Contents

1 Introduction

Superconductivity refers to the zero electrical resistance phenomenon displayed by certain materials at finite temperatures.[4] Since Kamerlingh Onnes's 1911 discovery of supraconductivity in mercury with a T_c of 4.2 K, researchers have been working on understanding and developing new superconducting materials. With the finding of the Meissner effect in 1933 describing how superconducting materials exclude external magnetic fields up to a critical magnetic field value, it was clear that superconductivity can't be explained with classical physics. Phenomenological theory of superconductivity emerged (London) and the dependence of the precise atomic masses on the superconductivity described as isotope effect was discovered in 1950.[5] This first clue on how the phonons could play a major role by generating attractive channels for electrons lead then to the BCS-theory in 1957 giving a microscopic picture of superconductivity. BCS-theory describes superconductivity in so called conventional superconductors. Here, pairs of electrons form bosonic Cooper pairs through coupling between electrons and phonons. This theory is the base of the theoretical framework nowadays to predict superconducting parameter like in the following work. Cohen and Anderson postulated in 1972, that the hard limit for the critical temperature of conventional superconductors was 25 K. At that point, there were no theoretical tools to predict superconductivity and the Migdal-Eliashberg theory developed in the 60's was solely a semi-phenomenological method because electron-phonon spectra were just accessible experimentally.[1] After first research around metallic hydrides at ambient pressure lead to no interesting findings around the 70's, the attention was fastly diverted to a new class: The cuprates. This class of unconventional superconductors did not follow the BCS theory but new critical temperatures of up to 145 K with optimal hole-doping could be reached, making superconductivity accessible for technological use because a cooling with liquid nitrogen was enabled.[6] Up until today, these superconductors are used for e.g. MRI, while the reason for their high temperature superconductivity is still not clear. With the development of theoretical tools to predict superconductivity, and especially electron-phonon spectra, Cohen and Anderson's postulates became obsolete end of the 90's. And after the potential of unconventional superconductors, especially cuprates, iron pnictides and chalcogenides, has been thoroughly investigated, the interest on conventional superconductors returned with the discovery of the low cost MgB_2 superconductor (T_c=39 K) in 2001 and Ashcroft returned to previous ideas to find high temperature superconductors through introducing a high content of hydrogen into a material.[1,5] Followed by the development of new synthesis and prediction techniques it was recently possible to access new structures previously unimaginable to produce for they require extreme pressures. This was the beginning of the discovery and race for superconductors synthesized under pressure.

Nowadays, superconductors are used as generators of intense magnetic fields that can be used in particle accelerators, magnetic resonance imaging and superconducting quantum interference devices (SQUIDs). The main limitation is here the extremely low temperatures or extremely high pressures to access the superconducting state of a material. Therefore, finding a superconductor at ambient temperature and pressure is an ongoing quest in physics that has the potential to trigger the development of a series of new technologies playing an important role in improving global energy efficiency.[5]

The following work focuses on nitrides with the stoichiometry M_2N_3, while metals are the V-group metals Tantalum, Niobium and Vanadium. Nitrides themselves are a very interesting group of materials that display high hardness and other attractive mechanical properties for application. E.g. boron nitrides BC_2N, the third hardest material after diamond. One system of interest that will be further explored is the novel superconducting orthorhombic η-Ta_2N_3.

It was recently synthesized under high pressure and high temperature conditions and can be recovered under ambient pressure. Next to the η-Ta_2N_3, a variety of other tantalum nitrides can be synthesized, while the η-Ta_2N_3 is the first Tantalum nitride with a U_2S_3 structure, a variation of the stibnite structure.[7] Structural and mechanical information are reported at ambient pressure showing very low compressibility of the edge-sharing polyhedral structure leading to high rigidity.[8] Furthermore, the η-Ta_2N_3 displays interesting very high hardness. Previous theoretical investigations show the meta stable nature of the η-Ta_2N_3 due to a tetragonal, more favorable, Ta_2N_3 structure.[9] In a preceding work, the superconductivity with a critical temperature of around T_c = 10 K could be predicted for the theoretical tetragonal structure, note that this is just a vague assumption that needs more in-depth theoretical examination and finally, experimental back-up.[10] In the following work, a quick look is taken upon this structure to mainly understand numerical differences because the old results were calculated with Quantum Espresso, while in this work, mainly Abinit is used to gain insights in the superconductivity.[11,12,13,14,15,16,17] The superconductivity of this materials class is based on electron-phonon coupling phenomena firstly described by BCS-theory. This group of superconductors have a high unknown potential for showing very high values for the critical temperature. The critical temperature is anti-proportional to the atomic mass of the participating atoms due to the fact that the frequency of the phonon modes is generally higher for low atomic mass atoms. This is the main motivation why a look will be taken on potential superconductors with the stoichiometry M_2N_3 with M=Ta,Nb,V. The Ta_2N_3 is a known superconductor and after trying to confirm its superconductivity, the heavy Tantalum is substituted by the lighter Niobium and Vanadium. It is of interest to investigate this new material class of superconductors not only because they also consists of the light nitrogen, but also because Nitrides display interesting mechanical properties. These materials were a priori theoretically investigated, predicting the Nb_2N_3 to be orthorhombic, while the stable structure of V_2N_3 is supposed to be trigonal. It is indicated, that these materials are candidates for hard materials and mechanically stable under ambient conditions.[3]

2 Superconductivity under pressure

Scientist have searched for higher critical temperature superconductors starting with elemental materials and then venturing forth towards more complex systems.[18] The superconductors of interest in the following work belong to the group of superconductors under pressure, for their synthesis require high pressures and temperatures, like e.g for the η-Ta_2N_3 a pressure of 11-20 GPa and temperature of 1800–2000 K.[7] In order to understand the trends and reasons in that area of research it is of utmost importance to take a look back at significant discoveries of the last two decades in order to also fully grasp the development of methods explained in the following chapter. A few famous examples are presented in the following to show the highlights of the recent years of superconductivity under pressure. Their structure is shown in figure 2.0.1.

J. A. Flores-Livas, L.Boeri, A.Sanna et al., Physics Reports 856, 2020, 1-78

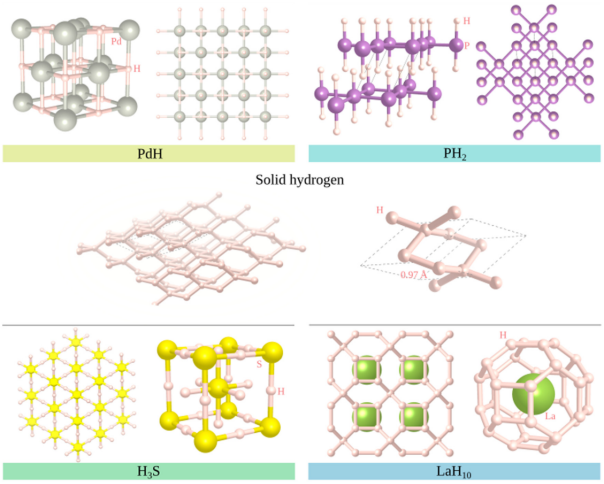

Figure 2.0.1: Examples for structures of superconductors under pressure. PdH is a metal hydride at ambient pressure with a T_c=54 K (0 GPa), PH_2 is a molecular hydride at intermediate pressure (120 GPa), which can reach a maximum T_c=103 K at around 207 GPa. H_3S is a covalently bonded hydride at high pressure reaching T_c=203 K (200 GPa) and the superhydride LaH_{10} shows superconductivity at very high pressures (300 GPa) with a critical temperature at around 260 K. Solid metallic hydrogen in comparison becomes superconducting at megabar pressures of around 400 GPa.[1]

2.1 Superconducting metallic hydrogen

Looking at the BCS-theory as derived in chapter 3.4, high temperature superconductors can be reached through introducing low atomic mass atoms in order to increase the frequency. The lowest mass atom is hydrogen, and its metallic structure under very high pressures was suspected since 1935 by Wigner and Huntington.[19] In 1968, Ashcroft proposed that solid metallic hydrogen could be a high temperature superconductor. Under sufficient high pressures, hydrogen changes from its molecular form into a metallic liquid phase, but for a long time, there was just theoretical predictions of the solid metallic state of hydrogen. Currently, it is widely accepted that a large portion of Jupiter's core is formed by hydrogen in its metallic liquid state. 2017 Dias *et al.*[20] claimed to have produced solid metallic hydrogen at a pressure of 495 GPa at 5.5 K, while the change in reflectance was measured and the carrier density was determined with the help of the Drude free-electron model. Recently, Loubeyre *et al.* reported that when pressurizing a hydrogen sample in a DAC, an abrupt, discontinuous and reversible change in

optical reflectivity can be observed at 425 GPa that indicate the change into a "dense" metallic state, for it is still controversial if measuring the reflectance is enough to prove the solid metallic structure of the hydrogen nor it gives any clue on important properties of the new phase.[21] Although theoretical calculation do lack accuracy due to the large quantum mechanical correction needed in that kind of extreme regimes, there are some that do predict a transition at 500 GPa which leads to a critical temperature around room temperature.[22] Interestingly, following predictions, the critical temperature can rise up to 420 K above 3 TPa.[18] But achieving to obtain the solid state metallic hydrogen superconductor is not sufficient due to the extreme pressures needed to keep the material stable. So researchers started searching potential metallic hydrides that could give a high temperature superconductor.[5] In 2004, Ashcroft suggested that metallic hydrogen could be found chemically in high hydrogen content materials. In 2006, Hoffmann *et al.*[23] proposed to metallize pressurized group 14 hydrides. The hydrogen is supposed to be chemically precompressed in these systems and can then be metallized at lower pressures. Firstly, they predicted a metallization pressure of 91 GPa for SiH_4.[23] After thorough investigation, a more stable semiconducting phase was found in this regime which led to a very low T_c which was confirmed by experiments.[5]

2.2 Sulfur hydride

After many experiments with the goal to find a novel high temperature superconductor failed for various reasons, H_2S was discovered, where the metallization occurred at around 100 GPa in a hydrogen atmosphere.[1] Superconductivity then appeared at around 150 GPa giving a critical temperature of around 8 K. Interestingly, experiments showed that the critical temperature varied not only with the increase in pressure but also with the increase of the temperature, which could be explained through the formation of H_3S, which then can be described as a dense solid of covalently-bonded hydrogen and sulfur.[1] With increasing the pressure, the structure of the H_3S also changes, starting with $Cccm$ (88) or $C2/c$ (49) space group below 112 GPa, changing into a rhombohedral $R3m$ distorted *bcc* structure and ending at a $Im\bar{3}m$ phase above 175 GPa. Taking into account the anharmonicity of the hydrogen phonon modes, the hydrogen bonds are symmetrized at lower pressures and the cubic $Im\bar{3}m$ is even favored beneath 175 GPa. With this knowledge, a new record was set 2015 with reaching a critical temperature of 203 K at around 170 GPa.[1] Several experiments were conducted to characterize the phases correctly and it is found to be a conventional Type-II superconductor with two critical magnetic fields found. Key parameters making the H_3S having a high critical temperature is mainly the hydrogen high frequency vibrational modes and the hydrogen contribution of 45 % of the states at the Fermi level. The short metal hydrogen distances are also much shorter then for other compounds like e.g. the superconducting PdH, leading to a stronger electron-phonon coupling. Noteworthy is also, that elemental sulfur is a high pressure superconductor, enhancing the coupling further. More findings of superconducting hydrides followed like e.g. the metastable PH_n (at 200 GPa T_c = 100K) were reported. Again the stochiometry could not be defined very well.

2.3 Lanthanum hydrides

The next big revelation were the lanthanum hydrides, that still hold the record.[1] Through two different synthesis, two groups obtained this material, while the exact phases and the phase diagram itself is yet to be clarified. Drozdov *et al.*[24] annealed La and H_2 directly in the DAC while Somayazulu *et al.*[25] used BH_3NH_3 as a hydrogen donor. A critical temperature up until 260 K was found at a pressure of 180–200 GPa, while the stochiometries and structures could not be defined properly. A the LaH_{10} ($Fm\bar{3}m$) is most probable based on the volume per formula ratio, some XRD measurements and first principle predictions by Li *et al.*, that previously predicted

a critical temperature of 280 K at 210 GPa, confirmed this suspected structure. Various LaH_n could be found depending on the synthesis procedure with differing critical temperatures.[26] A new class of superhydrides was born to be explored. In this structure, the Lanthanum donates its electrons to a pure metallic hydrogen lattice surrounding. The structure resembles closely to the idea of Ashcroft-Gillans's precompressed hydrogen which can be seen in figure 2.0.1. The critical temperature varies and there is a big disparity between synthesis with deuterium and hydrogen showing a big influence of anharmonic effects that are yet to be explained theoretically. Due to the arduous synthesis which enables a sample size up to 10-20 μm, the Meissner effect could not yet be measured, but the suppression of the magnetic field could be shown.[1] Recently, Grockowiak *et al.* synthetized a lanthanum based superhydride whose critical temperature could rise up to around 500 K through thermal cycling leading to a new record.[18] Like for the sulfur hydride, we can find a high electron-phonon coupling, high frequency phonons that stem from the hydrogen and a comparable electronic DOS.

2.4 Superconducting nitrides

A new class of potential high temperature superconductors could include other light elements like e.g. nitrogen or carbon. These materials show possibility to be stable under ambient pressures and they also combine superconducting behavior with interesting mechanical properties. Noteworthy is the NbN, that has a critical temperature of around 16 K. It shows very high hardness and is therefore tested for applications of e.g. superconducting quantum interference devices, superconducting hot-electron, photo detectors, and IR sensors.[27] With the help of high pressure synthesis, new nitrides can be found and even be recovered at ambient pressures. An example is the novel superconducting orthorhombic η-Ta_2N_3 that is further investigated in this work. It was recently synthesized under high pressure and high temperature conditions and can be recovered under ambient pressure. This new material class is shown to have interesting mechanical properties like an exceptional hardness and high rigidity.[8] Previous theoretical investigations show the meta stable nature of the η-Ta_2N_3 due to a tetragonal, more favorable, Ta_2N_3 structure.[9] Next to the tantalum and niobium hydrides, a variety of other nitrides with a broad range of stoichiometries can be synthesized.[7]

2.5 State of the art

Nowadays, many superconducting high temperature hydrides have been predicted theoretically as shown in figure 2.5.1. Experimental progress is catching up for the experiments require very high pressures and temperatures in order to break the molecular hydrogen bond that makes up a large kinetic barrier. Nevertheless, the experimental development and discovery of the last 10 years is impressive whilst the theoretical and experimental results are often in agreement.[1] One can count around 61 superconducting binary hydrides predicted.[1]
One can also see in figure 2.5.1, that new superhydrides followed the LaH_{10}, like e.g. YH_{10}, while many also experimentally confirmed cases are missing like e.g. ThH_{10} with T_c= 160 K (170-175 GPa)[28] and YH_9 with T_c= 243 K (201 GPa)[29]. These very recent results show how fast the field of superconducting hydrides is growing towards higher values of merit. Conditions that enhance the critical temperature are found to be:[1]

- Light-element electronic states crossing the Fermi-level
- The existence of a extended bonding structure between the light elements and the host
- High phonon mode energies leading to a high electron-phonon coupling

Theoretical understanding still needs to be refined for the structures might differ from the expected. Not only do quantum effects and anharmonicity complicate theoretical predictions but

C. J. Pickard, I. Errea, M. I. Eremets, Annual Review of Condensed Matter Physics 2020,11, 57–76

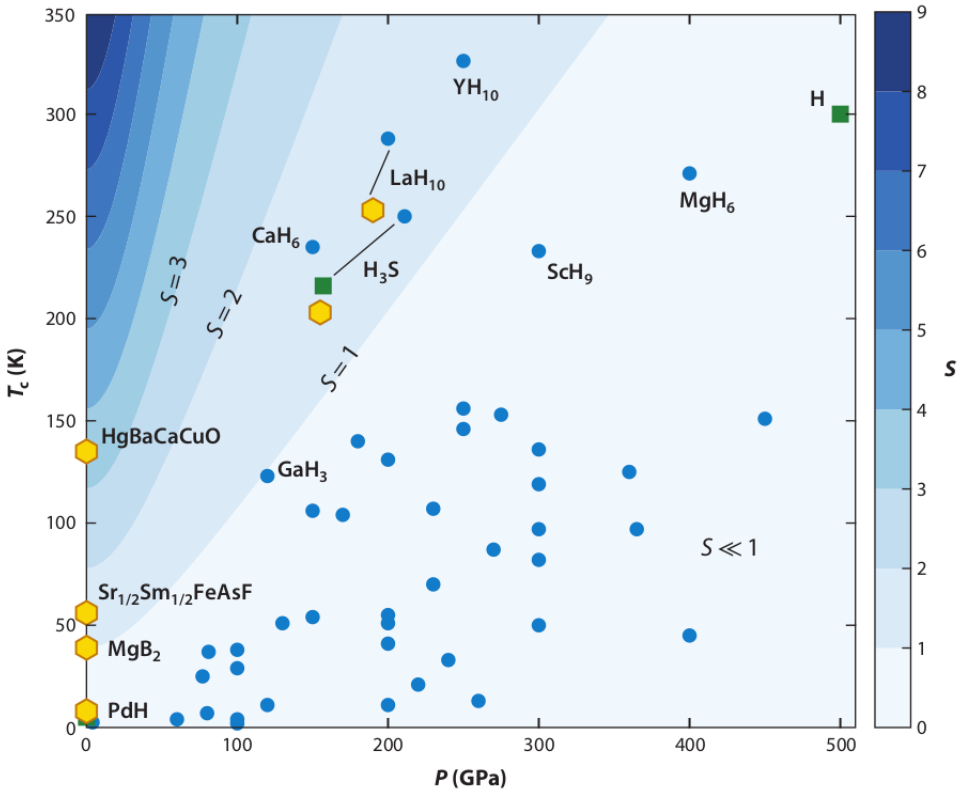

Figure 2.5.1: Critical temperatures of superconducting materials synthesized experimentally (yellow hexagons), predicted theoretically in the harmonic approximation (blue circles) and predicted theoretical including anharmonic effects (green squares) as a function of pressure. The contouring shows the merit S.[5]

also the difficulty to conclude experiments in this extreme conditions can be arduous. Many questions are still unanswered like e.g. if there is an upper limit for the critical temperature for superconductors and if one can quantify it by structural distortion, compositional change, or competition with electronic or magnetic phases while many materials are undiscovered or not synthesized. Furthermore, compounds have to be found that work at not only ambient temperature, but also ambient pressure in order to use them for technological applications. This compromise can be described by the following figure of merit proposed by Pickard *et al.*[5] that is also used in figure 2.5.1:

$$S = \frac{T_c}{\sqrt{T_{c,MgB_2}^2 + P^2}} \tag{2.1}$$

P is here the pressure in giga pascal and the critical temperatures are shown in Kelvin. Assuming a score of 10 would be optimal for terrestrial use, one can see how the highest scale up until now is still taken by the cuprate HgBaCaCuO, discovered by the nobel prize winners Dr Georg Bednorz and Professor Dr K. Alex Müller. One can see here how the critical temperature ($\approx$ 39 K) of the Magnesiumdiboride is used as a reference. Recent research does give a variety of new materials through stochastic search, although the computation of the critical temperature is not yet routine.[5] The potential of superconductors under pressure is vast. Ternary, quaternary and complex hydrides are still to be explored. It is estimated that there can be around 300 binary hydrides as an upper limit while it could be possible to find 1770 ternary hydrides, including 60 elements as possible building blocks. But not only hydrides are of interest, new material classes with other light elements like perovskites, two dimensional materials and ni-

trides could be of interest while doping can also influence the superconductivity.[1] This work is trying to get deeper understanding of another material class, that is the metal nitrides with a ratio of nitrogen to the metal exceeding 4:3. Recently, it is possible to synthesise and find more and more metal nitrides and superconductivity can be found in some of them. What makes them interesting candidates is the fact that they can be recovered in ambient conditions and also the light nitrogen might lead to a high critical temperature.

3 Methodology

One can mention three crucial methods that enabled researchers to find superconductors under pressure. One main method used for experiments, is the the diamond anvil cells (DACs), enabling the complicated high pressure, high temperature synthesis and characterization of the hydrides.[5] And for the theoretical methods, firstly, the random sampling that enables to find the stable state of a material at specific conditions and secondly, the computation of superconducting properties. The interplay between theory and experiments enabled the substantial progress of the last two decades. After shortly explaining the first two important methods bringing research as far as it is now, the focus will be set on the theoretical prediction of superconducting parameters which is also the main goal of this work.

3.1 Experimental tools

Almost in parallel with the rise in maximum critical temperature, one can note a rise in maximum pressure possible to reach experimentally. Therefore, a crucial experimental tool is the diamond anvil cell (DAC), it is used to access ultrahigh compression of a material so one can achieve these high pressures needed. Not only does a state of the art DAC produce the high pressures, it also has build-in characterization tools which can be seen in figure 3.1.1.

J. A. Flores-Livas, L.Boeri, A.Sanna et al., Physics Reports 856, 2020, 1-78

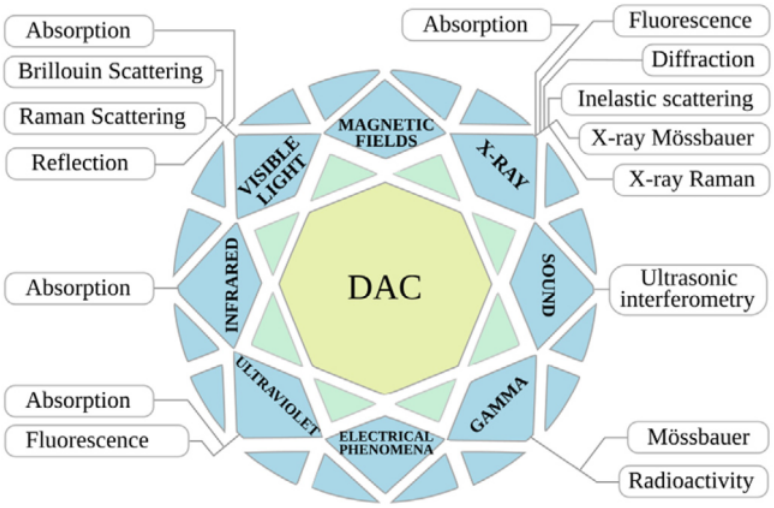

Figure 3.1.1: DAC with in-built characterization tools

Nowadays, it is possible to also synthesize the material *in situ*.[1] The material in question is placed in a thin metal foil between the two diamond anvils. The underlying physical principle is the anti proportionality of the pressure with respect to the area of surface where the force is applied. This also leads to the necessity to work with tiny sample volumes and to have diamond as the hardest material to build the anvils. Another reason to use diamond is its transparency for a wide range of electromagnetic radiation (weak absorption in the IR range, UV up to 220 nm). With their help, researchers have been able to study many materials and elements. It became possible to gain a deep understanding of their properties like e.g. superconductivity. Many molecules or elements become metallic and superconducting under pressure, while with pressure the critical temperature usually rises. Some interesting examples are: O_2 with 0.6 K

at 95 GPa or boron with 11.2 K at 250 GPa. In order to be able to prove superconductivity, the development of the SQUID was essential. This is a superconducting quantum interference device, that can measure very low magnetic fields. They can detect vertices in superconductors whose number grow with applied magnetic field and once their non-superconducting cores overlap, the superconductivity is lost, which occurs in type II superconductors and explains the two critical magnetic fields found and the breakdown of the Meissner effect.[30] In order to get information about the type of superconductor, magnetization experiments are conducted in the diamond anvil cell.

3.2 Theoretical tools

In the following, atomic units are used: $e^2 = \hbar = m = 1$

The main tool at hand is the density functional theory (DFT) and density functional perturbation theory (DFPT) explained in sections 4.3 and 4.4. It is a a first principle method/ab initio method that provides a description of the ground state electronic properties. It enables material-dependent predictions through mapping complex many-body problems of interacting particles in an external potential onto a system of non-interacting particles.[31] The two main theorems are, that the energy can by fully determined as a functional of the electronic density $\rho(\vec{r})$ and the theorem that the energy expectation value will always be higher or identical to the actual energy of the system.[32] One can gain information about the ground state energy and structure with DFT and the perturbation of the ground state of the system opens up many new ways of gaining a variety of information about vibrational, electrical, mechanical and many other parameters defining a material.
One important development that influenced the discovery of superconductors substantially is the random structural search, also used by Jiang *et al.* to gain the information about the ground state structure of materials. With the help of ab initio random structural search, researchers could discover novel stable materials. Main characteristic here is the stochastic generation of structures, which then are optimised with the help of DFT which also gives the ground state energy. These random searches helped to gain information about energy landscapes and to find the minima of the PES of a variety of materials. Important here is also the technical development that increased computational power and efficiency remarkably. Many computational methods are developed for structural prediction and for gaining data on potential novel material classes. With the help of these methods, researchers could predict the stable structures of the Ta_2N_3, Nb_2N_3 and V_2N_3 which are used as start point in this project.[9,3]

3.2.1 Predictive framework

Not only can one answer structural questions, but the calculation of the critical temperature is possible from first principal calculations. The most important equations leading to the results of this work are presented in the following, while they are derived and explained in the following sections starting with BCS-theory. Chapter 4 explains the practical implementation based on density functional theory (DFT). BCS-Theory gives the following expression for the critical temperature T_c:

$$T_c = \frac{2e^{\gamma}}{\pi}\omega_D e^{-2/g(\epsilon_F)V_0} = 1.314\hbar\omega_D e^{-2/g(\epsilon_F)V_0} \tag{3.1}$$

Here $g(\epsilon_F)$ is the density of states for both spins at Fermi level ϵ_F, the Euler-Mascheroni constant is $\gamma = 1.134$. The Debye energy ω_D and V_0 characterize the attractive electron interaction. In the following chapter 3.4, this formula will be derived.[33,34]

The MacMillan formula gives a more material-specific estimate of T_c for phonon-mediated superconductivity which will be used for the calculations. The origin of this formula is explained in chapter 3.10 and reads:

$$T_c = \frac{\omega_{log}}{1.2} \exp\left[-\frac{1.04(1+\lambda)}{\lambda - \mu^*(1+0.62\lambda)}\right] \tag{3.2}$$

The average logarithmic frequency or characteristic phonon frequency, that corrects for the relevant low energy phonons, is:[1]

$$\omega_{log} = \exp\left[\frac{2}{\lambda}\int_0^\infty \log(\omega)\frac{\alpha^2F(\omega)}{\omega}d\omega\right] \tag{3.3}$$

μ^* is an empirical parameter that describes the Coulomb screening. Typically its value is between 0.1-0.16, while it can be between 0 and $\frac{\lambda}{2}$. It is shown that the Coulomb strength parameter μ^* is not necessary constant in the full solution of the Eliashberg equations. Especially, if the density of states is varying strongly at the Fermi level.[35]
The momentum integral $\lambda = \sum_{\mathbf{q}\nu} \lambda_{\mathbf{q}\nu}$ is also called the electron-phonon enhancement parameter or electron-phonon coupling and it describes the attractive strength between the phonons and the electrons with a branch index ν. It is calculated for a defined set of **k** and **q**-points. The electron-phonon coupling strength $\lambda_{\mathbf{q}\nu}$ can be defined as following:

$$\lambda_{\mathbf{q}\nu} = \frac{1}{N(\epsilon_F)\omega_{\mathbf{q}\nu}} \sum_{nm\mathbf{k}} |g_{mn,\nu}(\mathbf{k},\mathbf{q})|^2 \delta(\epsilon_{n\mathbf{k}})\delta(\epsilon_{m\mathbf{k}+\mathbf{q}}) = \frac{\gamma_{\mathbf{q}\nu}}{N(\epsilon_F)\omega^2_{\mathbf{q}\nu}} \tag{3.4}$$

The electron phonon matrix elements $g_{mn,\nu}(\mathbf{k},\mathbf{q})$ can be calculated through perturbing the system with a atomic displacement, while m and n describe two bands:

$$g_{mn,\nu}(\mathbf{k},\mathbf{q}) = \frac{1}{\sqrt{2\omega_{\mathbf{q}\nu}}} \langle \phi_{m\mathbf{k}+\mathbf{q}} | \delta V_{\mathbf{q}\nu} | \phi_{n\mathbf{k}} \rangle \tag{3.5}$$

These are obtained as a byproduct from the phonon mode calculation through linear response or finite difference methods to which the Green functions belong.
$N(\epsilon_F)$ is the density of states per spin at Fermi level ϵ_F. $\gamma_{\mathbf{q}\nu}$ are the phonon linewidths. From that the Eliashberg function $\alpha^2F(\omega)$ can be obtained by taking the average over the Brillouin zone (BZ).[33,34] It describes the phonon density of states weighted by the electron phonon interaction:

$$\alpha^2F(\omega) = \sum_{\mathbf{q}\nu} \omega_{\mathbf{q}\nu}\lambda_{\mathbf{q}\nu}\delta(\omega - \omega_{\mathbf{q}\nu}) \tag{3.6}$$

$$\alpha^2F(\omega) = \frac{1}{N(\epsilon_F)} \sum_{\mathbf{k}\mathbf{q},\nu} |g_{mn,\nu}(\mathbf{k},\mathbf{q})|^2 \delta(\epsilon_{n\mathbf{k}})\delta(\epsilon_{m\mathbf{k}+\mathbf{q}})\delta(\omega - \omega_{\mathbf{q}\nu}) \tag{3.7}$$

These quantities can be determined from first principles calculations. Specifically, the electronic properties can be acquired through Density functional theory and the phonon frequencies are given by Density functional perturbation theory. The main parameters needed are the Kohn-Sham energies ϵ_i and wavefunctions $|\phi_i\rangle$ accessible through a ground state calculation and the phonon frequencies $\omega_{\mathbf{q}\nu}$, for which one has to use a perturbative approach.
Noteworthy is how the MacMillan temperature is not only dependent on the phonon modes and electron density, but also on the electron phonon coupling itself. This is important for the value can vary strongly from λ=0.4 for PdH to λ=2 for H_3S.[5] Limitations for the MacMillan formula are that it tends to underestimate the critical temperature for strongly coupled superconductors $\lambda > 1$. One example here is the cubic H_3S, that shows a critical temperature of 125 K at 200 GPa with the MacMillan formula, while one gets 194 K if the Migdal-Eliashberg

equation for the superconducting gap are solved directly.[5] Another breakdown can be found in anharmonic materials for the phonon frequencies are calculated in the harmonic approximation. This is particularly tricky for calculations with hydrogen for quantum effects appear due to the small atomic mass. Another break down of the theoretical calculation is, if unconventional superconductors are encountered, for computational calculations are based on the BCS-theory for conventional superconductors.

3.2.2 BSC-theory

Bardeen, Cooper and Schrieffer (BCS) provided the first microscopic explanation of superconductivity as a superfluid of Cooper pairs due to the electron-phonon coupling. Superconductors of this type are called conventional (or BCS) superconductors.
Cooper pointed out that, in the presence of an attractive force between electrons, the Fermi sea of a normal metal is unstable with respect to the formation of electron pairs (i.e. the so-called Cooper pairs). The strength of the attractive force is not of importance for the Cooper instability, but rather its bare existence. The electron-phonon coupling, in particular, can lead to an effective attractive interaction overcoming the Coulomb repulsion as demonstrated by Fröhlich. BCS-theory is still today essential for the characterization and understanding of superconductivity.[1] It is customarily formulated in terms of a reduced Hamiltonian. For that one has to introduce the annihilation operator $\hat{c}_{k\sigma}$ (creation operator $\hat{c}^{\dagger}_{k\sigma}$) that annihilates (creates) an electron in state $|k\sigma\rangle$ with the momentum or wave vector k, spin σ and band energy ϵ_k. The creation operator for electrons or Bloch waves $\hat{c}^{\dagger}_{k+q'\sigma}$ can be used to construct the formation of a Cooper pair. The final Cooper pair state is: $|k+\frac{1}{2}q\uparrow, -k+\frac{1}{2}q\downarrow\rangle$. Thus, the reduced Hamiltonian can be stated, where the first term is the electronic term and the second one an interaction term:[36]

$$\hat{H}_{red} = \sum_{k\sigma} \xi_k \hat{c}^{\dagger}_{k\sigma}\hat{c}_{k\sigma} + \frac{1}{N}\sum_{k,k'} V_{k,k'}\hat{c}^{\dagger}_{k,\uparrow}\hat{c}^{\dagger}_{-k',\downarrow}\hat{c}_{k',\uparrow}\hat{c}_{-k',\downarrow} \tag{3.8}$$

Assuming that $V_{k,k'}$ is attractive in the superconducting state, the ground state has either empty or doubly occupied pair states leading to Cooper pairs. Superconducting instabilities are due to the scattering between electrons $k\uparrow$ and $-k\downarrow$ with energies $|\xi_{k'}| < \hbar\omega_D$, whereas $|\xi_k| = \epsilon_k - \epsilon_F$ is the energy of electrons relative to the Fermi energy. The Debye frequency ω_D is the phonon bandwidth in the attractive state.

$$V_{k,k'} = \begin{cases} -V_0 & \text{for} \quad |\xi_k| \quad \text{and} \quad |\xi_{k'}| < \hbar\omega_D, \\ 0 & \text{otherwise.} \end{cases} \tag{3.9}$$

A mean field approximation is applied. That means that the one replaces the products of two operators A and B in the following manner: $AB \longrightarrow \langle A\rangle B + A\langle B\rangle - \langle A\rangle\langle B\rangle$. The error is proportional to the second order in deviation of A and B from their averages $((A-\langle A\rangle)(B-\langle B\rangle))$. Now we can plug in: $A = \langle \hat{c}^{\dagger}_{k'\uparrow}\hat{c}^{\dagger}_{-k'\downarrow}\rangle$ and $B = \langle \hat{c}_{-k'\downarrow}\hat{c}_{k'\uparrow}\rangle$. The following mean-field BSC Hamiltonian can be stated:

$$\hat{H}^{MF}_{red} = \sum_{k\sigma} \xi_k \hat{c}^{\dagger}_{k\sigma}\hat{c}_{k\sigma} - \sum_k (\Delta^*_k \hat{c}_{-k\downarrow}\hat{c}_{k\uparrow} + \Delta_k \hat{c}^{\dagger}_{k\uparrow}\hat{c}^{\dagger}_{-k\downarrow}) + \text{const.} \tag{3.10}$$

$$\Delta_k = -\frac{1}{N}\sum_{k'} V_{k,k'}\langle \hat{c}_{-k'\downarrow}\hat{c}_{k'\uparrow}\rangle \qquad \Delta^*_k = -\frac{1}{N*}\sum_{k'} V^*_{k,k'}\langle \hat{c}^{\dagger}_{k'\uparrow}\hat{c}^{\dagger}_{-k'\downarrow}\rangle \tag{3.11}$$

The last term $const.$ is a constant description of the energy shift. Δ_k describes the energy gap. Seeing how $\langle \hat{c}_{-k'\downarrow}\hat{c}_{k'\uparrow}\rangle$ and $\langle \hat{c}^{\dagger}_{k'\uparrow}\hat{c}^{\dagger}_{-k'\downarrow}\rangle$ can be non-zero, the emergence of a new ground state

and the condensation of Cooper pairs is implied. The Hamiltonian $\hat{H}_{red}^{MF}$ is bilinear so it describes two non interacting systems. Now one has to diagonalize the system and determine the temperature at which $\Delta_k = 0$.
For that reason, a Bogoliubov transformation can be applied to the Hamiltonian:

$$\hat{\gamma}_{k\uparrow} = u_k^* \hat{c}_{k\uparrow} - \upsilon_k \hat{c}_{-k\downarrow}^\dagger \tag{3.12}$$

$$\hat{\gamma}_{-k\downarrow}^\dagger = \upsilon_k^* \hat{c}_{k\uparrow} - u_k \hat{c}_{-k\downarrow}^\dagger \tag{3.13}$$

The operator $\hat{c}$ describes electrons. That is why it has to satisfy anti commutation relations. Therefore, γ_k has to be anti commutative like the operator $\hat{c}$ and the coefficients have to satisfy $\{\hat{\gamma}_{k\uparrow}, \hat{\gamma}_{k\uparrow}^\dagger\} = |u_k|^2 + |\upsilon_k|^2 = 1$. The transformation can also be inverted:[36,33]

$$\hat{c}_{k\uparrow} = u_k \hat{\gamma}_{k\uparrow} + \upsilon_k \hat{\gamma}_{-k\downarrow}^\dagger \tag{3.14}$$

$$\hat{c}_{-k\downarrow}^\dagger = -\upsilon_k^* \hat{\gamma}_{k\uparrow} + u_k^* \hat{\gamma}_{-k\downarrow}^\dagger \tag{3.15}$$

The coefficients satisfy all requirements if they are defined as following, whereas $\Phi_k = \arg \Delta_k$:

$$u_k = \frac{1}{\sqrt{2}} \left(1 + \frac{\xi_k}{\sqrt{\xi_k^2 + |\Delta_k|^2}} \right)^{1/2} \tag{3.16}$$

$$\upsilon_k = \frac{1}{\sqrt{2}} \left(1 - \frac{\xi_k}{\sqrt{\xi_k^2 + |\Delta_k|^2}} \right)^{1/2} e^{i\Phi_k} \tag{3.17}$$

In combination with the expression $\Delta_k = |\Delta_k| e^{i\Phi_k}$ the diagonalized reduced Hamiltonian can be stated:

$$\hat{H}_{BCS} = \sum_{k,\sigma} E_k \gamma_{k,\sigma}^\dagger \gamma_{k,\sigma} + \text{const.} \tag{3.18}$$

At $T = 0$ with $E_k = \sqrt{\xi_k^2 + |\Delta|^2}$ and the assumption $\xi_{-k} = \xi_k$ and $|\Delta_{-k}| = |\Delta_k|$, the BSC gap equation can be stated:

$$\Delta_k = \frac{1}{N} \sum_{k'} V_{kk'} \frac{\Delta_{k'}}{2E_{k'}} (1 - 2n_F(E_{k'})) \tag{3.19}$$

For self consistency, the averages have been evaluated accordingly to the BCS Hamiltonian. We assume, that for $|\xi_k| < \hbar\omega_D$, the band gap Δ_0 is independent of the electronic state:

$$\Delta_k = \begin{cases} \Delta e^{i\Phi} & \text{if} \quad |\xi_k| < \hbar\omega_D \\ 0 & \text{otherwise} \end{cases} \tag{3.20}$$

Now to obtain the critical temperature T_c, one has to observe $\Delta_k \longrightarrow 0$. There the temperature corresponds to the T_c. If in this limit of the DOS is constant near ϵ_F and $\beta\omega_D \gg 1$, the gap equation (3.19) becomes:

$$1 \approx V_0 N(\epsilon_F) \int_0^{\omega_D} d\xi \frac{\tanh \frac{\beta\xi}{2}}{\xi} = V_0 N(\epsilon_F) \left(\ln \frac{\beta\xi}{2} \tanh \frac{\beta\omega_D}{2} - \int_0^{\beta\omega_D/2} dx \frac{\ln x}{\cosh^2 x} \right) \tag{3.21}$$

$$\simeq V_0 N(\epsilon_F) \left(\ln \frac{\beta\omega_D}{2} + \gamma - \ln \frac{\pi}{4} \right) \tag{3.22}$$

Now the equation (3.2) for the T_c can be obtained from that.[33]
Furthermore, one can examine the condensation energy. Here, one can calculate the expectation value of the mean field Hamiltonian $\hat{H}$.

$$\langle G|\hat{H}|G\rangle = \sum_k \left(\xi_k - E_k + \frac{|\Delta_k|^2}{2E_k}\right) = E_s \tag{3.23}$$

The condensation energy is the difference between the expectation value and the ground state energy of the metallic phase $2\sum_k \xi_k \Theta(k_f - k)$ at $\Delta_k = 0$:

$$E_s - E_n = \sum_k \left(\xi_k - E_k + \frac{|\Delta_k|^2}{2E_k} - e\xi_k\Theta(k_F - k)\right) \tag{3.24}$$

$$= 2\sum_k (\xi_k - E_k)\Theta(\xi_k)\Theta(\hbar\omega_D - \xi_k) + \sum_k \frac{\Delta_k^2}{2E_k}\Theta(\hbar\omega_D - |\xi_k|) \tag{3.25}$$

Setting the electronic state k for the Fermi state k_F, the following equation can be obtained:

$$E_s - E_n \approx -\frac{1}{2}VN(\epsilon_F)\Delta_0^2 \tag{3.26}$$

The term $\frac{1}{2}N(\epsilon_F)\Delta_0^2$ is the condensation energy density. From there one can obtain the critical field value at zero temperature:

$$\frac{1}{2}N(\epsilon_F)\Delta_0^2 = -\frac{H_c^2}{8\pi} \tag{3.27}$$

$$H_c(0) = \sqrt{4\pi N(\epsilon_F)}\Delta_0 \tag{3.28}$$

3.2.3 The electron-phonon Hamiltonian

The BSC-theory is assuming a rather simple attractive interaction between the electrons, see equation (3.9). The attractive interaction results from the electron-phonon coupling because the electronic states are highly influenced by lattice vibrations, especially close to the Fermi level. One can start building a perturbative system to treat the perturbation of the electronic system by the phonons or vice versa in order to describe the attraction more accurately. To derive the Hamiltonian, that gives the accurate energy of a system, one can start from electrons in a rigid ion lattice without influence of phonons. One cannot start from the phonons for they are changed strongly by the electrons. This change has to be incorporated into the description of the phonons. One can start from the Fröhlich Hamiltonian:[31,36,37]

$$\hat{H} = \hat{H}_e + \hat{H}_{ph} + \hat{H}_{e-ph} \tag{3.29}$$

The formula splits into non-interacting quasi-particles for the electrons $\hat{H}_e$, phonons $\hat{H}_{ph}$ and the electron-phonon part $\hat{H}_{e-ph}$. The electronic part can be described in the approximation as non-interacting quasi particles with energetic dispersion ϵ_k in a periodic lattice whereas the Coulomb interactions are included:

$$\hat{H}_e = \sum_{km\sigma} \epsilon_{km}\hat{c}^\dagger_{km\sigma}\hat{c}_{km\sigma} \tag{3.30}$$

The phonon or lattice Hamiltonian for non interacting quasi particles is the following:

$$\hat{H}_{ph} = \sum_{q\nu} \omega_{q\nu}(\hat{b}^\dagger_{q\nu}\hat{b}_{q\nu} + \frac{1}{2}) \tag{3.31}$$

Again $\hat{b}^{\dagger}_{q\nu}$ and $\hat{b}_{q\nu}$ describe the creation and annihilation operator for a phonon with the momentum q, branch index or polarization state ν and energy or phonon frequency dispersion $\omega_{q\nu}$ of the branch ν and phonon momentum q. These operators can also describe the atomic displacement. The creation operator creates a phonon in state $|q\nu\rangle$. The Hamiltonian for the electron-phonon coupling can be derived in the following way[38]. One can write the periodic normalized displacement describing the normal mode vibrations in terms of the unit cell l and the atoms inside s with the Cartesian indices:[31]

$$u_{ls\alpha} = e^{iqR^0_{l\alpha}} \frac{1}{\sqrt{N_q}} \sum_{q\nu} A^{q\nu}_{s\alpha} (\hat{b}_{q\nu} + \hat{b}^{\dagger}_{-q\nu}) \tag{3.32}$$

$$A^{q\nu}_{s\alpha} = \frac{\eta_{s\alpha}(q\nu)}{\sqrt{2M_s\omega_{q\nu}}} \tag{3.33}$$

Here, $\eta_{s\alpha}(q\nu)$ is the eigenvector of the vibrational mode $q\nu$. N_q is a normalization factor and gives the number of the wavevectors q, which are given by the **q**-points. This leads to the electron-phonon part of the electron phonon Hamiltonian:

$$\hat{H}_{el-ph} = \sum_{kmn\sigma} \sum_{q\nu} g_{mn,\nu}(k,q)(\hat{b}^{\dagger}_{-q\nu} + \hat{b}_{q\nu}) c^{\dagger}_{k+q\sigma} c_{k\sigma} \delta_{k',k+q} \tag{3.34}$$

The electron-phonon coupling matrix element $g_{mn,\nu}(k,q)$ describes the probability of scattering an electron with the momentum k to a state with the new momentum $k+q$ into another band n through absorbing (emitting) a phonon with momentum $q(-q)$ and branch index ν like described by equation (3.5).[31,36,31]

3.2.4 Nambu formalism

An accurate way of calculating superconducting properties are the first-principle Green-functions, that will be briefly discussed below. Green functions are a way of describing the superconducting state in the same way as the a normal state regarding Feynman diagrams.[37,36]
Starting from the electron-phonon Hamiltonian, one can use the Fröhlich Hamiltonian and split it into the part describing the unperturbed particles:

$$\hat{H}_0 = \hat{H}_e + \hat{H}_{ph} \tag{3.35}$$

$\hat{H}_{el-ph}$ is the perturbation linear to the electron-phonon coupling (EPC). Therefore, investigations of this part can make us gain information about the EPC. Green functions can be used to solve this differential perturbation theory problem, in particular one can use imaginary-time Green functions in the Nambu formalism as perturbator:

$$G(k,\tau) = -\langle \hat{T}_\tau c_{k\sigma}(\tau) c^{\dagger}_{k\sigma}(0) \rangle \tag{3.36}$$

This Green function utilizes the imaginary time $-i\tau$ and can be used for fermionic quasiparticles like electrons. Here, $\hat{c}_{k\sigma}(\tau) = e^{H\tau} \hat{c}_{k\sigma} e^{-H\tau}$ and $-\beta < \tau < \beta, \beta = 1/T$. $\hat{T}_\tau$ is the Wick operator or time-ordering operator that orders the operators to increasing τ from right to left.[31]
One can get an expectation value of a physical quantity A in the following manner:[1]

$$\langle A \rangle = \frac{\hat{T}_r(\exp(-\beta H)A)}{\hat{T}_r(\exp(-\beta H))} \tag{3.37}$$

The phonon Green function is the following:

$$D(q,\tau) = -\langle \hat{T}_\tau (\hat{b}_q(\tau) + \hat{b}^{\dagger}_{-q}(\tau))(\hat{b}_q(0) + \hat{b}^{\dagger}_{-q}(0)) \rangle \tag{3.38}$$

Symmetry properties can be denoted to the two in τ periodic functions $G(k,\tau)$ and $D(q,\tau)$, while $\beta = 1/T$:

$$G(k,\tau+\beta) = -G(k,\tau) \tag{3.39}$$
$$D(q,\tau+\beta) = -D(q,\tau) \tag{3.40}$$

Applying a Fourier transformation one can obtain the following:

$$G(k,i\omega_n) = \frac{1}{2}\int_{-\beta}^{\beta} d\tau e^{i\omega_n\tau} G(k,\tau) \tag{3.41}$$
$$D(q,i\nu_m) = \frac{1}{2}\int_{-\beta}^{\beta} d\tau e^{i\nu_m\tau} D(q,\tau) \tag{3.42}$$
$$\tag{3.43}$$

Where n, m are now integers and $\omega_n = (2n+1)\pi/\beta$ the Matsubara fermionic and $\nu_m = 2n\pi/\beta$ the Matsubara bosonic frequencies. Assuming a nonmagnetic state, the spin index is neglected.[31,36]
With the help of the Green functions one can achieve the same like the BCS-theory and get an exact solution following Gor'kov:[1]
Here, Green functions satisfy the equation of motion, that is then solved by a mean-field approximation:

$$\left(-\frac{d}{d\tau} - \xi_k\right) G(k,\tau) = \delta(\tau) - \sum_k{}' V_{kk'} \langle \hat{T}_r c^\dagger_{-k\downarrow}(\tau) c_{-k'\uparrow}(\tau) c_{-k'\downarrow}(\tau) c^\dagger_{-k\uparrow}(0)\rangle \tag{3.44}$$
$$\langle \hat{T}_r c^\dagger_{-k\downarrow}(\tau) c_{-k'\uparrow}(\tau) c_{-k'\downarrow}(\tau) c^\dagger_{-k\uparrow}(0)\rangle \longrightarrow F(k,0)F^*(k,\tau) \tag{3.45}$$

Where F is the anomalous Green's function:

$$F(k,\tau) = -\langle T_r c_{k'\uparrow}(\tau) c_{-k'\downarrow}(0)\rangle \tag{3.46}$$

One can rewrite for the two Green functions:

$$G(k,i\omega_n) = \frac{-i\omega_n - \xi_k}{\omega_n^2 + E_k^2} \tag{3.47}$$
$$F(k,i\omega_n) = \frac{\Delta_k^*}{\omega_n^2 + E_k^2} \tag{3.48}$$

Where $E_k^2 = \xi_k^2 + |\Delta_k|^2$ and the superconducting gap function $\Delta_k = \sum_{k'} F(k',0)$ can be written:

$$\Delta_k = \frac{1}{\beta}\sum_k \sum_{n=-\infty}^{\infty} \frac{V_{kk'}\Delta'_k}{\omega_n^2 + E_k^2} = \sum_k \frac{V_{kk'}\Delta_{k'}}{2E'_k} \tanh\left(\frac{E'_k}{2k_BT}\right) \tag{3.49}$$

Like for BSC-theory, one can now extract limits defining superconductivity. One important assumption is that the gap function is isotropic $\Delta_k = \Delta \neq 0$:

1. $T \longrightarrow 0$ with $VN(E_F) \ll 1$:
   $\Delta \sim 2\hbar\omega_D \exp\left(-\frac{-1}{VN(\epsilon_F)}\right)$
2. $T \sim T_c$, then $\Delta \longrightarrow 0$:
   $T_c = 1.134\omega_D \exp\left(\frac{-1}{VN(\epsilon_F)}\right)$ like equation (3.1).

Same like in the previous section one obtained the first definition of the critical temperature. But BCS-theory has the main drawback that it does does not take any time into account. It solely assumes the electronic interaction as instantaneous, which leads to a low quantitative accuracy.[1]

3.2.5 Migdal-Eliashberg theory

The Eliashberg theory is the extension of the normal-state Migdal theory to the superconducting state. Here, a many-body perturbation approach is applied, whilst the derivation is similar like for BCS-theory, here the electron-phonon interactions are computed within the Kohn-Sham theory.
One simplification is that the perturbation does not need to mix different electron bands or phonon modes to lead to a sufficient representation by a single band or phonon mode index. The lattice dynamics are also decoupled.
As in perturbation theory, one can write the Hamiltonian as a sum of the ground state Hamiltonian and the perturbed Hamiltonian:

$$\hat{H} = \hat{H}_0 + \hat{H}_I \tag{3.50}$$

$$\hat{H}_0 = \hat{H}_{KS} + \hat{H}_{ext} \tag{3.51}$$

$$\hat{H}_I = \hat{H}_{e-e} + \hat{H}_{el-ph} - \hat{H}_{db} \tag{3.52}$$

Here, the $\hat{H}_0$ consists of the Kohn-Sham Hamiltonian plus a Hamiltonian $\hat{H}_{ext}$ describing the coupling with external fields. The interaction Hamiltonian takes the electron-electron and electron-phonon interactions into account, whilst a exchange Hamiltonian $\hat{H}_{db}$ is subtracted to avoid double counting. Because the non-interacting Hamiltonian $\hat{H}_0$ includes a term in $\hat{H}_{ext}$ which contains a proximity field introducing an extra process that is forbidden in particle conserving theory, one cannot apply a conventional many body perturbative approach.[1] One can solve this problem with introducing the Nambu-Gor'kov formalism that introduce two electronic field operators obeying fermionic commutation rules. Now a perturbative approach can be applied with the only difference that the Green's functions and self-energies will be 2×2-matrices and the vertices will carry an additional factor. The following Green function for the unperturbed Hamiltonian can be stated:

$$G_0(k, i\omega_n) = \frac{1}{-\omega_n - \epsilon_k} \tag{3.53}$$

$$D_0(q, i\nu_m) = \frac{1}{-\nu_m - \omega_q} - \frac{1}{-\nu_m - \omega_q} \tag{3.54}$$

In other words, these Green functions can be accounted for a non-interacting system for single particles. One can apply the Many Body Perturbation Theory (MBPT), this is a way to account for each electron correlation. From here the Migdal-Eliashberg theory explains the basic components of a many-body system, which are the propagators. After a partial re-summation the Dyson equations are obtained through analysis of the Feynman diagrams:

$$G(k, i\omega_n)^{-1} = G_0(k, i\omega_n)^{-1} - \Sigma(k, i\omega_n) \tag{3.55}$$

$$D(q, i\nu_m)^{-1} = D_0(q, i\nu_m)^{-1} - \Pi(q, i\nu_m) \tag{3.56}$$

They give the perturbed electron and phonon self-energies: Σ and Π. These are the sum of all one particle irreducible Feynman diagrams that describe the behavior between the quasiparticles.[31] In other words, they contain all the electron-phonon vertices that govern the superconductivity. Migdal's theorem is stating, that the vertex corrections are small in comparison

with the self-energies, which means that the electron-phonon interaction can be truncated. But even with this simplification, the computational cost is still quite high. Therefore, more approximations are made, like e.g. that the Coulomb interactions (and all the other interactions) are replaced by a Fermi surface average. The Green function can then be solved and separated into components to gain the Eliashberg functions. These are then even more simplified through describing the k-dependence by the energies ϵ_{nk}. The Eliashberg functions in the isotropic approximation are then:

$$Z(i\omega_n) = 1 + \frac{\pi}{\omega_n \beta} \sum_{n'} \frac{\omega_{n'}}{\sqrt{\omega_{n'}^2 + \Delta^2(i\omega_{n'})}} \lambda(i\omega_{n'} - i\omega_n) \tag{3.57}$$

$$\Delta(i\omega_n) Z(i\omega_n) = \frac{\pi}{\beta} \sum_{n'} \frac{\Delta(i\omega_{n'})}{\sqrt{\omega_{n'}^2 + \Delta^2(i\omega_{n'})}} [\lambda(i\omega_{n'} - i\omega_n) - \mu] \tag{3.58}$$

$$\lambda(i\omega_n - i\omega_{n'}) = \int \frac{2\omega\alpha^2 F(\omega)}{(\omega_n - \omega_{n'})^2 + \omega^2} d\omega \tag{3.59}$$

Where the spectral function $\alpha^2 F(\omega)$ is given by equation (3.6). These isotropic gap equations are fully accessible by first principle calculations.[37] μ carries the Coulomb interactions, for it is assumed as described that is it constant around the Fermi level and zero outside it.
Here, λ is introduced as a interaction kernel. These equations can be solved for a given temperature T and the isotropic spectral function $\alpha^2 F$. The isotropic coupling constant λ characterizes the strength of the electron phonon coupling. If $\Delta(i\omega_n) \neq 0$, then the superconducting state is achieved. Therefore the max. temperature fulfilling this condition will be the critical temperature T_c, which was already stated by BCS-theory.

3.2.6 Electron self energy

The self-energy can be approximated in the basis of the Kohn-Sham states as:

$$\Sigma(k, i\omega_n) = -\frac{1}{\beta} \sum_{k', n'\mu} \sigma_3 G(k', i\omega_{n'}) \sigma_3 \left((g_{kq\nu,k'})^2 D_\mu(k - k', i\omega_n - i\omega_{n'}) + V_C(k - k') \right) \tag{3.60}$$

V_C is a screened Coulomb potential depending only on the momentum transfer $(k - k')$. Here the electron-phonon matrix elements $g_{kq\nu,k'}$ equals the expression shown in equation 3.5, while the indices vary for n and m do not stand for band indices since section 3.6. The equation can be rewritten using Pauli matrices and the green function matrix can be replaced with the definition of it in the Dyson function. From that the Eliashberg functions can be extracted, that enable the calculation of the electronic density and the chemical potential. These are a complex set of non-linear equation which couple all momenta k.[37]
The lowest-order diagram of the electron self-energy is the virtual exchange of a phonon. After simplification through performing the Matsubara sum over $\omega_{n'}$, the following equation can be formulated:

$$\Sigma_{ep}(k, i\omega_n) = \frac{1}{N_q} \sum_{k', q} |g_{kq\nu,k'}|^2 \left(\frac{b(\omega_q) + f(\epsilon_{k'})}{i\omega_n + \omega_q - \epsilon_{k'}} + \frac{b(\omega_q) + 1 - f(\epsilon_{k'}}{i\omega_n - \omega_q - \epsilon_{k'}} \right) \tag{3.61}$$

It is dependent on temperature through the Fermi distribution function $f(\epsilon) = (e^{\epsilon/T} + 1)^{-1}$ and Bose distribution function $b(\omega) = (e^{\omega/T} - 1)^{-1}$. N_q is the summation over all phonon momenta q. If the self-energy is small enough, the quasiparticle energy is shifted, which is determined by the real part of the electron self energy Σ. The imaginary part of the equation is defining a finite lifetime of the quasiparticle. The inverse of the lifetime gives a linewidth. Rewriting

the imaginary part of the electron self-energy, two spectral functions can be introduced, that describe the probability of scattering electrons with higher energies while absorbing a phonon $\alpha^2F_k^-(\epsilon,\omega)$ or scattering electrons from lower energies while emitting a phonon $\alpha^2F_k^+(\epsilon,\omega)$.This probability depends on the fermionic and bosonic distributions:

$$\alpha^2F_k^{\pm}(\epsilon,\omega)=\frac{1}{N_q}\sum_q\delta(\omega-\omega_q)\sum_{k'}|g_{kq\nu,k'}|^2\delta(\epsilon-\epsilon_{k'}\pm\omega) \tag{3.62}$$

These spectral function $\alpha^2F_k^{\pm}(\epsilon,\omega)$ depends on the electronic state k and influence the linewidth additively through creating decay channels for the quasiparticles. The spectral function can be simplified in the quasielastic approximation. Here, one assumes that, because the electronic scales are much larger then the phonon scale, the difference between emission and absorption is negligible. Also, the phonon energy ω_q can be neglected in the δ-function giving equation (3.6).

3.2.7 Phonon self-energy

Like for the electron self energy in the previous section, also the phonon energy shows a phonon linewidth that can be extracted from the imaginary part. The lowest order diagram can be given after performance of the Matsubara sum:

$$\Pi_q(i\nu_m=\frac{1}{\beta}\sum_n\frac{1}{N_k}\sum_{k,k'}|g^q_{k,k'}|^2\frac{f(\epsilon_k)-f(\epsilon_{k'}}{i\nu_m+\epsilon_k-\epsilon_{k'}} \tag{3.63}$$

Following linewidth can be extracted (half-width-half maximum):

$$\gamma_q=-2Im\Pi_q(\omega_q)=2\pi\frac{1}{N_k}\sum_{k',k}|g^q_{k,k'}|^2(f(\epsilon_k)-f(\epsilon_{k'}))\delta(\omega_q+(\epsilon_k-\epsilon_{k'})) \tag{3.64}$$

Note that Fermi distribution functions f defining the temperature dependence are included. Again the phonon energies are negligible in comparison to the electron energies. The difference $\epsilon_k-\epsilon_{k'}$ is neglected:

$$f(\epsilon_k)-f(\epsilon_{k'})=f'(\epsilon_k)(\epsilon_k-\epsilon_{k'})=f'(\epsilon_k)\omega_q \tag{3.65}$$

$$\gamma_q=2\pi\frac{1}{N_k}\sum_{k',k}|g^q_{k,k'}|^2\delta(\epsilon_k)\delta(\epsilon_{k'}) \tag{3.66}$$

This theoretical line width shows only the contribution for EPC. It is calculated numerically through integrating over the Brillouin zone (BZ) points at Fermi-level ϵ_F in the double delta approximation:[31,36,37]

$$\gamma_{\mathbf{q},\nu}=\sum_{nm\mathbf{k}}|g_{mn,\nu}(\mathbf{k},\mathbf{q})|^2\delta(\epsilon_{n\mathbf{k}})\delta(\epsilon_{m\mathbf{k}+\mathbf{q}}) \tag{3.67}$$

3.2.8 Critical temperature

Morel-Anderson theory is deriving a new analytical estimation of the critical temperature starting at the isotropic Eliashberg functions. In order to get to a more accurate description, it was firstly assumed that Δ is small enough so that equation (3.58) can be linearized and a definition for $\Delta(i\omega_n)$ can be extracted:

$$\Delta(i\omega_n)=\frac{\pi}{\beta Z(i\omega_n)}\sum_{|\omega_{n'}|<\omega_c}\frac{\Delta(i\omega_{n'})}{|\omega_{n'}|}(\lambda(i\omega_{n'}-i\omega_n)-\mu)-\mu\Delta^{\infty}\frac{\pi}{\beta Z(i\omega_n)}\sum_{\omega_c<|\omega_{n'}|<\epsilon_F}\frac{1}{\omega_{n'}} \tag{3.68}$$

It is assumed that λ is finite only for a very small $i\omega_{n'} - i\omega_n << \omega_c$, where ω_c is a much shorter cut-off energy. Δ^∞ defines a constant $\Delta(i\omega_n)$ for very high frequencies and $\lambda = 0$. The definition of Δ^∞ that can be obtained through assuming the absence of the mass renormalization effect for large ω_n due to the electron-phonon coupling $Z(i\omega_n = 1)$ and taking the limit for low temperature:

$$\Delta^\infty = -\left(\mu\frac{\pi}{\beta}\sum_{|\omega_j|<\omega_c}\frac{\Delta_g(i\omega_{n'})}{|\omega_{n'}|}\right)/(1+\mu\log(\epsilon_F/\omega_c)) \tag{3.69}$$

When plugging this equation into equation (3.68) one gets:

$$\Delta(i\omega_n) = \frac{\pi}{\beta Z(i\omega_n)}\sum_{|\omega_{n'}|<\omega_c}\frac{\Delta_g(i\omega_{n'})}{|\omega_{n'}|}(\lambda(i\omega_{n'} - i\omega_n) - \mu^*) \tag{3.70}$$

Now we get a first expression for the pseudo-Coulomb potential μ^*:

$$\mu^* = \frac{\mu}{1+\mu\log(\epsilon_F/\omega_c)} \tag{3.71}$$

Assuming a constant $\lambda(i\omega_{n'} - i\omega_n)$:

$$\lambda = \lambda(0) = 2\int\frac{\alpha^2F(\omega)}{\omega^2}d\omega \tag{3.72}$$

Defining $|\omega_{n'}| = \omega_D$ and $Z = 1 + \lambda$ and the ω_i dependence of Δ is neglected, one can rewrite equation (3.70):

$$\frac{1+\lambda}{\lambda-\mu^*} = \sum_{i=0}^{\omega_D/2\pi T_c - 1/2}\frac{1}{i+1/2} \tag{3.73}$$

A new analytical estimation for the critical temperature can be given:

$$T_c = 1.13\omega_D\exp\left(-\frac{1+\lambda}{\lambda-\mu^*}\right) \tag{3.74}$$

In comparison with the description of the critical temperature by the BCS-theory, one can now see how the mass enhancement effect defined by $Z = 1 + \lambda$ and the Coulomb repulsion described as $\lambda - \mu^*$ reduce superconductivity.[1]
In 1968, McMillan introduced a new formula that could accurately describe the critical formula. For that reason the experimental phonon spectral function of Niobium was used with different scaling and μ^*/λ-ratios:[1]

$$T_c = \frac{\omega_D}{1.45}\exp\left[-\frac{1.04(1+\lambda)}{\lambda-\mu^*(1+0.62\lambda)}\right] \tag{3.75}$$

This formula will also be compared for the materials on interest for the Debye temperature is given by the phonon calculations. Allen and Dynes thoroughly numerically analyzed the isotropic gap equations while varying λ and $\mu*$. That enabled the calculation of the T_c solely defined by the material-dependent quantities $\alpha^2F(\omega)$ and $\mu*$. The prefactor changed and instead of the Debye energy, the logarithmic average was introduced (see equation(3.3)), that corrects for the low energy phonons that are relevant for the superconductivity. They prove that in the range of $\lambda < 2$ and $\mu* > 0.15$ the MacMillan formula (3.3) is valid with the included modified prefactor.[31,36,37] The McMillan formula is nowadays widely used for computing the critical temperatures for first principles and surprisingly, the Coulomb interaction described by μ^* is material independent in this description.

4 Theoretical framework

Abinit is a software to calculate the electrical, vibrational, optical, mechanical, and other properties of materials. It uses density functional theory and combines it with perturbation theories and many body Green's function. It is the main tool in this work and it utilized the formulas explained in section 3.2.1 to predict superconducting behavior.[11,12,13,14,15] In the following, the numerical background to acquire all the important input is described.

4.1 The Schrödinger equation

The Schrödinger equation $\Psi(\vec{r}, \vec{R})$ is a many-body wavefunction describing a quantum-mechanical system, which here consists of nuclei N_i at positions $\vec{R}_i$ and electrons n_i at $\vec{r}_i$. Following the Born-Oppenheimer approximation, the wavefunction can be rewritten in terms of electronic coordinates, whereas the nuclei positions are considered constant and sub nuclear interactions are neglected. This is due to the much higher nucleus mass in comparison to the electronic mass:

$$\Psi(\vec{r}, \vec{R}) = \Psi_{el}(\vec{r})\Psi_{nu}(\vec{R}) \tag{4.1}$$

Because our material is a periodic system described by a unit cell, one can write the states as a superposition of plane waves, the Bloch states, to tackle the problem of having to calculate an infinite amount of wavefunctions for each electron. Conductive electrons therefore move in the periodic potential set by the ionic lattice.
The wavefunctions are calculated just for the electrons in the unit cell in reciprocal space of the Bravais lattice. The wavefunction $\Psi(\vec{r})$ can be written as a sum of Bloch states $\Psi_{\vec{k}}$:[39]

$$\Psi(\vec{r}) = \sum_{\vec{k}} \Psi_{\vec{k}} \tag{4.2}$$

$$\Psi_{\vec{k}}(\vec{r}) = e^{i\vec{k}\vec{r}} f_{\vec{k}}(\vec{r}) \tag{4.3}$$

The wavefunction consists of two parts. The first one is the plane wave part. $\vec{k}$ is a wave vector in reciprocal space that can be described by its wave length $\lambda = \frac{2\pi}{|\vec{k}|}$. Using periodic boundary conditions, all the information about the electronic distribution can be found inside the Brillouin zone (BZ). Therefore, one has to only consider a finite amount of **k**-points inside. The wavefunction is expressed with the help of sampling special sets of high symmetry **k**-points with the help of the Brillouin zone. The plane-wave set at each **k**-point is discrete and describes the wavefunction. The number of **k**-points can be set in the input file in Abinit with the command $ngkpt$. For 3-dimensional systems, a grid of $\mathbf{k}_x \times \mathbf{k}_y \times \mathrm{k}_z$ is used, that is evenly spread in the BZ, also called a Monkhorst-Pack grid. The finer the grid, the more accurate the calculation gets, so a convergence test has to be concluded to choose the right k-point grid [App. 12.2.1]. With the command $kptopt$, one can control the symmetry used in order to generate the k-point grid. Other parameters in the script defining the k-point grid is $nshiftk$: This parameter gives the number of shifted grids to be used to generate the full grid and $shiftk$ gives its values. They are also called Monkhorst-Pack grids. One can have a look at the values chosen in the appendix[App. 12]
The second term is the cell periodic part, that describes the cell periodicity:

$$f_{\vec{k}}(r) = \sum_{\vec{g}} c_{\vec{k},\vec{g}} e^{i\vec{g}r} \tag{4.4}$$

Here, $\vec{g}$ is the reciprocal lattice vector defined by $\vec{g}\vec{q} = 2\pi m$, where $\vec{q}$ is a lattice vector and m an integer. The value of $\vec{g}$ is defined by the energy cut-off. The summation of $\vec{k}$ and $\vec{g}$ gives the radius of the sphere centered around **k** in which the calculation takes place. This explains why there is not necessary the same number of plane waves per **k**-point. The lattice vector $\vec{g}$ is defined by the energy cut-off with the following equation:

$$E(g) = \frac{|\vec{g} + \vec{k}|^2}{2} \tag{4.5}$$

Plane waves are considered as long as their kinetic energy is equal or below E_g. The bigger $\vec{g}$, the higher the corresponding energy is and once a desired accuracy due to the right **k**-point grid is reached, the summation $\vec{k} + \vec{g}$ is neglected, for $\vec{g}$ becomes bigger then $\vec{k}$. The full Bloch function is the following:

$$\Psi_{\vec{k}}(r) = \sum_{\vec{g}} c_{\vec{k},\vec{g}+\vec{k}} e^{i\vec{r}(k+\vec{g})} \tag{4.6}$$

In order to reach the needed electronic cut-off, two approaches are included: The Pseudopotential used makes the frozen core approximation, which leads to a lower energy cut-off needed for the highly energetic core electrons are not considered for interatomic interactions. Furthermore, the potential is smoothed around the nuclei, which is then called Pseudopotential. It also defines the energy cut-off. If a soft Pseudopotential with a soft well is used, a smaller energy cut-off can be used. For a hard Pseudopotential with a deep well, a bigger energetic cut-off should be used to include more oscillations. In the input file, one can then define the energy cut-off with the command $ecut$. It is usually introduced in Hartree and has to be converged in order to catch all the important interactions, like shown in appendix [App. 12.2.2].[39]
One can take equation (6) to build the nth Kohn Sham wavefunction needed to apply density functional theory (see. 2.3):

$$\phi_n(\vec{r}) = \sum_{\vec{k}} \sum_{\vec{g}\vec{k}}^{BZ} c_{n,\vec{k},\vec{g}+\vec{k}} e^{i\vec{r}(\vec{k}+\vec{g})} \tag{4.7}$$

The coefficients $c_{n,\vec{k},\vec{g}+\vec{k}}$ are defined in a self consistent procedure following the variational principle. The variational principle is used to find the ground state (GS) wavefunction and energy. Therefore a self consistent field procedure (SCF) is used, whose convergence criteria are defined by the Abinit input variables. For setting a tolerance, one can use one of the following commands and give them a value (e.g. 10^{-10} (read by Abinit in Hartree)): $toldfe$ for energy, $toldff$ for forces, $toldwfr$ for wavefunction, $tolvrs$ for potential. The maximum number of steps is then defined by $nstep$.[App. 12]

4.2 The Hamiltonian

To obtain the ground state energy, one has to solve the Hamiltonian for the time-independent Schrödinger equation:

$$\hat{H}\Psi(\vec{r}, \vec{R}) = E\Psi(\vec{r}, \vec{R}) \tag{4.8}$$

The Hamiltonian consists of different contribution:

$$\hat{H} = \hat{T}_{el}(\vec{r}) + \hat{T}_{nu}(\vec{R}) + \hat{U}_{el-el}(\vec{r}) + \hat{U}_{el-nu}(\vec{r}, \vec{R}) + \hat{U}_{nu-nu}(\vec{R}) \tag{4.9}$$

After application of the Born Oppenheimer approximations, neglecting the kinetic energy of the nuclei $\hat{T}_{nu}(\vec{R})$, the Coulomb interaction of the nuclei $\hat{U}_{nu-nu}(\vec{R})$ and $\vec{R}$ is considered constant. This will give the electronic Hamiltonian $\hat{H}_{el} = \hat{T}_{el} + \hat{U}_{el-el} + \hat{U}_{el-nu}$, that will be used in combination with the electronic wavefunction.

4.3 Density Functional Theory

The density functional theory (DFT) is a first principle method/ab initio method to solve for systems, that give a tremendous electronic wavefunction for it is dependent on $3 \times N_{el}$ variables. The underlying principle is here to construct the ground state density of a fully interacting system build of non-interacting electrons, also called Kohn Sham one electron states, enabling to make material-dependent predictions.[31] The density functional theory is based on two theorems:

4.3.1 The Hohenberg-Kohn Existence Theorem:

It states that the ground state electronic density is sufficient to determine the the energy as a functional of the density $\rho(\vec{r})$. One reason for is that, the integration of the electronic density $\rho(r)$ gives the number of electrons N_{el}.

$$N_e = \int \rho(\vec{r}))dr \tag{4.10}$$

The external potential V_{ext}, which are the charges and positions of the nuclei, is also given by the non-degenerate ground state density, since each nucleus is located at an electron density maximum.[40] Furthermore, this external potential V_{ext} is defining the density of the system:

$$E_{el}[\rho(\vec{r})] = \int V_{ext}(\vec{r})\rho(\vec{r})d\vec{r} + F[\rho(\vec{r})] \tag{4.11}$$

This leads to the fact, that the non-degenerate ground state density $\rho(r)$ determines the Hamiltonian and thus the wavefunction. Since the Hamiltonian determines all excited-state wavefunctions, the amount of information laying in the density is tremendous. The first theorem is an existence theorem, thus it does not provide any information on how to predict the density $\rho(\vec{r})$ of a system.

4.3.2 The Hohenberg-Kohn Variational Theorem

It states that the density obeys a variational principle. If for instance a well-behaved approximated density indicates an approximated wavefunction and a Hamiltonian, the energy expectation value will be higher or identical the actual energy of the system:[40]

$$\langle \Psi_{app} | \hat{H}_{app} | \Psi_{app} \rangle = E_{app} \geq E_0 \tag{4.12}$$

4.3.3 Practical Implementation

Having the theoretical tools in hand, we can move on to the following problematic: Solving the Schrödinger equation. The description of the electron-electron interaction term in the correct Hamiltonian is complicated to grasp for a many-electron system. The solution is to write the

Hamiltonian operator as a sum of non-interacting one electron operators, the so called Kohn-Sham (KS) operators $\hat{h}_i$:

$$\hat{H}_{KS} = \sum_{i=1}^{N_{el}} \hat{h}_i^{KS} \tag{4.13}$$

$$\hat{h}_i^{KS}(\vec{r}_i)|\phi_i(\vec{r}_i)\rangle = \left(-\frac{1}{2}\nabla_i^2 + V_{ext}(\vec{r}) + V_H[\rho(\vec{r}_i)] + \hat{V}_{xc}[\rho(\vec{r}_i)]\right)|\phi_i(\vec{r}_i)\rangle = \epsilon_i|\phi_i(\vec{r}_i)\rangle \tag{4.14}$$

$$V_{xc}[\rho(\vec{r}_i)] = \frac{\delta E_{xc}(\vec{r}_i)}{\delta\rho(\vec{r}_i)} \tag{4.15}$$

$$V_H[\rho(\vec{r}_i)] = \int_j d\vec{r}_j \frac{\rho(\vec{r}_j)}{|\vec{r}_j - \vec{r}_i|} \tag{4.16}$$

N_{el} here is the total number of electrons. The one electron Kohn-Sham operator $\hat{h}_i^{KS}$ consist of a kinetic energy $-\frac{1}{2}\nabla_i^2$, an external potential V_{ext} felt by the electrons (generated by nuclei or external electromagnetic field) and effective potential terms consisting of the Hartree potential $V_H[\rho]$ and the exchange-correlation potential $\hat{V}_{xc}[\rho]$.[41] These one electron operator then acts on a one electron wavefunction, that is just dependent on three space coordinates instead of a wavefunction, that was dependent on $3 \times N_{el}$ coordinates. These then act onto the independent Kohl-Sham electron wavefunction $\phi(\vec{r})$.

$$E_{N_{el}}[\rho(\vec{r})] = \sum_{i=1}^{N} \hat{h}_i^{KS}|\phi_1, \phi_2, ..., \phi_{N_{el}}\rangle = E_N|\phi_1, \phi_2, ..., \phi_{N_{el}}\rangle \tag{4.17}$$

$$E_{N_{el}}[\rho(\vec{r}_i)] = \int V_{ext}(\vec{r}_i)\rho(\vec{r}_i)d\vec{r}_i - \sum_n^{N_{el}} \int \phi_n^*(\vec{r}_i)\frac{\nabla^2}{2}\phi_n(\vec{r}_i) + \frac{1}{2}\int\int \frac{\rho(\vec{r}_i)\rho(\vec{r}_j)}{|\vec{r}_i - \vec{r}_j|}d\vec{r}_i d\vec{r}_j + E_{xc}[\rho(\vec{r}_i)] \tag{4.18}$$

$$\rho(\vec{r}) = 2\sum_{k=1}^{N_{el}/2} \phi_k^*(\vec{r})\phi_k(\vec{r}) \tag{4.19}$$

For metals, one can calculated the density in a different manner, using a smearing function around the Fermi level, with a distribution function $S(\epsilon_s)$ with a defined smearing value ϵ_s:

$$\rho(\vec{r}, \epsilon_s) = \sum_n S(\epsilon_s)|\phi_k(r)|^2 \tag{4.20}$$

The smearing function can be a Fermi-Dirac (FD) distribution, a Gaussian function, a cold smearing or it can be fixed with the tetrahedron method. One can simplify the above equation to get:

$$E[\rho(\vec{r})] = 2\sum_n S(\epsilon_s)\epsilon_n - \frac{e^2}{2}\int \frac{\rho(\vec{r})\rho(\vec{r}')}{|\vec{r} - \vec{r}'|}d\vec{r}d\vec{r}' + E_{xc}[\rho] - \int \rho(\vec{r})V_{xc}(\vec{r})d\vec{r} \tag{4.21}$$

This equation not only allows for calculation of the ground state energy but also the performance of derivations needed to get to the dynamical matrix.[1]
The terms of the energy can now be calculated self consistently. Just the exchange correlation functional $E_{xc}[\rho(\vec{r}_i)]$ is hard to evaluate. It accounts for the difference between the classical and quantum mechanical electron-electron repulsion and the difference in kinetic energy between the fictitious non-interacting system and the real system.
Most modern functionals do not attempt to solve this term, but either ignore it, try to add the kinetic energy difference between the non-interacting and interacting system separately or add empirical parameters.[40] The Jacob's ladder describes the levels of approximations.[42]

The lowest rung is the 'local density approximation' (LDA). Here the exchange energy density depends only on the density at a point and is that of the uniform electron gas of that density. It is used for metals and in material sciences, but is usually a bad approximation for chemical applications. The next rung includes a generalized gradient approximations (GGAs). These formulas use the density and its gradient, which leads to a higher computational cost, but also to a more exact solution. Famous examples for functionals using GGAs are the BLYP and PBE.[43,44,45,46] In the following work we will use a PBE pseudopotential. The next step are the meta-GGAs, which include the dependance on the Kohn-Sham kinetic energy density. The fourth category of functionals incorporates a part of exact exchange in combination with GGAs. The most popular functional used on that level of DFT is the B3LYP. It mixes a fraction of exact exchange (about 20 %) with GGAs. The hybrid analogue to the PBE is the PBE0.[43,44,45,46,47,48] This type of functionals is called hybrid-functionals. In the following work, we make use of the PBE exchange correlation typed Pseudopotential.
Now we have all tools in hand to get all the information about the energy of the system. A electronic density of states (DOS) can be produced through adding the flag 1 into the input file. Usually it is of importance to converge the DOS with respect to the **K**-point grid. Here, a non-self consistent calculation with the wanted **k**-point grid suffices when having a wavefunction (WFK)-file and density (DEN)-file from a previous, lower **k**-point mesh SCF calculation. A flag inducing this kind of NSCF-calculation is $iscf-3$. Furthermore, the calculation of a band structure requires giving Abinit **k**-points defined by $kptbounds$ at which the band structure should be calculated. These high symmetry points have been produced by abistruct.py with a Abinit input file of the compound in question. With the flag $ndivsm$ one can set how many points are calculated in between the high-symmetry points. $kptopt$ has to be set to the number of $kptbounds$-points multiplied by -1. $iscf-2$ indicates that this calculation is a NSCF-calculation again, while the same **k**-point grid like for the GS-calculation can be used.[App. 12]

4.4 Density Functional Perturbation Theory

Density Functional Perturbation Theory (DFPT) is needed in our case, not only to calculate the phonon frquencies and to gain the electron-phonon matrix elements but also to optimize the system. The trick here is to perturb the ground state Hamiltonian $\hat{H}_0$ by an atomic displacement (also works with any perturbation λ). The Hellmann-Feynmann theorem states that the perturbed first order Hamiltonian $\hat{H}_1 = \hat{H}_0 + V_{ext}(\lambda)$ and the ground state wavefunction Ψ_0^i, given by DFT, are enough to give the first order energy of the system:

$$\langle \Psi_0^i \, | \hat{H}_1 | \Psi_0^i \rangle = \epsilon_1^i \tag{4.22}$$

Extending this simple equation on terms of DFT, one yields the first order energy from which the electron-phonon matrix elements can be calculated:

$$E_1^{el} = \sum_{i=1}^{N_e} \langle \Psi_0^i | \hat{H}_1 | \Psi_0^i \rangle = \sum_{i=1}^{N_e} \langle \Psi_0^i | (T + V_{ext})_1 | \Psi_0^i \rangle + \frac{dE_{xc}[\rho_0]}{d\lambda}|_{\lambda=0} \tag{4.23}$$

With the help of the Sternheimer equation, one can then access the first order wavefunctions iteratively:

$$(H_0 - \epsilon_0^i)|\Psi_1^i\rangle = -(H_1 - \epsilon_1^i)|\Psi_0^i\rangle \tag{4.24}$$

Essentially, the second order energy can be accessed through following the same framework. In order to calculate the second order energy, one just need the first order wavefunction, ground state wavefunction, the first order energy and ground state energy of the system.

4.4.1 Optimisation

Through deriving the total energy, one can obtain a plentora of physical parameters. One of those are the forces, that can be calculated with the help of the Hellmann-Feynman theorem[49]:

$$F_i^\alpha = -\frac{\partial E}{\partial u_i^\alpha(\vec{q})} \tag{4.25}$$

$u_i^\alpha(\vec{q})$ is the displacement of atom i at position α by a vector $\vec{q}$. With help of these parameters one can relax the system and find new cell parameters and atomic coordinates at lower energies. This is explicitly important if vibrational parameters are of interest, for a not fully relaxed structure will affect the atomic vibrations. There are several parameters defining the relaxation in Abinit. $optcell$ defines which parameters will be relaxed, $ionmov$ denotes the type, in the following project the Broyden-Fletcher-Goldfarb-Shanno minimization (BFGS) is used and $ntime$, which limits the number of iterations. The parameter $dilatmx$ helps avoiding a too drastic change of the cell size and $ecutsm$ imposes a smearing on the energy cut-off, so the edges of the plane wave basis are smoothed and the energy cut-off stay consistent with the new size. An example can be seen in the appendix [App. 12.2.3].

4.4.2 Phonon calculation

Following a second order perturbation approach, the energy is again derived by a displacement of the atoms. This derivation gives the interatomic force constants. These give the dynamical matrix and with solving the dynamical equation that is a eigenvalue problem, one can calculate the phonon eigenvectors and phonon frequencies. In order to gain information about the vibrational properties, one has to take the nuclear Schrödinger equation into account:

$$\left[-\sum_i \frac{\hbar^2}{2M_i}\nabla_i^2 + E(\vec{R})\right]\Psi(\vec{R}) = \epsilon\Psi(\vec{R}) \tag{4.26}$$

Here the system is defined solely by the nuclear coordinates $\vec{R}$, the nuclear mass M_i and the energy $E(\vec{R})$ at fixed positions defining the Born-Oppenheimer energy surface. $E(\vec{R})$ is the ground state energy gained from the DFT. Electronic transitions induced by ionic motion are neglected and nuclear interaction with the electrons is instantaneous due to the BOA. The structure needs to be optimized to give a equilibrium geometry so that the forces acting on the nuclei equal to zero. The second derivative then gives the vibrational frequencies in the harmonic approximation. It can also be called the Hessian matrix that can be diagonalized to give the phonon frequencies:

$$\det\left|\frac{1}{\sqrt{M_iM_j}}\frac{\partial^2 E(\vec{R})}{\partial R_i \partial R_j} - \omega^2\right| = 0 \tag{4.27}$$

In terms of a periodic normalized displacement $u_i^\alpha(\vec{q})$ of the atom i with wavevector $\vec{q}$, one can write:

$$\det\left|\frac{1}{\sqrt{M_iM_j}}\tilde{C}_{ij}^{\alpha\beta}(\vec{q}) - \omega^2(\vec{q})\right| = 0 \tag{4.28}$$

$$\tilde{C}_{ij}^{\alpha\beta}(\vec{q}) = \frac{\partial^2 E}{\partial u_i^\alpha(\vec{q})\partial u_j^\beta(\vec{q})} \tag{4.29}$$

The DFPT calculations are done per **q**-point, which describes the wavevector $\vec{q}$. These are the limiting factor in the calculations for it takes a lot of computational time but still has to be converged. It denotes how many unit cells are taken into account for the periodic displacement.

The interatomic force constants $\tilde{C}_{ij}^{\alpha\beta}$ give the dynamical matrix and with solving the following dynamical equation, one can access the phonon frequencies ω:

$$\tilde{D}_{ij}^{\alpha\beta} = \frac{\tilde{C}_{ij}^{\alpha\beta}}{M_i M_j} \tag{4.30}$$

$$\sum \tilde{D}_{ij}^{\alpha\beta}\gamma_j^{\beta} = \omega^2 \gamma_i^{\alpha} \tag{4.31}$$

α and β are the cartesian components of the displacement.[1]
The information about the dynamical matrix can be found in the DDB-files, which are calculated by Abinit for each **q**-point, described by qpt and each irreducible perturbation described by $rfdir$ (direction x,y,z) and $rfatpol$ (atom). The flag $rfphon = 1$ denotes the phonon-type perturbation, while $optdriver = 1$ induces a response-function calculation. These produced DDB-files then have to be merged with mrgddb. With the help of anaddb the phonon frequencies and density of states can be extracted. In order to calculate the phononfrequencies at Γ-point, one just needs the DDB-file at $qpt000$, which stands for the Γ-point. An important flag are here the $ifcflag$, that turns on the calculation of the interatomic force constants. For the phonon dispersion, one needs more **q**-points. Again the **q**-point grid is described with $ngqpt$. The $ngpath$ and $qpath$ flag describes the points on which the phonon band structure and line width are interpolated (0 for Γ-point calculation). In order to get an accurate phonon denisty of state, the variable $ng2qptx, y, z$ denotes the Monkhorst-Pack grid linear dimensions so that a finer **q**-point grid is calculated to achieve the needed accuracy for the DOS, this factor has to be converged as well. $prtdos1$ leads to the printing of the phDOS. All scripts that are used and that inhibit the previously explained information can be seen in the appendix [App. 12.2.4].

4.4.3 Electron-phonon calculation

The new Abinit driver is used to calculate the electron-phonon interactions. It is indicated with the variable $optdriver7$ in the input script. The electron phonon coupling matrix elements are obtained as a byproduct from the phonon calculation as they are obtained by the first order perturbation by atomic displacement of the potential ($\delta V_{\mathbf{q}\nu}$. The electron phonon matrix elements are calculated in terms of the **k** and **q**-points like shown in equation (6).
The first order change in potential consists of the Hartree exchange correlation potential $V_{\mathbf{q}\nu}^{Hxc}(\vec{r})$ and a mix of local/non-local terms from the pseudopotentials $V_{\mathbf{q}\nu}^{e-n}(\vec{r},\vec{r}')$. It can be calculated from the POT-files that are an output of the DFPT calculation($V_{\mathbf{q}\nu}^{scf}(\vec{r})$) and a part depending on the pseudopotential and the geometry, also called the "frozen" part $V_{\mathbf{q}\nu}^{nl}(\vec{r},\vec{r}')$:

$$\delta V_{\mathbf{q}\nu} = V_{\mathbf{q}\nu}^{Hxc}(\vec{r}) + \delta V_{\mathbf{q}\nu}^{e-n}(\vec{r},\vec{r}') = V_{\mathbf{q}\nu}^{scf}(\vec{r}) + V_{\mathbf{q}\nu}^{nl}(\vec{r},\vec{r}') \tag{4.32}$$

Similar like the DDB-files, the POT-output has to be merged to gain a DVDB-file. The first order change of potential can be therefore calculated per **q**-point and irreducible atomic perturbation :

$$\delta V_{\mathbf{q}\nu} = \sum_{Rs} \frac{\partial V}{\partial u_{Rs}} \cdot u_s^{\mathbf{q}\nu} e^{i\mathbf{q}\cdot R} \tag{4.33}$$

After merging the input file for the electron-phonon calculation is called a DVDB-file. The electron-phonon coupling strength λ and the Eliashberg function is then calculated like shown in equation (4) and (5):

$$\lambda_{\mathbf{q}\nu} = \frac{1}{N_F \omega_{\mathbf{q}\nu}} \sum_{mn\mathbf{k}} |g^{\nu}_{mn}(\mathbf{q},\mathbf{k})|^2 \delta\epsilon_{n\mathbf{k}} \delta(\epsilon_{m\mathbf{k}+\mathbf{q}}) \tag{4.34}$$

$$\alpha^2 F(\omega) = \sum_{\mathbf{q}\nu} \omega_{\mathbf{q}\nu} \lambda_{\mathbf{q}\nu} \delta(\omega - \omega_{\mathbf{q}\nu}) \tag{4.35}$$

With that information one can obtain the average logatrithmic frequency $\omega_{\log}$ and the critical temperature like shown in equations (1) and (2).
Throughout the electron-phonon calculation, there are several kinds of interpolations to interpolate for better grids. Firstly, by setting the variable ph_ngqpt, one can use Fourier interpolation to obtain a fine grid of **q**-points. Secondly, by setting eph_ngqpt_fine one can interpolate the potential, this is avoided with using the same set of points like for ph_ngqpt. Generally, the interpolation grids were set: $ph\_ngqpt = eph\_ngqpt = ngkpt$ for maximum accuracy and to avoid the interpolation of the matrix elements. From the electron-phonon calculation one gets two sets of superconducting parameters, the first one is the simply summed DFPT to the a finer **q**-point that is then integrated, which we will call 'Explicit Interpolation'. The second one that we will call the 'Fourier interpolation' interpolated the electron-phonon matrix elements onto a finer set of **q**-points. When displaying the Eliashberg spectral function these are called A2FW (Fourier interpolation) and NOINTO_A2FW (explicit interpolation). So to put everything in a nutshell, for a successful electron-phonon calculation, the following framework has to be followed: The first step is a ground state calculation in order to get the ground state wavefunction (WFK) and density (DEN) file. NSCF-calculations can be concluded in order to gain a denser **k**-point mesh. A **k**-point convergence is needed here because it is just the electrons at the Fermi-surface that contribute to the electron-phonon interaction, so that just a small part of the BZ does contribute. The default smearing method is the tetrahedron method set with $eph\_intmeth2$, that does not need the definition of a smearing factor. But one can also experiment with the Gaussian smearing $eph\_intmeth1$, so that a **k**-point convergence can be investigated with various smearing values $eph\_fsmear0.01$. Afterwards the earlier calculated DDB-files and POT-files are merged (with $mrgddb$ and $mrgdv$) together to give the information about the phonon frequencies (input file:$\_xi\_DDB$), and the electron-phonon coupling (input file: $\_xi\_DVDB$) respectively. Here, the density of the **q**-point mesh is essential, while it has to be a multiple of the **k**-point mesh. In our case because of the rather big unit cell, each perturbation for each **q**-point was calculated separately and then merged. In order to be able to calculate the electron-phonon calculations, a smart parallelization scheme had to be set with the help of eph_np_pqbks 12 1 1 20 1. The first number stand for the irreducible perturbation, the second for the **q**-point grid, the third for the bands, the fourth for the **k**-point grid and the last for the spin. The calculation is split on the different nodes. For the calculations with k-point grid: 8x8x24 and 10x10x30, 240 cores were sufficient with the above mentioned parallelization scheme. For the grid 12x12x36, 480 cores were used with a set-up of eph_np_pqbks 20 1 1 24 1. The memory on each node was the limiting factor. Again, the appendix shows how the script looks in the end [App. 12.2.5].

4.5 Technical information

The Pseudopotentials are taken from the website Pseudo Dojo and they are Perdew-Burke-Ernzerhof (PBE) exchange-correlation typed Pseodopotentials.[50,51]

Table 4.5.1: Technical information about the calculation

Compound	Section	k-point grid	Smearing [Ha]	Energy cut-off [Ha]

η- Ta_2N_3	Convergence study	varied	varied	varied
η- Ta_2N_3	Optimisation	10x10x30	0.01	40
η- Ta_2N_3	Electronic structure	8x8x24	0.01	40
		10x10x30		
		(DOS)		
η- Ta_2N_3	Phononfrequencies at	8x8x24	0.01	40
	Γ-point	varied	varied	
η- Ta_2N_3	Phonon investigation	6x6x18	0.005	40
		8x8x24	0.01	
		8x8x24	0.05	
η- Ta_2N_3	Investigation of the	6x6x18	0.005	40
	instability at Z-point	varied	varied	varied
η- Ta_2N_3	Investigation of the	6x6x18	0.005	40
	influence of	varied	varied	varied
	computational			
	parameters on the			
	electronic structure			
η- Ta_2N_3	Superconductivity	10x10x30	varied	40
η- Ta_2N_3 at 26.065 GPa	Optimisation	10x10x30	0.01	40
η- Ta_2N_3 at 26.065 GPa	Electronic structure	6x6x18	0.05	40
		10x10x30	0.05	
		(DOS)		
η- Ta_2N_3 at 26.065 GPa	Vibrational properties	6x6x18	0.005	40
		6x6x18	0.05	
η- Ta_2N_3 at 26.065 GPa	Superconductivity	10x10x30	varied	40
Tetragonal Ta_2N_3	Convergence study	varied	varied	varied
Tetragonal Ta_2N_3	Optimisation	12x12x12	0.01	40
Tetragonal Ta_2N_3	Optimisation	12x12x12	0.01	40
		16x16x16		
		(DOS)		
Tetragonal Ta_2N_3	Vibrational properties	12x12x12	0.01	40
		8x8x8	0.01	40
η- Nb_2N_3	Convergence study	varied	varied	varied
η- Nb_2N_3	Optimisation	10x10x30	0.01	40
η- Nb_2N_3	Electronic structure	8x8x24	0.01 0.05	40
η- Nb_2N_3	Vibrational properties	8x8x24	0.01	40
		6x6x18	0.05	40
η- Nb_2N_3	Superconductivity	10x10x30	0.01	40
			0.005	40
η- V_2N_3	Convergence study	varied	varied	varied
η- V_2N_3	Optimisation	10x10x30	0.01	40
η- V_2N_3	Electronic structure	12x12x36	0.01	40
η- V_2N_3	Vibrational properties	8x8x24	0.01	40
Trigonal V_2N_3	Convergence study	varied	varied	varied
Trigonal V_2N_3	Optimisation	8x8x8	0.01	40
Trigonal V_2N_3	Electronic structure	8x8x8	0.01	40
Trigonal V_2N_3	Vibrational properties	8x8x8	0.01	40
Trigonal V_2N_3	Superconductivity	24x24x24	varied	40

A "Cold smearing" of N. Marzari, with a=-0.5634 (minimization of the bump) smeared delta

function: $\exp(-xx \cdot 2)/\sqrt{\pi} \cdot (1.5 + xx \cdot (-a \cdot 1.5 + xx \cdot (-1.0 + a \cdot xx)))$ is used. A test is conducted with Fermi-Dirac smearing developed for finite-temperature metals. Smeared delta function: $0.25/(\cosh \frac{xx}{2.0}{}^2)$. Furthermore, the Gaussian smearing is used for superconductivity calculations corresponding to the 0 order Hermite polynomial of Methfessel and Paxton. Smeared delta function: $1.0 \cdot \exp(-xx^2)/\sqrt{\pi}$.

5 Orthorhombic Ta_2N_3

The first compound of interest is the orthorhombic Ta_2N_3, that was synthesized through a high-pressure/ high-temperature route by Zerr *et al.*[7] First-principle calculations were already performed by Jiang *et al.*[9] performing random structural search and investigating the stability of the Ta_2N_3 and other metal nitrides with the same stoichiometry. In the same work the tetragonal Ta_2N_3 was found to have lower energy at ambient conditions, while at pressures above $\tilde{7}.7$ GPa, the orthorhombic Ta_2N_3 becomes the more favorable structure. Further investigations assumed that a low oxygen content in the orthorhombic Ta_2N_3 could impact the stability of this compound and mechanical instability was predicted.[9]

5.1 Convergence study

The **k**-points and the smearing were converged together in order to find the lowest possible **k**-point grid that can be used with the most appropriate smearing value. The energy cut-off was also investigated:

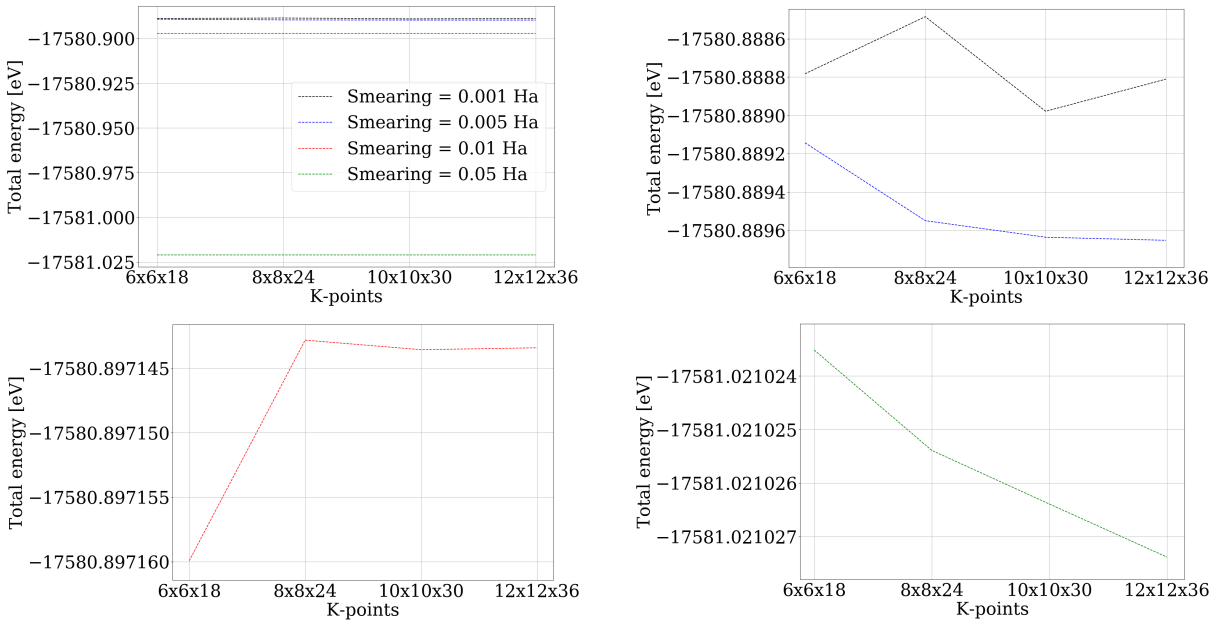

Figure 5.1.1: Convergence study for choosing the right set of **k**-points and smearing factor for the Gaussian smearing. Upper left handed graph shows all the set-up's used while the over graphs are zooming in on the different results. First in the right handed upper graph, a smearing of 0.001 Ha (black) and 0.005 Ha (blue) is shown. Left handed bottom graph depicts a smearing of 0.01 Ha and on the right handed lower part, one can observe the behavior of 0.05 Ha smearing.

One can see that Smearing = 0.001 is too low to represent the electronic states, much more **k**-points are needed for a convergence and the values still vary strongly. Therefore, the other smearing values are examined. For each smearing, convergence with respect to the **k**-point grid is reached very fast. Even a grid of 6x6x18 is acceptable, the difference with the grid 8x8x24 is in the order of around 10^{-5} eV.
The figure for smearing=0.01 shows a positive slope. The difference in total energy for the three smearing values of 0.001, 0.005 and 0.01 and their sets of **k**-points is negligible. Interestingly, a smearing of 0.05 Ha is showing a negative slope and the ground state energy is 0.1 eV lower

due to the entropic term. The smearing does influence the ground state energy ($\pm$ 0.1 eV), while the **k**-point grid does play a minor role for accuracy of the electronic calculation giving a max. error of $\pm 5 \cdot 10^{-5}$ eV. The results for 0.05 Ha smearing give an even smaller error of $\pm 5 \cdot 10^{-6}$ eV

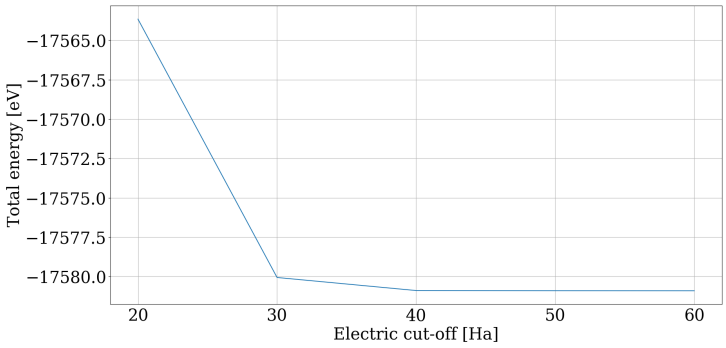

Figure 5.1.2: Energy cut-off convergence study.

An energy-cutoff of 40 Ha was chosen for further calculations. The error is of the size of $\pm 5 \cdot 10^{-1}$ eV, which is of higher order then the change one can find when playing around with the smearing and the **k**-point grid.

5.2 Optimisation

The optimisation gave a new set of cell parameters and atomic coordinates, used for further calculations:

Table 5.2.1: Optimized atomic coordinates and previously theoretically calculated atomic coordinates by Jiang *et al.*[9] and experimental results by Zerr *et al.*[7] while the z-values stay constant due to symmetry restrictions. The values are shown rounded off to three significant digits showing the accuracy of the calculation. An error of $\pm 5 \cdot 10^{-4}$ is found.

Atom	x	y	z
Ta1	0.313 (0.313, 0.313)	-0.021 (-0.21, -0.20)	0.25
Ta2	0.505 (0.505, 0.505)	0.306 (0.306, 0.307)	0.25
N1	0.875 (0.875, 0.875)	0.046 (0.046, 0.025)	0.25
N2	0.549 (0.549, 0.585)	0.879 (0.879, 0.890)	0.25
N3	0.200 (0.200, 0.201)	0.220 (0.220, 0.248)	0.25

The new cell parameter are the following:

- a = 8.18 Å
- b = 8.22 Å
- c = 3.00 Å

The unit cell parameter are in good agreement with previous theoretical results by Jiang *et al.*[9] (a = 8.19 Å, b = 8.24 Å, c = 3.00 Å) and previous experimental results by Zerr *et al.*[7] (a = 8.19 Å, b = 8.18 Å, c = 2.98 Å). Again, the values are rounded off accordingly to their accuracy with an error of $\pm 5 \cdot 10^{-3}$. The unit cell volume is 201.72 Å^3.

5.3 Electronic structure

The density of states for the electronic structure were calculated for a set of 8x8x24 **k**-points and 0.01 Ha cold smearing. The results were compared with other set's with different smearing value (0.005, 0.05) or different **k**-point grid (6x6x18,12x12x36) and no difference could be found. The electronic DOS was also converged with a higher **k**-point grid that also did not show any noteworthy changes validating the convergence of the following result. Therefore, only one set is shown below that is shown with the help of abipy's abiopen.py, that produces a interface to the AbiPy objects, that are produced through Abinit.[52]

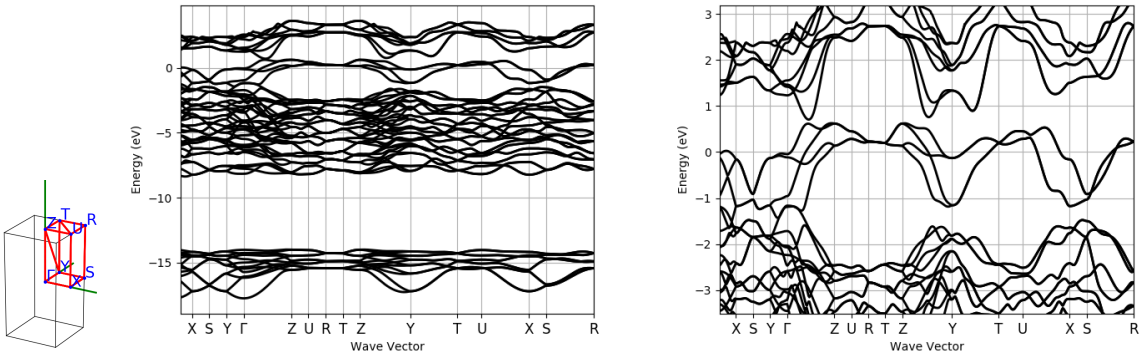

Figure 5.3.1: Electron band structure and a zoomed up version for Ta_2N_3 at ambient pressure. The Fermi-level of 13.716 eV is set as zero-point.

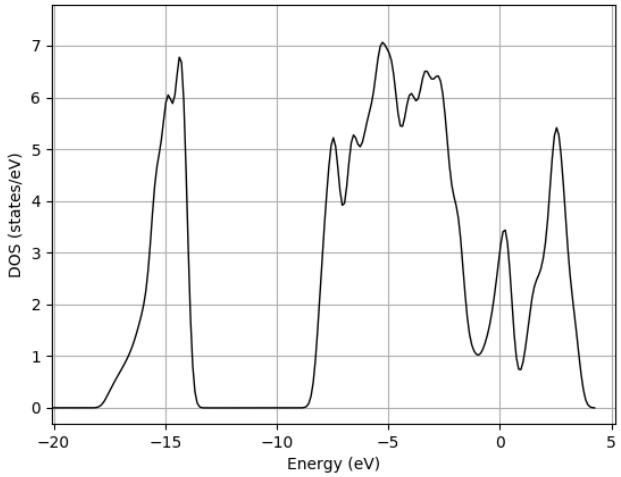

Figure 5.3.2: Density of states for Ta_2N_3 at ambient pressure. The Fermi-level of 13.716 eV is set as zero-point.

5.4 Phononfrequencies at Γ-point

The Phononfrequencies were calculated for the Γ-point and their activity was denoted by the means of point group theory. 60 Phononmodes were found. A **k**-point grid of 8x8x24 and a smearing of 0.01 was used for the following result, while results for the two other set-up's that were investigated were also produced and compared for the Raman active modes. The phonon modes converged within $\pm 10^{-11}$Ha. The digits were reduced so that the solutions can be comparable to the experimental data, that are not as accurate.

Table 5.4.1: 23 IR-active Phononmodes at Γ-point.

Phonon energy [cm^{-1}]	Activity	D_{2h}	Phonon energy[cm^{-1}]	Activity	D_{2h}
61.4	y	B_{2u}	482.3	y	B_{2u}
151.9	z	B_{1u}	501.7	y	B_{2u}
127.8	x	B_{3u}	525.3	x	B_{3u}
132.9	z	B_{1u}	552.5	z	B_{1u}
179.3	x	B_{3u}	558.3	x	B_{3u}
179.8	y	B_{2u}	617.0	z	B_{1u}
200.8	y	B_{2u}	620.5	y	B_{2u}
212.9	x	B_{3u}	635.6	x	B_{3u}
359.8	y	B_{2u}	638.7	y	B_{2u}
385.0	x	B_{3u}	670.1	y	B_{2u}
402.7	z	B_{1u}	763.9	x	B_{3u}
479.0	x	B_{3u}			

Table 5.4.2: Silent modes at Γ-point.

Phonon energy [cm^{-1}]	Activity	D_{2h}	Phonon energy[cm^{-1}]	Activity	D_{2h}
0.0	x^2, y^2, z^2	A_g	127.1	/	A_u
0.0	yz, J_x	B_{3g}	445.8	/	A_u
0.0	x	B_{3u}	535.2	/	A_u
115.4	/	A_u	603.3	/	A_u

The following table describes the frequencies at the Γ-point that are Raman active, a comparison with the different set-up's is conducted to show the influence of the parameter.

Table 5.4.3: 29 Raman active Phononmodes at Γ-point for the different experimental set-up's.

Phononenergy[cm^{-1}]						
12x12x36 0.005 Ha	6x6x18 0.005 Ha	8x8x24 0.01 Ha	8x8x24 0.05 Ha	Expt	Activity	D_{2h}
64.5	64.3	53.5	68.1		xy, J_z	B_{1g}
101.0	101.0	100.8	98.6	107	xz, J_y	B_{2g}
122.6	122.6	122.5	122.8		xz, J_y	B_{2g}
128.8	128.8	128.7	134.5	135	x^2,y^2,z^2	A_g
140.3	140.3	140.1	136.0		yz,J_x	B_3g
153.0	153.0	153.0	155.9		x^2,y^2,z^2	A_g
157.5	157.5	157.6	161.0	162	x^2,y^2,z^2	A_g
168.0	168.1	166.4	184.3	180	xy,J_z	B_{1g}
191.8	191.9	191.5	203.2	198	xy,J_z	B_{1g}
220.9	220.9	220.0	224.7	228	xy,J_z	B_{1g}
236.5	236.6	236.3	246.5	245	x^2,y^2,z^2	A_g
388.2	388.2	383.7	386.5		x^2,y^2,z^2	A_g
393.8	393.9	394.9	394.6		xz, J_y	B_{2g}
420.2	420.2	420.5	420.6	418	yz, J_x	B_{3g}
453.0	453.0	451.3	465.0		x^2, y^2, z^2	A_g
466.4	466.5	464.7	465.8	469	xy, J_z	B_{1g}
470.4	470.5	470.5	480.6		yz, J_x	B_{3g}

500.1	500.1	500.4	506.0	510	xz,J_y	B_{2g}
528.5	528.6	528.7	539.1		xy, J_z	B_{1g}
550.6	550.6	551.6	549.8		xz, J_y	B_{2g}
554.0	554.0	554.2	565.6		yz, J_x	B_{3g}
591.6	591.6	590.3	591.7		x^2, y^2, z^2	A_g
605.5	605.6	602.9	601.3		xy, J_z	B_{1g}
609.6	609.7	609.3	612.8	610	xy, J_z	B_{1g}
620.5	620.5	620.5	636.1		x^2, y^2, z^2	A_g
646.5	646.6	644.1	658.5		xy, J_z	B_{1g}
654.4	654.5	654.8	664.1	671	x^2, y^2, z^2	A_g
713.1	713.1	712.1	727.3		xy, J_z	B_{1g}
729.3	729.3	729.7	740.1	759	x^2, y^2, z^2	A_g

One can see from the first two columns, how the **k**-point grid does not influence the frequencies noteworthy (± 0.1 cm^{-1}) when keeping the smearing constant. The results from smearing 0.005 Ha to 0.01 Ha do change up to around (± 2 cm^{-1}). Comparing the change from smearing 0.1 Ha to 0.05 Ha, the difference aggravates leading to changes up to around (± 20 cm^{-1}). The smearing 0.05 Ha is already very high. The reason for taking it into account is the lower ground state energy and the interesting behavior that will be shown in the next sections. A Raman spectrum is calculated and compared to experimental results.

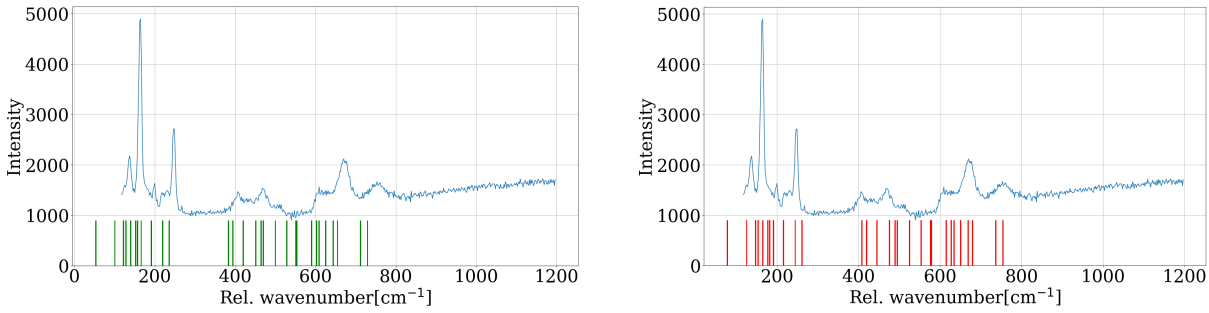

Figure 5.4.1: Experimental Raman spectrum (blue) in comparison with the theoretically calculated Raman-active phonon modes without a shift (green) and with a constant shift of +25 cm^{-1} (red). A light wavelength of 830 nm was used at pressure 0.8 GPa to obtain the experimental curve.

The shift was chosen empirically with trying to fit the theoretical result onto the experimental ones. Various shifts and stretches were trying while a shift of +25 cm^{-1} gave the best result. One can see that the theoretical peaks are slightly red shifted. Physically, it is hard to explain a rigid shift, a stretch blue shifting the frequencies could be explained through thermal expansion. The experimental values are calculated at ambient temperature and pressure, while the theoretical values are calculated for 0 K.
When comparing the experimental Raman modes with the Raman modes from the calculation with the smearing=0.05 Ha, one can get similar results, while a shift of +20 cm^{-1} is sufficient.

5.5 Phonon Investigation

For calculation of the phonondispersion, the **k**-point grid was reduced to 6x6x18. A **q**-point grid of 2x2x6 was used to achieve the following results:

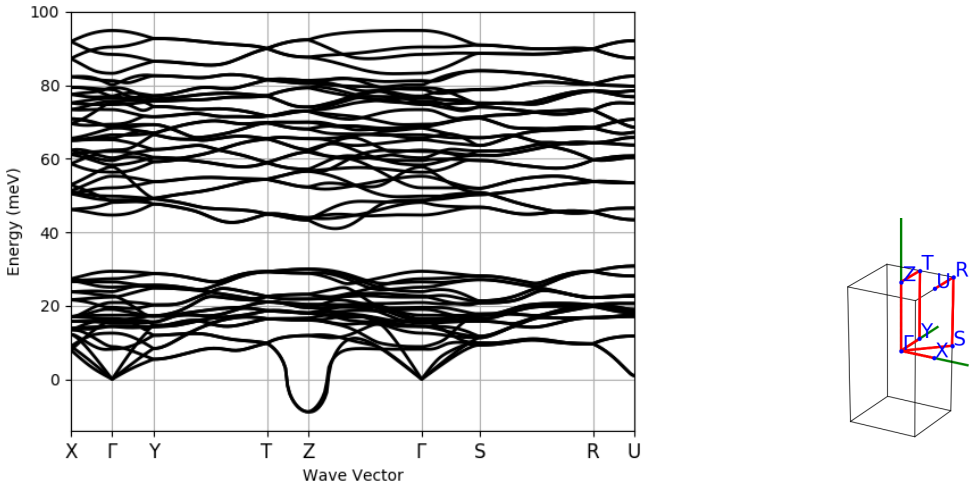

Figure 5.5.1: Phonondispersion for Ta_2N_3 at ambient pressure for 6x6x18 and 0.005 smearing with a **q**-point grid of 2x2x6.

One can see a significant instability at the Z-point. A optimisation of the structure with higher SCF-criterion was repeated following the phonon dispersion calculation in order to make sure the structure was sufficiently relaxed. No considerable changes were found, leading to the fact that the structure is relaxed enough. The forces on the atoms were of the order of 10^{-6} eV/Å^3.

If the smearing is changed to higher values, one can see a stabilization of the mode at the Z-point.

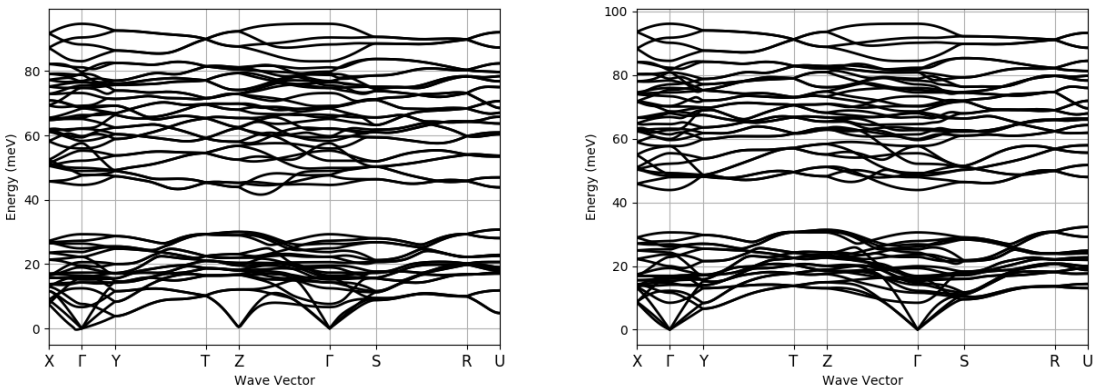

Figure 5.5.2: Phonondispersion for Ta_2N_3 at ambient pressure using a **k**-point grid of 8x8x24 and 0.01 (left) or 0.05 (right) smearing with a **q**-point grid of 2x2x6.

One explanation could be, that the Fermi surface is highly sensitive to changes in the temperature. It could explain the instability disappearing at higher smearing. But the used cold smearing does not induce a physical meaning. Furthermore, it was mentioned in literature that a small amount of oxygen stabilizes the structure.[9] This oxygen doping has not been taken into account in these calculations.

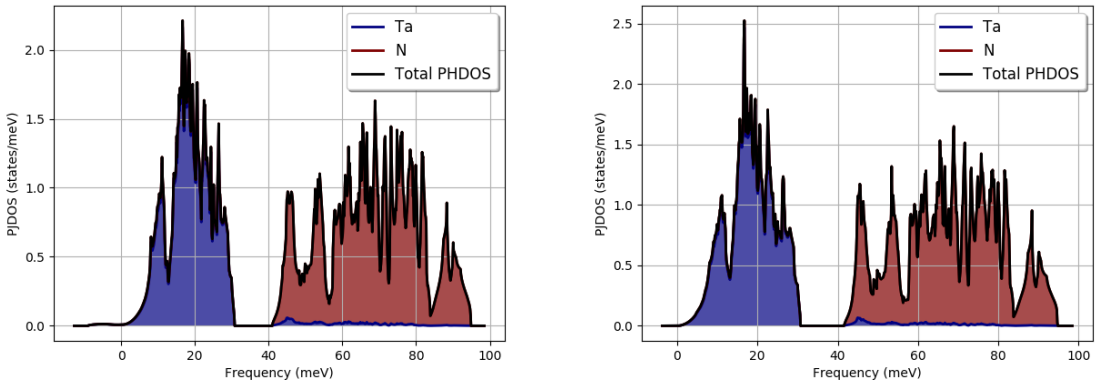

Figure 5.5.3: Phonon density of states for Ta_2N_3 at ambient pressure for 6x6x18, 0.005 smearing (left) and 8x8x24, 0.01 smearing

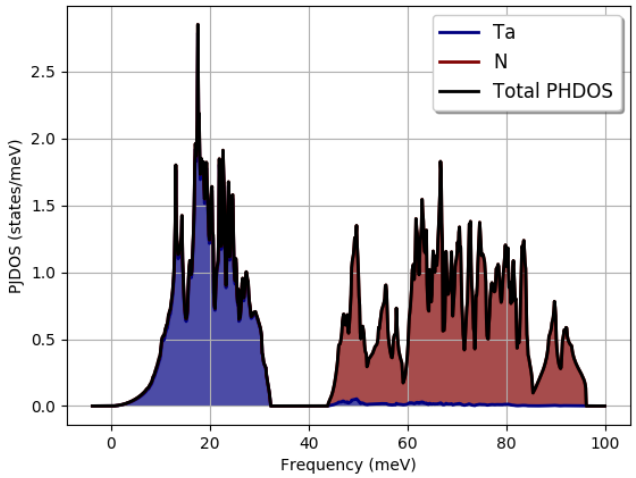

Figure 5.5.4: Phonon density of states for Ta_2N_3 at ambient pressure for **k**-point grid 8x8x24 and 0.05 smearing

The phonon density of states was calculated with interpolation on a higher grid of **q**-points. A grid of 24x24x72 was used. A convergence test was conducted, whereas no difference to a **q**-point grid of 16x16x48 was found.

5.6 Investigation of the instability at Z-point

One can see instabilities at Z. Therefore, the **q**-point (0,0,0.5) is further investigated. The eigenvectors for that **q**-point are calculated and frozen into the structure. One can find two degenerate instabilities at Z, therefore, two sets of eigendisplacements can be simulated and compared:

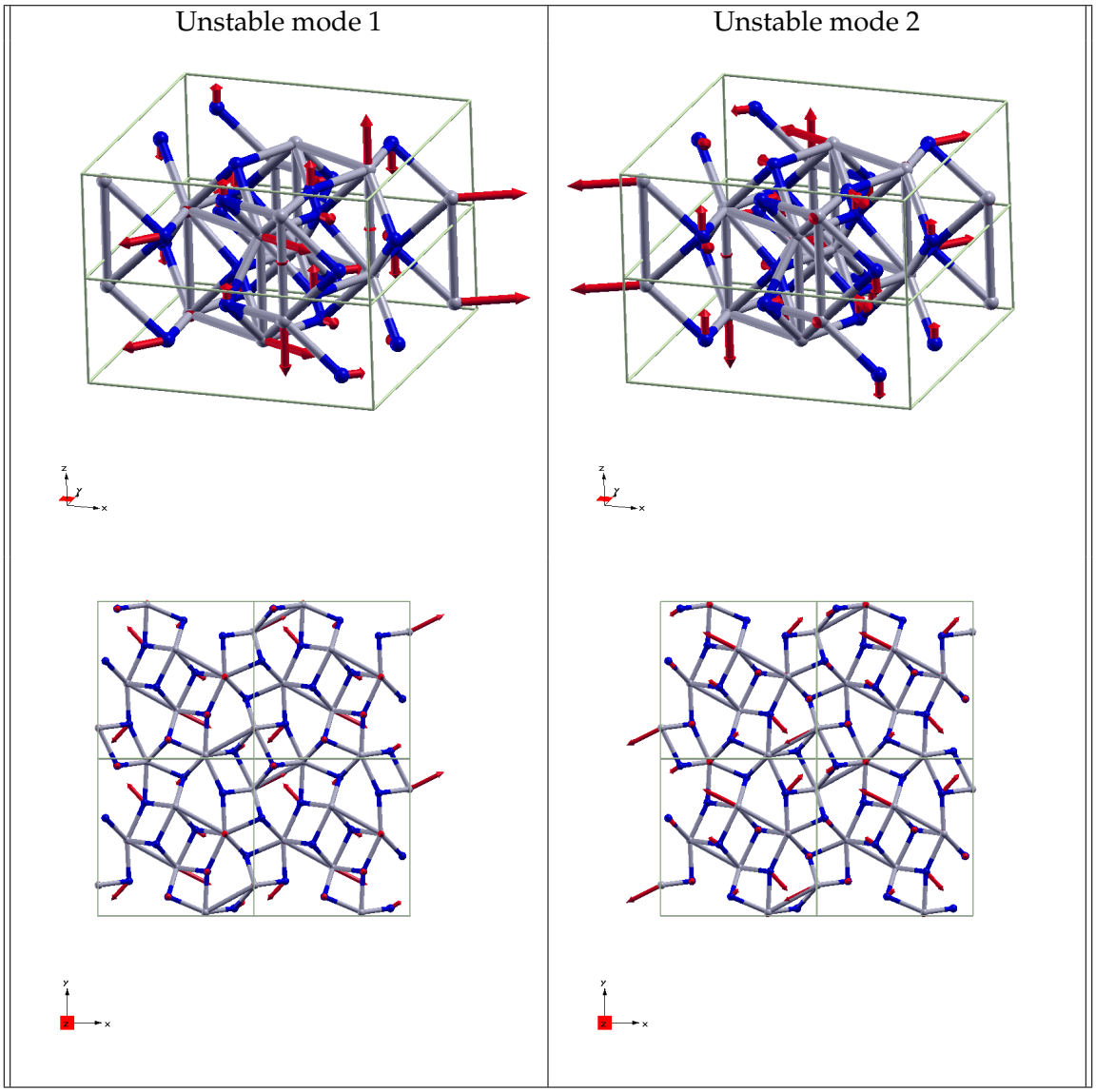

Figure 5.6.1: Ta_2N_3-structure with its Eigendisplacement coming from the two unstable modes are shown and compared. In the top part, two Ta_2N_3 unit cells along Z-direction are shown with the Eigendisplacements. On the bottom, the view of 2x2x2 unit cells is shown. (Red = Eigendisplacement, Blue=Nitrogen, Grey=Tantalum).

One can see how the two modes are correlated through symmetry, for the two Eigenvectors produced by the instability show some degree of similarity. After freezing of the displacements, one gets a unit cell with 40 atoms, where the cell parameter a and b stay constant, while the cell parameter c is doubled, as shown in figure 3.6 or 3.9 without any major changes of the atomic coordinates ($\pm$ 0.01). Therefore, the calculation parameters are further investigated, to try to explain the exhibited behavior.

The **k**-points and energetic cut-off are varied to see the evolution of the unstable mode:

Table 5.6.1: Evolution of the wavenumber with the change of **k**-point grid, energy cut-off and smearing.

k-points	Smearing [Ha]	Energy cut-off [Ha]	$\omega_{\min}$ [cm^{-1}]
8x8x24	0.001	40	-76.346
4x4x4	0.005	40	-72.401
6x6x12	0.005	40	-75.550
6x6x18	0.005	40	-72.593
6x6x18	0.005	60	-72.576
8x8x24	0.005	40	-71.951
12x12x12	0.005	40	-75.330
12x12x36	0.005	40	-71.766
6x6x18	0.01	40	4.880
8x8x24	0.01	40	3.958
6x6x18	0.05	40	105.890
8x8x24	0.05	40	105.918
8x8x24	0.00001 (Fermi-Dirac)	40	-69.586
8x8x24	0.0001 (Fermi-Dirac)	40	-69.735
8x8x24	0.001 (Fermi-Dirac)	40	-70.211
8x8x24	0.01 (Fermi-Dirac)	40	99.594

Energy cut-off:
When changing the energy cut-off to 60 Ha while keeping the original **k**-point grid of 6x6x18, the unstable phonon modes are similar to the previous ones, indicating convergence of the energy cut-off like predicted in section 5.1.

Spin-Orbit coupling (SOC) influence:
Another test was conducted with a Pseudo potential including spin-orbit coupling because Tantalum is a heavy atom that could display this effect influencing the calculation. A **k**-point grid of 6x6x18 and smearing=0.005 Ha was used. The modes remained unstable and unchanged: -72.593 cm^{-1}.

Adding empty bands:
After adding 15 additional empty bands for the calculation, one gets a phonon frequency of 4.043 cm^{-1} for 8x8x24 and 0.01 smearing showing a sufficient amount of bands included by default.

Smearing:
The smearing was varied, to see its influence. It impacts the phononmode extraordinarily. It shows, how the structure is highly sensitive in the Z-direction. With higher smearing, the mode stabilizes. With a smearing of 0.05, which is very high, the previously unstable phononmode reaches wavenumber in the order of 100 cm^{-1}. Interestingly, if the smearing is lowered, the change of frequency is not as big as when it is increased (see difference between 0.001, 0.005 and 0.01). Furthermore, the kind of smearing was changed from Cold-smearing to Fermi-Dirac smearing. Similar behavior was found, although Fermi-Dirac smearing shows an exponential growth, while cold smearing consists of Gaussian-kind growth. As expected, at 0.01 Ha smearing, the Fermi-Dirac variant leads to a more stable structure.

k-point grid:
Seems to play a minor role regarding the unstable phononmode.

5.7 Investigation of the influence of computational parameter on the electronic structure

The phononmode at the Z-point shows high sensitivity, for it changes from being unstable at a low smearing to being stable at high smearing, where it goes from being very soft to showing a more typical bahavior at higher smearing like e.g. 0.05 Ha. A thorough investigation of the bandstructure and the fermisurface is needed and conducted. The Fermi-energy is: 13.716 eV. 92 bands were calculated, whilst band 84 is the lowest unoccupied band. Bands 81, 82 ,83 have varying occupation levels for each **k**-point calculated and they do cross Fermi-level partially, these are therefore further investigated:

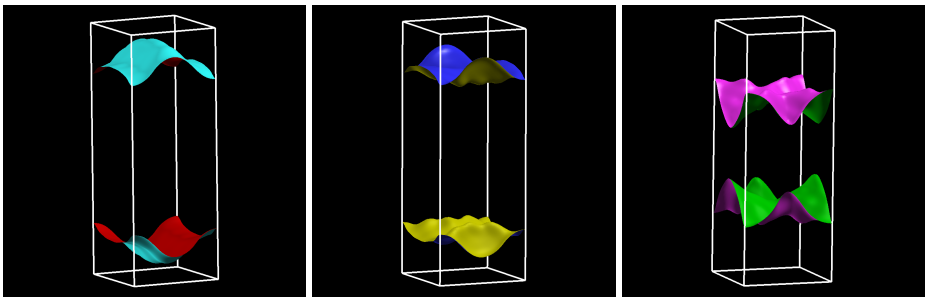

Figure 5.7.1: The three bands 81, 82, 83 being the highest occupied bands.

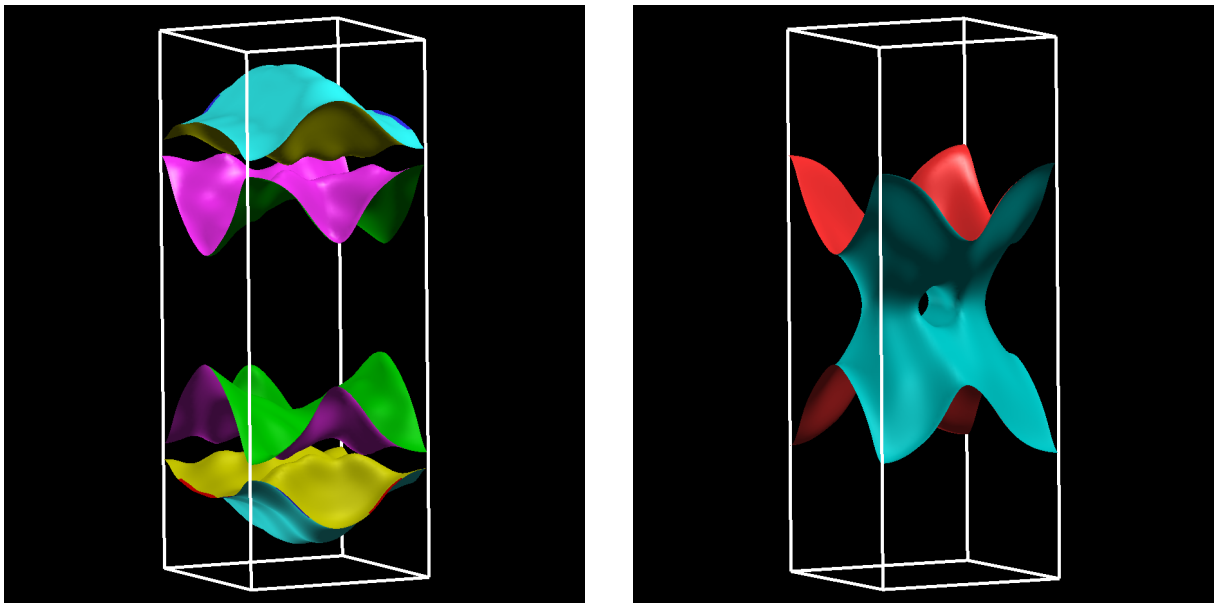

Figure 5.7.2: The Fermi-surface for the highest occupied bands 81, 82, 83 (left) in comparison with the the lowest unoccupied bands 84 (right).

The bands between the Γ- and Z-point were further investigated for different experimental set-up's, whereas the eigenvalues were taken from the SCF ground state calculations, that were based on the phonon mode calculation.
The bands 80-86 were chosen for the following graphs, to show the behavior of the occupied band 80, the partially occupied bands 81,82,83 and the two unoccupied bands 84 and 85. Band 84 seems to be partially occupied for the high smearing cases, due to the change of Fermi-level.

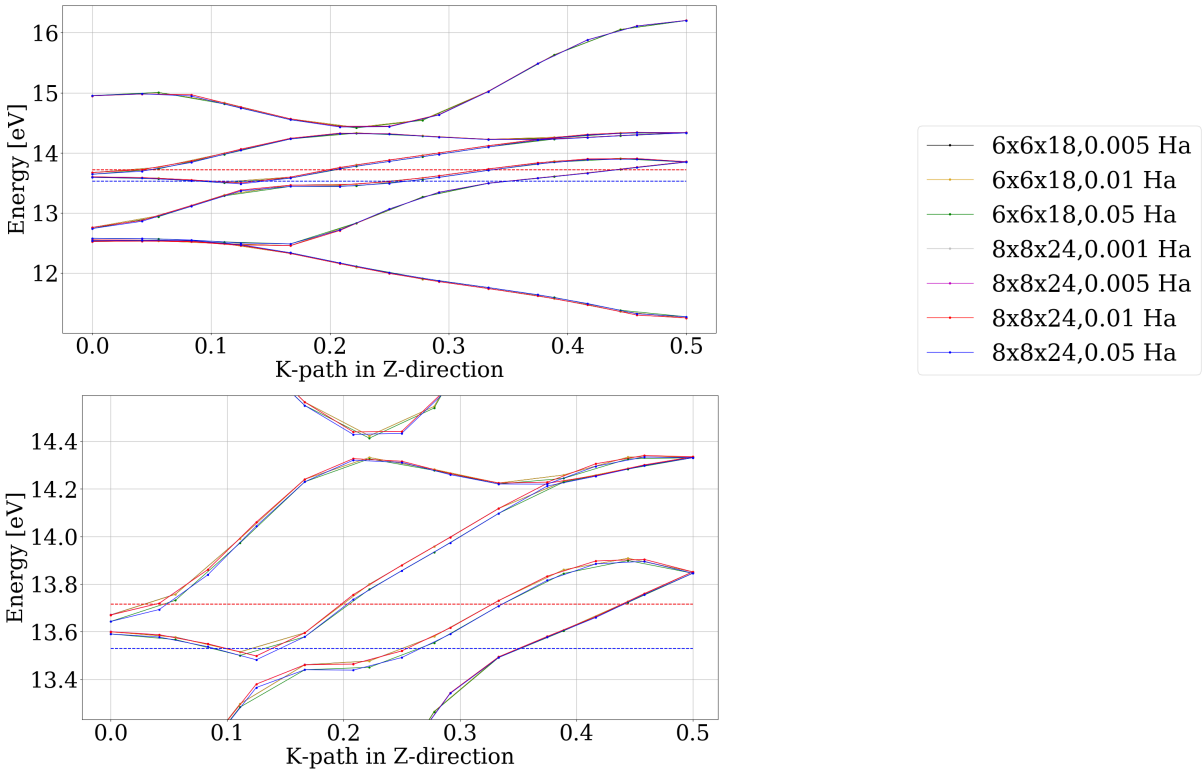

Figure 5.7.3: Comparison of the bands 80-85 for **k**-point grids 6x6x18 and 8x8x24 with different cold smearing values. The Fermi-level is shown as a straight line. The values overlap and therefore not all the colors are visible. Therefore a second diagram showing a close-up is produced.

One can see in the figure 5.7.3, how the bands are almost identical. The bands are not notably influenced by the **k**-point change from 6x6x18 and 8x8x24 except right after 14.2 eV at around 0.33 K-path length to the Z-point, where the **k**-point grid of 8x8x24 shows a crossing while it can't be seen for a **k**-point grid of 6x6x18. The Fermi-level is another difference that can be seen, which could lead to a different behavior of the material. This especially impacts the two bands 83 and 84 that start at Γ-point in between the different two Fermi-level values. For the higher Fermi-level, these bands start beneath the Fermi-level and vice versa. Afterwards, these two bands gain in energy towards Z-point. The lower Fermi-level appears with high smearing factors of 0.05 Ha. The occupation can't be seen in the band structure, but one can find the occupations in an density of states output. It becomes clear that much more are partly filled bands (≈ 25) appear for the higher smearing then for the low smearing (≈ 3). It is possible, to have an instability at very low temperatures for the Ta_2N_3.

Table 5.7.1: Fermi-levels for the different calculation set-up's.

K-points	Smearing [Ha]	Fermi level [eV]
8x8x24	0.001	13.7178
8x8x24	0.001 (Fermi-Dirac)	13.7151
6x6x18	0.005	13.7154
8x8x24	0.005	13.7162
12x12x12	0.005	13.7143
12x12x36	0.005	13.7162
6x6x18	0.01	13.7162
8x8x24	0.01	13.7159
6x6x18	0.05	13.5292
8x8x24	0.05	13.5292

To get a more accurate value for the Fermi level, one must usually do a NSCF calculation with a more dense **k**-point grid, which could be an error source. But for comparison in order to see the trend it should be sufficient.
The band structure was thoroughly investigated and to conclude, the smearing change does only impact the Fermi-level. The change in **k**-point grid shows differences in the band structure when looking closely but they are of very small magnitude, even when comparing a grid of 6x6x18 and 12x12x36:

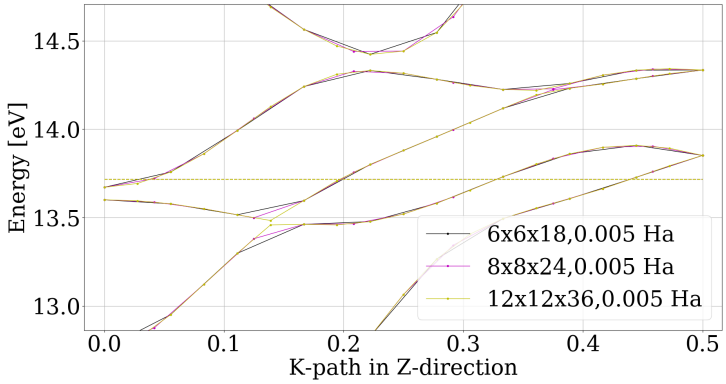

Figure 5.7.4: Comparison of the bands 80-84 for **k**-point grids 6x6x18, 8x8x24 and 12x12x36 with smearing 0.005 Ha

A direct comparison between two calculations that just differ by the kind of smearing was also concluded. If one compares cold smearing and Fermi-Dirac smearing, both using a smearing factor of 0.001 Ha, the band structure does not change notably, the max difference between the energy is in the order of 10^{-4} eV and therefore definitely negligible.

To conclude everything, the small differences (around $\pm 5 \cdot 10^{-1}$) between the bands come from the change of the **k**-point grid which also influences one crossing close to the Fermi-level. The bands do not vary with changing the sensitive parameter which is the smearing. The smearing is mainly influencing the occupational levels leading for more bands being partially filled for higher smearing, which does make sense from a physical perspectives. Because finally, smearing can be seen as adding temperature to the system, that enables population of bands laying in higher energies. And although the cold smearing does not populate the states in a physical manner, it is shown to lead to more accurate result. It's behavior is also shown to be similar to the Fermi-Dirac smearing leading to a physical-like population of the states.

5.8 Superconductivity

5.8.1 Convergence study

In the following, the DDB-files and POT-files produced by a calculation with the smearing 0.05 Ha are used to conduct the convergence study. Later the results are compared with results that are acquired with using the DDB-file/POT-files produced with a smearing 0.01 Ha, while we assume same convergence behavior. For all the electron-phonon calculations, a empirical parameter of 0.12 was used. In order to calculate the important parameters accurately, a smearing and **k**-point calculation has to be conducted again for the electron-phonon calculation to find the correct experimental set-up:

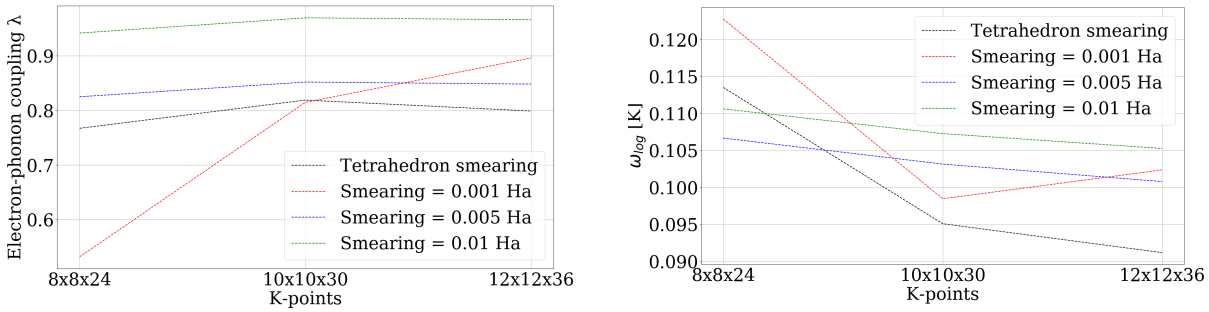

Figure 5.8.1: Convergence for different smearing types and values and **k**-point grids of the isotropic electron-phonon coupling constant λ and the logarithmic frequency ω_{log}.The additionally Fourier interpolated results are featured in the convergence studies.

Each smearing leads to a different converged isotropic electron-phonon coupling constant λ, while the Gaussian smearing with the smearing factor 0.001 Ha is probably needs more **k**-points to represent the superconducting parameter correctly. One can see how convergence is reached with a **k**-point grid of 10x10x30 for the tetrahedron smearing, the Gaussian smearing with the smearing factors= 0.005 Ha, 0.01 Ha regarding the electron-phonon coupling constant λ.
The logarithmic frequency ω_{log} is unrealistically small, therefore the calculation of the critical temperature is also wrong. Nevertheless it is shown and taken into account for convergence reasons. The values converge well showing how the ω_{log} underestimation is probably a systematic numerical error. A **k**-point grid of 10x10x30 is used for further calculations with the three smearing methods that give a well-converged value (Tetrahedron method, Gaussian smearing with the smearing factor 0.005 Ha, 0.01 Ha). They are compared to each other.

5.8.2 Further investigations and results

In order to conduct the electron-phonon calculation, the previously calculated files have to be used as an input. The DDB-files and POT-files are products of the phonon calculation and as described before, they show major differences between the smearing values. Therefore, two data sets are investigated. Other input files needed are the ground state calculation WFK- and DEN-file, for which a new convergence study was conducted in the previous section. From the electron-phonon calculation one gets two sets of superconducting parameters, the first one is the simply summed DFPT to the a finer **q**-point that is then integrated, which we will call 'Explicit Interpolation'. The second one that we will call the 'Fourier interpolation' interpolated the electron-phonon matrix elements onto a finer set of **q**-points. When displaying the Eliashberg spectral function these are called A2FW (Fourier interpolation) and NOINTO_A2FW (explicit interpoltion).

Data set 0.05 Ha

The results for the **k**-point grid 10x10x30 are shown in the following table.

Table 5.8.1: Results for the isotropic parameters for different interpolation techniques and smearing techniques. The first column per smearing method called "Explicit interpolation" is interpolated but then the matrix elements are taken explicitly on the **k**-point grid and the second one is Fourier interpolated with respect to the DDB q-points (interpolated by ph_ngqpt).

	Tetrahedron smearing		Gaussian smearing 0.01 Ha		Gaussian smearing 0.005 Ha	
	Explicit Interpolation	Fourier interpolation	Explicit Interpolation	Fourier interpolation	Explicit Interpolation	Fourier interpolation
T_c [K]	$4.06 \cdot 10^{-3}$	$4.08 \cdot 10^{-3}$	$6.82 \cdot 10^{-3}$	$6.41 \cdot 10^{-3}$	$5.00 \cdot 10^{-3}$	$4.82 \cdot 10^{-3}$
Isotropic λ	0.7735	0.8188	0.9131	0.9695	0.8002	0.8519
$\omega_{\log}$ [K]	0.1077	0.0951	0.1272	0.1073	0.1225	0.1032
Positive moments of $\alpha^2F(\omega)$						
λ (ω^2)	$1.04 \cdot 10^{-6}$	$1.04 \cdot 10^{-6}$	$1.261 \cdot 10^{-6}$	$1.26 \cdot 10^{-6}$	$1.11 \cdot 10^{-6}$	$1.11 \cdot 10^{-6}$
λ (ω^3)	$2.32 \cdot 10^{-9}$	$2.34 \cdot 10^{-9}$	$2.80 \cdot 10^{-9}$	$2.82 \cdot 10^{-9}$	$2.49 \cdot 10^{-9}$	$2.51 \cdot 10^{-9}$
λ (ω^4)	$5.93 \cdot 10^{-12}$	$6.05 \cdot 10^{-12}$	$7.14 \cdot 10^{-12}$	$7.27 \cdot 10^{-12}$	$6.36 \cdot 10^{-12}$	$6.50 \cdot 10^{-12}$
λ (ω^5)	$1.60 \cdot 10^{-14}$	$1.66 \cdot 10^{-14}$	$1.92 \cdot 10^{-14}$	$1.98 \cdot 10^{-14}$	$1.72 \cdot 10^{-14}$	$1.78 \cdot 10^{-14}$

The Eliashberg function α^2F evaluates the phonon density of states weighted by electron phonon interactions.[1] Therefore, it can be compared to the phonon density of states. It is shown interpolated, whilst the **q**-points are Fourier interpolated, so that they are given for a grid that equals the **k**-point grid. The electron-phonon matrix elements are therefore automatically also calculated for a grid that equals the **k**-point grid. In order to understand better, the α^2F spectrum is shown and compared below:

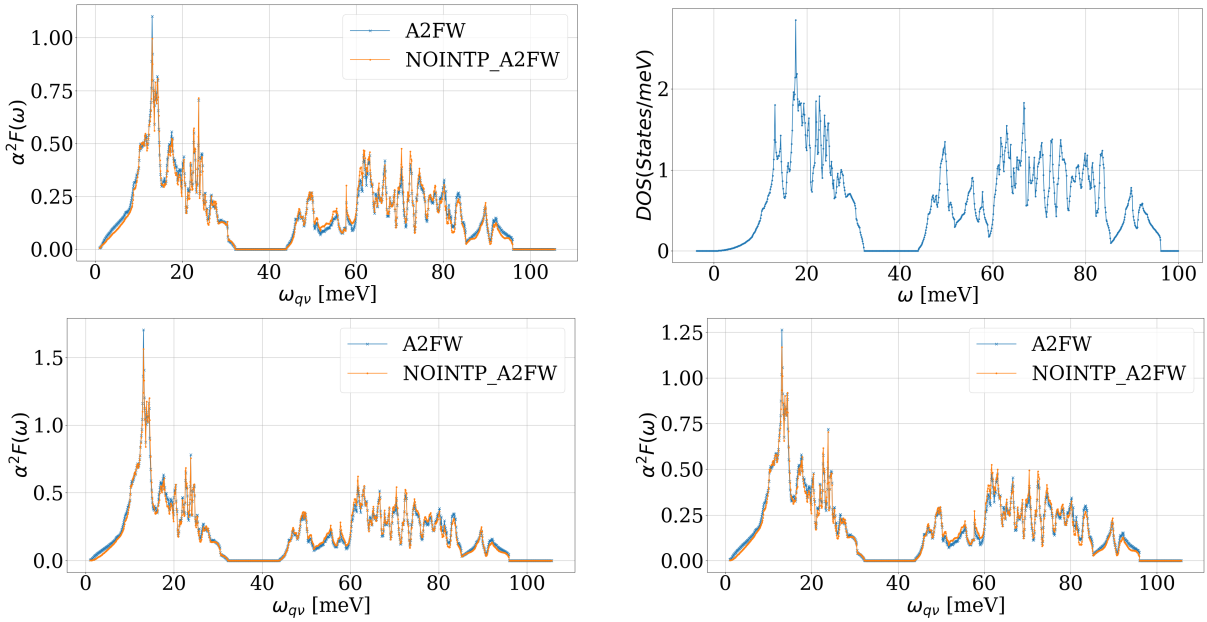

Figure 5.8.2: The spectral function α^2F as a function of the frequency ω is shown here for tetrahedron smearing (top,left) and Gaussian smearing with the factors 0.01 (bottom, left) and 0.005 (bottom,right) in comparison with the phonon density of states (top, right). A2FW stands for the additionally Fourier interpolated results, while NOINTP_A2FW stands for the explicitly interpolated results.

One can see one major difference, which is that the frequency at which the highest spectral density occurs is different from where the biggest peak for the phonon density is. Furthermore, it seems that the low frequency for the spectral function α^2F shows partly linear behavior, while it should show a parabolic like curve like for the phonon density of states. This is investigates further for it could be the numerical reason behind this unreasonably low logarithmic frequency ω_{log}.
In order to do so, the ω_{log} is solved by hand, whereas the low frequency parts of the α^2F function are removed or substituted by the phDOS part that is fitted to the spectral function. For that reason, the trapezoidal rule is deployed to calculate the integral found in equation (4). The integration method is compared to the Simpson's rule, but the differences were negligible. This framework will be deployed for the rest of this work for the underestimation of the logarithmic frequency is probably due to a numerical error stemming from, we suspect, wrong interpolation.

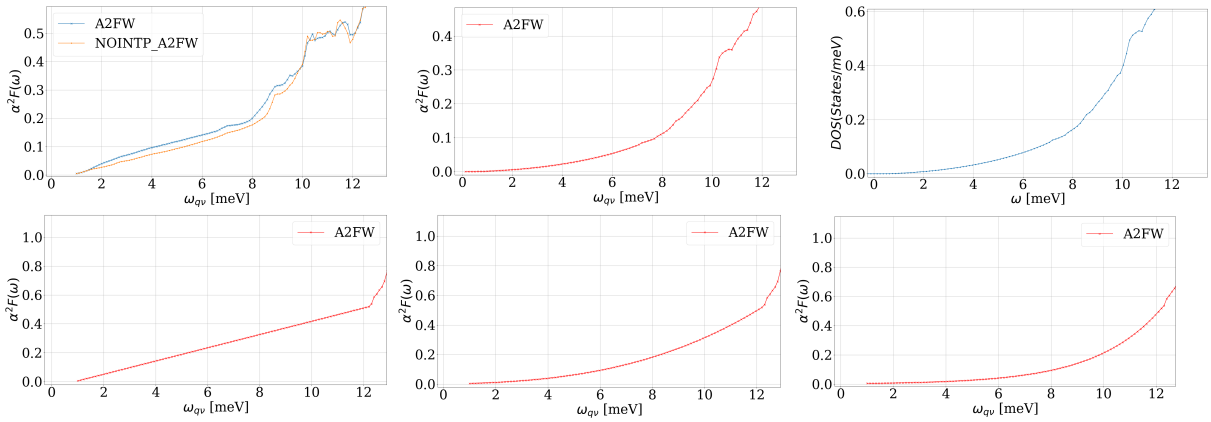

Figure 5.8.3: The spectral function α^2F as a function of the frequency ω is shown here for tetrahedron smearing. The left picture shows the original low frequency part of the spectral function. In the middle (red) the phonon DOS low frequency curve has been fitted to the spectral function until 12 meV in comparison with the phonon density of states beginning (right in blue).The three bottom graphs stand for when the spectral density curve until 12 meV is substituted by a function $y = x^p$ with the power p= 1 (left, 5.$\omega_{\log}$, linear), p=3 (middle, 6. $\omega_{\log}$, cubic) and p = 100 (right, 7. $\omega_{\log}$, upper limit).

It is also tried to substitute the low frequency part with a function $y = x^p$ with the power p= 1, reproducing extremely nonphysical linear behavior, p=3 to see how a cubic function would influence the $\omega_{\log}$ and p = 100, to see how the logarithmic frequency will change for this extreme case. The results are presented in the following table:

Table 5.8.2: Recalculated results, while the isotropic λ is kept. The differently calculated $\omega_{\log}$ stand for when the spectral density is neglected until 9.5 meV, 10.9 meV, 12 meV. The forth $\omega_{\log}$ stands for when the first part until 12 meV is substituted by a phonon DOS-like curve. The following three $\omega_{\log}$-values stand for when the spectral density curve until 12 meV is substituted by a function $y = x^p$ with the power p= 1 (5.$\omega_{\log}$, linear), p = 3 (6. $\omega_{\log}$) and p = 100 (7. $\omega_{\log}$ upper limit). The first column per smearing method called "Explicit interpolation" is interpolated but then the matrix elements are taken explicitly on the **k**-point grid and the second one is Fourier interpolated with respect to the DDB q-points (interpolated by ph_ngqpt).

	Tetrahedron smearing		Gaussian smearing 0.01 Ha		Gaussian smearing 0.005 Ha	
	Explicit Interpolation	Fourier interpolation	Explicit Interpolation	Fourier interpolation	Explicit Interpolation	Fourier interpolation
Isotropic λ	0.773	0.8188	0.9131	0.9695	0.8002	0.8519
1. $\omega_{\log}$ [K]	3.7377	7.0081	1.6492	3.3455	2.3230	4.7624
2. $\omega_{\log}$ [K]	11.5453	20.3360	5.1030	9.6936	7.2109	13.7991
3. $\omega_{\log}$ [K]	39.9635	65.7114	20.7292	36.2945	26.7961	47.3532
4. $\omega_{\log}$ [K]	1.1450	2.2924	0.2730	0.6148	0.4783	1.0793
5. $\omega_{\log}$ [K]	0.0049	0.0133	0.0004	0.0013	0.0015	0.0048
6. $\omega_{\log}$ [K]	0.3514	0.7510	0.0978	0.1820	0.1851	0.4424
7. $\omega_{\log}$ [K]	1.8764	3.6552	0.8398	1.7717	1.2182	2.5974

The first three values of $\omega_{\log}$ stand for when a part of the low frequency part is neglected. This is rather not physically reasonably, but it also shows the big influence of the low frequency part. The average logarithmic frequency $\omega_{\log}$ is getting higher the more low frequency part is neglected due to the logarithmic part. The function was cut at different parts and substituted for the phonon density of state function, which did impact the $\omega_{\log}$, the value is rising, but still not high enough. Using the phonon DOS is physical for the Eliashberg function is the weighted phonon DOS. Due to the fact that the average logarithmic frequency is still not high enough, the numerical error is probably not only affecting the low frequency part. Lastly, it is attempted to model the low frequency behavior to see its effect on the logarithmic frequency $\omega_{\log}$. The first value that is calculated for perfectly linear behavior is very small and it is calculated to show the lower limit of $\omega_{\log}$ when just changing the low frequency part. This 5. $\omega_{\log}$ will not be taken into account for the final table. When applying a function with the power 100, the $\omega_{\log}$ is rising towards more realistic values, but still not sufficiently large. The value for $\omega_{\log}$ is most realistic with neglecting the low frequency part, but doing this is hardly physically justifiable. This also leads to a less accurate description. Therefore, the 3. $\omega_{\log}$ is neglected for the results because it seems unrealistic to take away all the frequencies until 12 meV. Furthermore, it is hard to compare with next results that do not neglect such a big part of the spectral density.

From the shown data, one can deduce following superconducting parameter:

Table 5.8.3: superconducting parameters found for taking into account a smearing for the input phonon files of 0.05 Ha. The Debye temperature is an output from the phonon density of states calculation and the two values stem from the calculation from partial sums and the second value stems from the phDOS directly.

Isotropic λ	0.77-0.97
$\omega_{\log}$	0.13-20.34 K
Empirical parameter μ^*	0.1
McMillan critical temperature	0.01-1.35 K
Debye-temperature from partial sums-phDOS	169.66-193.75 K
Critical temperature calculated from equation (3.79)	6.07-10.65 K

One can see how the Debye-temperature is much higher then the logarithmic frequency $\omega_{\log}$. The originally calculated $\omega_{\log}$ is too small to be realistic and from estimating another low frequency part, one can gain more realistic results that lead to a critical temperature that is closer to the experimentally found critical temperature of 3 K.[2] The calculation of the critical temperature with equation (3.79) leads to a overestimation of the critical temperature for it does not take the low frequency part of the spectral function correctly into account, which we have shown to be calculated wrongly anyways.

Data set smearing 0.01 Ha

The convergence is assumed to be similar like for the previous data sets. Therefore, the results for the **k**-point set 10x10x30 are further investigated in the same fashion like in the previous section.

Table 5.8.4: Results for the isotropic parameters for different interpolation techniques and smearing techniques. 1. $\omega_{\log}$ stands for neglecting the low frequency beneath 6.8 meV, 2. $\omega_{\log}$ neglects the spectra density beneath 8 meV, while the third value integrates the phonon density of states values fitted accordingly until a frequency of 8 meV. The following three $\omega_{\log}$-values stand for when the spectral density curve until 8 meV is substituted by a function $y = x^p$ with the power p = 1 (4. $\omega_{\log}$, linear), p =3 (5. $\omega_{\log}$) and p =100 (6. $\omega_{\log}$ upper limit). The first column per smearing method called "Explicit interpolation" is interpolated but then the matrix elements are taken explicitly on the **k**-point grid and the second one is Fourier interpolated with respect to the DDB q-points (interpolated by ph_ngqpt).

	Tetrahedron smearing		Gaussian smearing 0.01 Ha		Gaussian smearing 0.005 Ha	
	Explicit Interpolation	Fourier interpolation	Explicit Interpolation	Fourier interpolation	Explicit Interpolation	Fourier interpolation
T_c [K]	$2.022 \cdot 10^{-2}$	$3.506 \cdot 10^{-2}$	$4.18 \cdot 10^{-3}$	$3.43 \cdot 10^{-3}$	$3.05 \cdot 10^{-3}$	$2.57 \cdot 10^{-3}$
Isotropic λ	0.8729	9.9436	1.1572	1.2469	0.9727	1.0588
$\omega_{\log}$ [K]	0.04119	0.03506	0.0531	0.0394	0.0507	0.0372
1. $\omega_{\log}$ [K]	3.5351	8.3086	2.1366	5.0336	2.6017	8.3138
2. $\omega_{\log}$ [K]	17.5298	36.5412	11.0723	23.1718	13.2917	30.1719
3. $\omega_{\log}$ [K]	0.3094	0.8730	0.1365	0.3919	0.1982	0.6335
4. $\omega_{\log}$ [K]	0.0001	0.0003	0.0000	0.0001	0.0000	0.0002
5. $\omega_{\log}$ [K]	0.0383	0.1264	0.0220	0.0720	0.0270	0.1017
6. $\omega_{\log}$ [K]	0.3640	1.0145	0.2757	0.7526	0.2913	0.9022
Positive moments of $\alpha^2F(\omega)$						
λ (ω^2)	$7.79 \cdot 10^{-7}$	$7.79 \cdot 10^{-7}$	$1.01 \cdot 10^{-6}$	$1.01 \cdot 10^{-6}$	$8.77 \cdot 10^{-6}$	$8.77 \cdot 10^{-7}$
λ (ω^3)	$1.69 \cdot 10^{-9}$	$1.72 \cdot 10^{-9}$	$2.16 \cdot 10^{-9}$	$2.19 \cdot 10^{-9}$	$1.90 \cdot 10^{-9}$	$1.93 \cdot 10^{-9}$
λ (ω^4)	$4.25 \cdot 10^{-12}$	$4.38 \cdot 10^{-12}$	$5.38 \cdot 10^{-12}$	$5.55 \cdot 10^{-12}$	$4.76 \cdot 10^{-12}$	$4.91 \cdot 10^{-12}$
λ (ω^5)	$1.13 \cdot 10^{-14}$	$1.18 \cdot 10^{-14}$	$1.42 \cdot 10^{-14}$	$1.49 \cdot 10^{-14}$	$1.26 \cdot 10^{-14}$	$1.32 \cdot 10^{-14}$

Again the calculated logarithmic frequency $\omega_{\log}$ is unrealistically small, even smaller then for the smearing 0.05 Ha data set. Therefore, again tests were made where the low frequency part has been neglected. One sees how neglecting parts is impacting the $\omega_{\log}$ positively, but the low frequency parts play an important role due to the logarithm. In the following figure a description of the deployed substitution is shown.

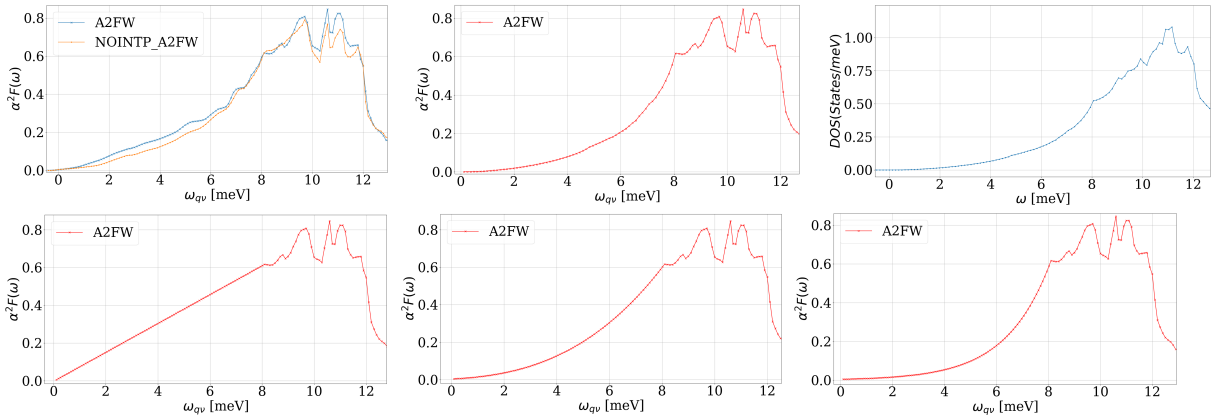

Figure 5.8.4: The spectral function α^2F as a function of the frequency ω is shown here for tetrahedron smearing. The left picture shows the original low frequency part of the spectral function. In the middle (red) the phonon DOS low frequency curve has been fitted to the spectral function until 8 meV in comparison with the phonon density of states beginning (right in blue). The bottom three spectral density estimations stand for when the spectral density curve until 8 meV is substituted by a function $y = ^p$ with the power p =1 (left, bottem 4.$\omega_{\log}$, linear), p =3 (middle, bottom 5. $\omega_{\log}$) and p =100 (right, bottom 6. $\omega_{\log}$ upper limit).

One can see how the slope of the α^2F-function is much steeper at low frequencies for this data set. This comes from the unstable phonon mode that leads to more population of lower laying bands. Fitting the phonon DOS curve onto the spectral function curve, does impact the curve a little as can be seen. The value of $\omega_{\log}$ is rising as well. But this still leads to a very low $\omega_{\log}$. It shows how big the impact of the low frequency modes is. A small change leads to an around 2-10 times bigger $\omega_{\log}$ (Compare calculated $\omega_{\log}$ with 3. $\omega_{\log}$ in table 5.8.4). This could mean that even when deploying a more parabolic kind of low frequency spectral function, it might still not be parabolic enough. The behavior is also shown for fitting a function like described in the previous section. We see similar tendencies, where the $\omega_{\log}$ is going from very low for a linear growth to more realistic, but still too low values for a more extreme parabolic growth, that also resembles the phonon DOS more.

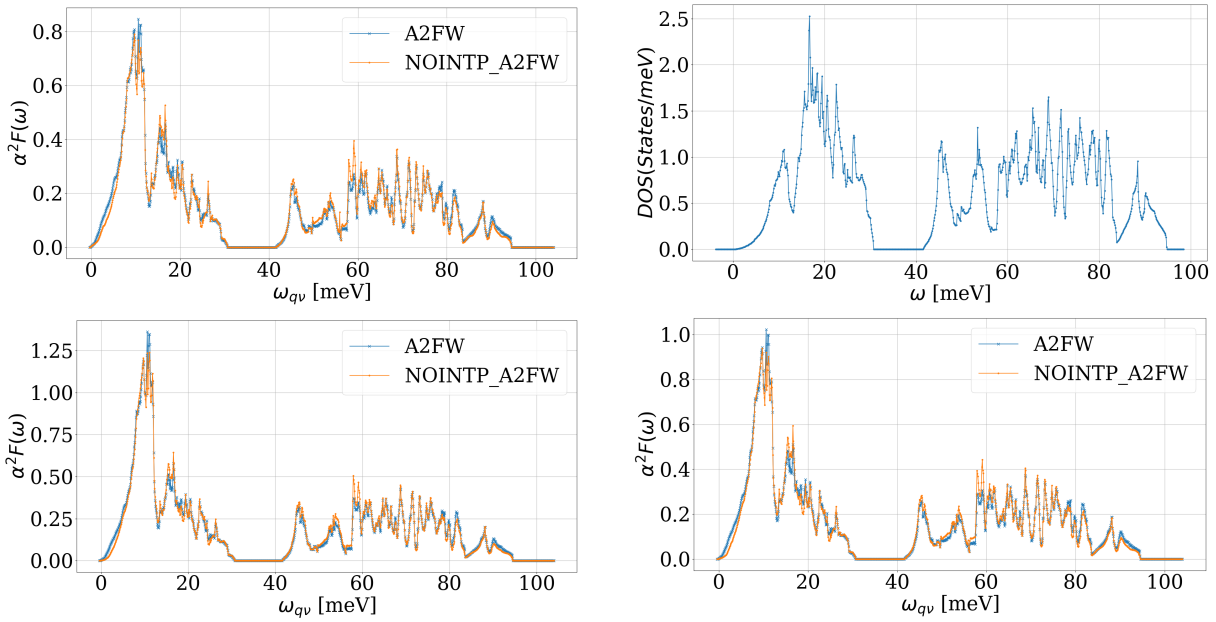

Figure 5.8.5: The spectral function α^2F as a function of the frequency ω is shown here for tetrahedron smearing (top,left) and Gaussian smearing with the factors 0.01 (bottom, left) and 0.005 (bottom,right) in comparison with the phonon density of states (top, right).A2FW stands for the additionally Fourier interpolated results, while NOINTP_A2FW stands for the explicitly interpolated results.

Here, it becomes very clear how, like for the data set 0.05 Ha, the peak highest peak for the phonon density of states is not the highest peak in the spectral function. The following superconducting parameters are recalculated:

Table 5.8.5: superconducting parameters found for taking into account a smearing for the input phonon files of 0.05 Ha. The Debye temperature is an output from the phonon density of states calculation and the two values stem from the calculation from partial sums and the second value stems from the phDOS directly.

Isotropic λ	0.87-1.16
$\omega_{\log}$	0.04-36.54 K
Empirical parameter μ^*	0.1
McMillan critical temperature	0.00-3.14 K
Debye-temperature from phDOS-partial sums	82.06-161.20 K
Critical temperature calculated from equation (3.79)	3.74-11.46 K

The values for the $\omega_{\log}$ are again roughly estimated. The calculated $\omega_{\log}$ from the calculation are lower, for the Eliashberg function curve lays in lower levels then for the data set 0.05 Ha, but this does not impact the final results for the $\omega_{\log}$ had to be approximated. The estimation of the critical temperature is acceptable. The calculation with the Debye-temperature gives a good estimation of the critical temperature and furthermore, is the Debye-temperature, much more accurate then the estimated logarithmic frequency because it is gained through the very highly converged phonon DOS.

Final results

In the spectral function, one can see how the low frequency phonon modes have a big impact on the superconductivity. These stem mainly from the tantalum. Therefore, one can compare the results with the elemental Tantalum, that has the following superconducting parameters, that were calculated previously:[10]

Table 5.8.6: Superconducting parameters predicted in this work in comparison with experimental results for η-Ta_2N_3[2] and also compared to the known superconducting parameters of Tantalum.[10]

	Predicted η-Ta_2N_3	Experimental η-Ta_2N_3[2]	Predicted Ta[10]	Experimental Ta[53]
Isotropic λ	0.77-1.16	/	0.80-0.85	/
$\omega_{\log}$	0.04-36.54 K	/	122-125 K	/
Empirical parameter μ^*	0.1	/	0.1	/
McMillan critical temperature	0.00-3.14 K	$\approx$ 3 K	5.0-6.7 K	4.457 $\pm$ 0.003 K
Debye-temperature from phDOS	82.06-193.75 K	/	/	/
Critical temperature calculated from equation (3.79)	3.74-10.65 K	/	/	/

The critical temperature is well underestimated due to the systematic underestimation of the $\omega_{\log}$. But nevertheless, a rough approximation did lead to a results being close to experimental findings. One can see how the originally calculated $\omega_{\log}$ is not correct and how small estimations of the low frequency part leads to more accurate results, that are closer to reality. Still,

more in depth understanding of the numerical error behind must be build, especially seeing how the logarithmic frequency $\omega_{\log}$ still differs strongly in comparison to the elemental Tantalum, although one could assume that the lower atomic mass nitrogen rather tends to bring the logarithmic frequency to higher values. The isotropic λ is on the other hand in the same range. Seeing how a logarithmic $\omega_{\log}$ of 36.54 K leads to a critical temperature of 3.14 K, we can assume that it should be around that value rather then the lower limit we set for it. Furthermore, it is interesting to see how the critical temperature given by the original McMillan formula (3.79) is also very accurate. It is suggested that using this equation for predictive purposes might be more meaningful. For calculation of the following system it is kept in mind, that the critical temperature calculated with the logarithmic frequency $\omega_{\log}$ is rather strongly underestimated, while the critical temperature calculated with the Debye temperature is overestimated.

6 Orthorhombic Ta_2N_3 at 26.065 GPa

The η-Ta_2N_3 is investigated under pressure in order to compare the results with experimental ones by Zerr *et al.*[2]. Furthermore, it is of interest to see the superconducting behavior in dependence on the pressure

6.1 Optimisation

In the following, the structure under pressure was optimized twice. First of all, the atomic coordinates were optimized with keeping the literature cell parameter (for the ambient structure) constant and afterwards a relaxation of both the atomic coordinates and the cell parameter was conducted at 26.065 GPa pressure. The following cell parameters and atomic coordinates were used for further calculations:

Table 6.1.1: Final atomic coordinates for the η-Ta_2N_3 under pressure in comparison with the atomic coordinates in brackets found for the ambient structure shown in section 5.1.

Atom	x	y	z
Ta1	0.312 (0.313)	-0.021 (-0.021)	0.25
Ta2	0.507 (0.505)	0.307 (0.306)	0.25
N1	0.873 (0.875)	0.047 (0.046)	0.25
N2	0.546 (0.549)	0.879 (0.879)	0.25
N3	0.191 (0.200)	0.216 (0.220)	0.25

The new cell parameter are the following:

- a = 8.57 Å (8.18 Å)
- b = 8.46 Å (8.22 Å)
- c = 3.08 Å (3.00 Å)

The unit cell parameter are compared to the unit cell parameters found for the ambient structure. They are smaller as expected for a structure under pressure. This leads to a volume of 170.52 $Å^3$, which is as expected smaller then the unit cell volume at ambient pressure.

6.2 Electronic structure

The density of states for the electronic structure were calculated for two smearing values 0.005 Ha and 0.05 Ha. Like for the ambient structure one could only notice a change in Fermi-level. For the low smearing factor the Fermi-level was 11.990 eV while for the high smearing, the value was lower (11.759 eV). The result is shown for the high smearing for in the next section, major instabilities are discovered for the low smearing. In comparison with the η-Ta_2N_3 at ambient conditions, this structure shows higher levels of DOS, but same characteristics.

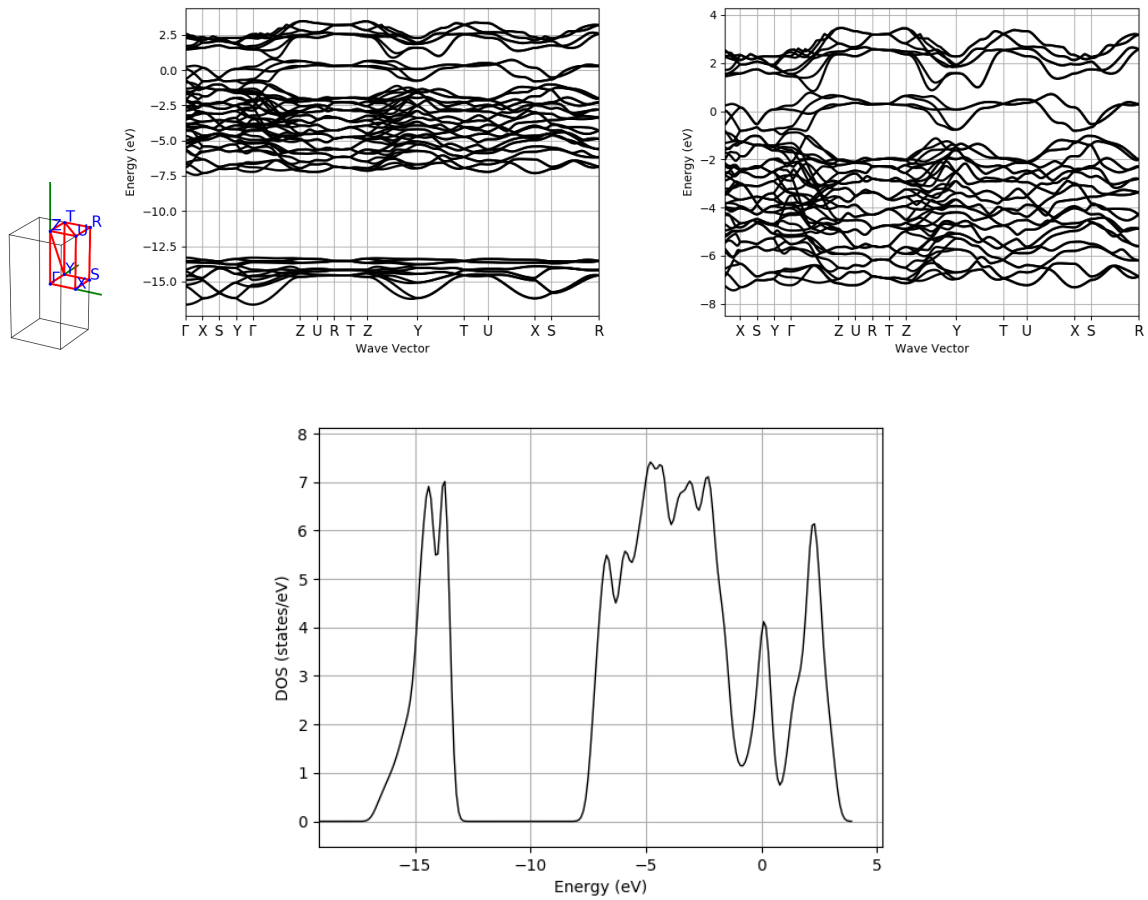

Figure 6.2.1: Electron band structure and Density of states for Ta_2N_3 at 26.065 GPa for a smearing of 0.05 Ha, **k**-point grid 6x6x18. The Fermi-level of 11.759 eV is set as zero-point

6.3 Vibrational properties

The frequencies at Γ were calculated. The three unstable modes were found for smearing = 0.005 Ha. One can freeze these modes and a new optimization of the structure can be repeated in search for a stable structure. When propagating the displacement of the atoms, the maximum change in reduced atomic coordinates was 0.02, while the cell parameter changed around 0.005 Å, which is rather negligible.
As for the Ta_2N_3, a test regarding different smearing parameters were made. Choosing a smearing of 0.01 revealed two unstable Phonon modes at around -51 cm^{-1}, which is a bit higher in energy then for the smearing 0.005. A new calculation with a higher smearing of 0.05 revealed stability at Γ-point. The structure might follow a stability curve in a pressure/temperature dependent phase diagram, which would explain the higher smearing needed for stabilization for the structure under pressure. The phonon modes at Γ do change a lot for the two smearing values. The results are shown in the following tables:

Table 6.3.1: Raman active Phonon modes at Γ-point for different cold smearing factors shown with their activities and symmetry groups.

6x6x18, 0.005Ha Phonon energy[cm^{-1}]	6x6x18, 0.05Ha Phonon energy[cm^{-1}]	Activity	D_{2h}	6x6x18, 0.005Ha Phonon energy[cm^{-1}]	6x6x18, 0.05Ha Phonon energy[cm^{-1}]	Activity	D_{2h}

-56.83	49.8	xy,J_z	B_{1g}	370.6	357.2	yz, J_x	B_{3g}
75.93	72.4	xz, J_y	B_{2g}	398.7	402.1	xy,J_z	B_{1g}
97.22	104.5	x^2,y^2,z^2	A_g	421.1	431.2	xy,J_z	B_{1g}
97.63	97.0	xz, J_y	B_{2g}	423.7	421.0	xz, J_y	B_{2g}
106.4	99.5	yz, J_x	B_{3g}	446.0	443.0	xz, J_y	B_{2g}
126.1	128.8	x^2, y^2, z^2	A_g	464.1	465.0	yz, J_x	B_{3g}
127.4	160.1	xy,J_z	B_{1g}	487.6	491.1	x^2,y^2,z^2	A_g
130.8	135.2	x^2,y^2,z^2	A_g	503.2	513.2	xy,J_z	B_{1g}
153.0	166.0	xy,J_z	B_{1g}	514.5	528.1	xy,J_z	B_{1g}
174.5	176.4	xy,J_z	B_{1g}	523.6	562.3	xy,J_z	B_{1g}
190.2	206.0	x^2,y^2,z^2	A_g	532.3	544.3	x^2,y^2,z^2	A_g
285.7	286.4	xz, J_y	B_{2g}	572.7	586.4	x^2,y^2,z^2	A_g
312.2	332.6	yz, J_x	B_{3g}	626.9	643.2	xy,J_z	B_{1g}
315.2	327.5	x^2,y^2,z^2	A_g	638.6	650.4	x^2,y^2,z^2	A_g
349.6	361.2	x^2,y^2,z^2	A_g				

Table 6.3.2: IR-active Phonon modes at Γ-point or different cold smearing factors shown with their activities and symmetry groups.

6x6x18, 0.005Ha Phonon energy[cm^{-1}]	6x6x18, 0.05Ha Phonon energy[cm^{-1}]	Activity	D_{2h}	6x6x18, 0.005Ha Phonon energy[cm^{-1}]	6x6x18, 0.05Ha Phonon energy[cm^{-1}]	Activity	D_{2h}
-76.70	73.4	y	B_{2u}	396.7	394.7	x	B_{3u}
77.03	74.0	z	B_{1u}	405.7	424.2	x	B_{3u}
4 95.16	104.5	x	B_{3u}	407.1	412.4	y	B_{2u}
108.7	114.5	z	B_{1u}	446.8	468.4	z	B_{1u}
126.2	162.9	x	B_{3u}	458.3	476.6	x	B_{3u}
141.8	145.0	y	B_{2u}	500.8	540.0	y	B_{2u}
159.8	178.2	y	B_{2u}	510.7	502.5	z	B_{1u}
169.2	181.4	x	B_{3u}	544.0	559.7	y	B_{2u}
285.0	295.9	x	B_{3u}	544.1	570.0	z	B_{3u}
286.7	274.9	y	B_{2u}	589.5	603.8	y	B_{2u}
331.0	325.3	z	B_{1u}	660.4	675.1	x	B_{3u}
359.0	372.9	y	B_{2u}				

One can see how due to the smearing, the phonon modes at Γ not only stabilize but also change their value noteworthy. The instability at the Z-point seems to influence all the other modes as well.

Table 6.3.3: Silent modes at Γ-point.

6x6x18, 0.005Ha Phonon energy [cm^{-1}]	6x6x18, 0.05Ha Phonon energy[cm^{-1}]	Activity	D_{2h}	6x6x18, 0.005Ha Phonon energy [cm^{-1}]	6x6x18, 0.05Ha Phonon energy[cm^{-1}]	Activity	D_{2h}
0.0	0.0	yz, J_x	B_{3g}	96.41	100.2	/	A_u
0.0	0.0	y	B_{2u}	382.2	393.4	/	A_u
0.0	0.0	z	B_{3u}	423.3	437.0	/	A_u
88.67	92.9	/	A_u	495.5	490.9	/	A_u

The phonondispersion was computed for a lower k-point grid of 6x6x18 for 0.005 Ha smearing. It shows various unstable modes. Their origin might be the unstable K-point mode at ambient pressure.

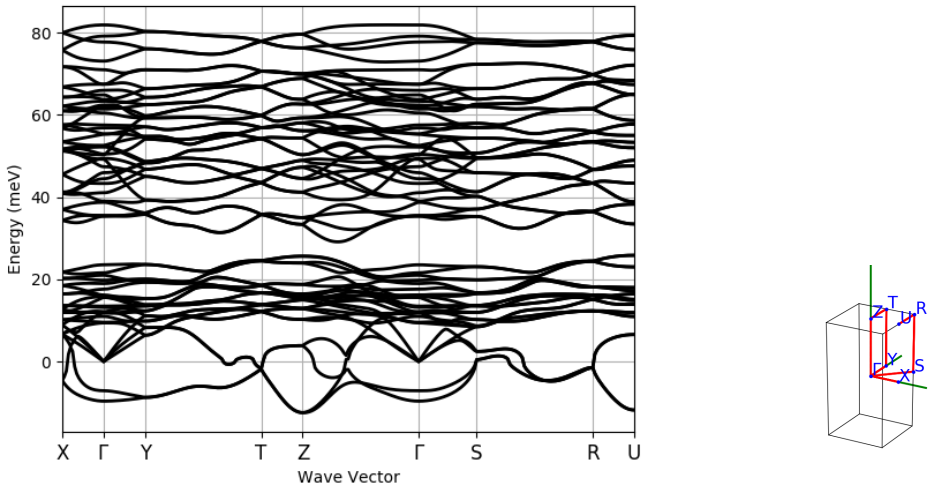

Figure 6.3.1: Phonondispersion for Ta_2N_3 at 26.065 GPa with a smearing of 0.005 Ha.

A new calculation was conducted, for as previously described, the modes become stable at higher smearing which is necessary to be able to conduct a superconductivity calculation.

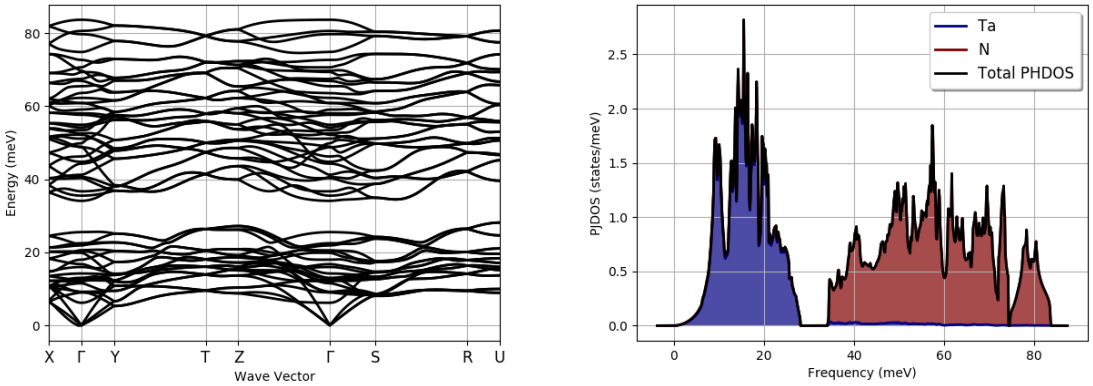

Figure 6.3.2: Phonondispersion and phonon density of states for the Ta_2N_3 at 26.065 GPa with smearing=0.05 Ha.

Due to the stability, the DDB-files for smearing 0.05 Ha are used to compute the superconductivity parameters.

6.4 Superconductivity

The convergence is assumed to be similar like for the previous datasets. Therefore, the results for the **k**-point set 10x10x30 are further investigated in the same fashion like in the previous section. $\omega_{\log}$ is again calculated with the help of the trapezoid rule. We do not include a dataset for 0.01 Ha smearing for it shows instabilities at Γ-point leading to the fact that no superconductivity calculation can be realized.

Table 6.4.1: Results for the isotropic parameters for different interpolation techniques and smearing techniques. 1. $\omega_{\log}$ stands for neglecting the low frequency beneath 5.4 meV, 2. $\omega_{\log}$ neglects the spectra density beneath 8.1 meV, while the third value integrates the phonon density of states values fitted accordingly until a frequency of 8.1 meV.

	Tetrahedron smearing		Gaussian smearing 0.01 Ha		Gaussian smearing 0.005 Ha	
	Explicit Interpolation	Fourier interpolation	Explicit Interpolation	Fourier interpolation	Explicit Interpolation	Fourier interpolation
T_c [K]	$2.172344 \cdot 10^{-3}$	$2.247395 \cdot 10^{-3}$	$5.29 \cdot 10^{-3}$	$4.77 \cdot 10^{-3}$	$3.17 \cdot 10^{-3}$	$2.99 \cdot 10^{-3}$
Isotropic λ	0.8248	0.8650	1.2743	1.3498	0.8952	0.9554
$\omega_{\log}$ [K]	0.0498	0.0466	0.0591	0.0499	0.0615	0.0513
1. $\omega_{\log}$ [K]	0.5891	1.0863	0.2128	0.5276	0.3049	0.7298
2. $\omega_{\log}$ [K]	7.7830	12.7327	3.4610	6.5525	3.8109	7.77984
3. $\omega_{\log}$ [K]	0.3490	0.6595	0.0917	0.2128	0.1475	0.3696
Positive moments of $\alpha^2F(\omega)$						
λ (ω^2)	$5.79 \cdot 10^{-7}$	$5.79 \cdot 10^{-7}$	$8.60 \cdot 10^{-7}$	$8.60 \cdot 10^{-7}$	$6.67 \cdot 10^{-7}$	$6.67 \cdot 10^{-7}$
λ (ω^3)	$1.04 \cdot 10^{-9}$	$1.05 \cdot 10^{-9}$	$1.52 \cdot 10^{-9}$	$1.54 \cdot 10^{-9}$	$1.21 \cdot 10^{-9}$	$1.22 \cdot 10^{-9}$
λ (ω^4)	$2.20 \cdot 10^{-12}$	$2.29 \cdot 10^{-12}$	$3.22 \cdot 10^{-12}$	$3.29 \cdot 10^{-12}$	$2.57 \cdot 10^{-12}$	$2.64 \cdot 10^{-12}$
λ (ω^5)	$5.03 \cdot 10^{-15}$	$5.36 \cdot 10^{-15}$	$7.35 \cdot 10^{-15}$	$7.62 \cdot 10^{-15}$	$5.87 \cdot 10^{-14}$	$6.18 \cdot 10^{-14}$

Again the calculated logarithmic frequency $\omega_{\log}$ is unrealistically small. Therefore, again tests were made where the low frequency part has been neglected. One sees how neglecting parts is impacting the $\omega_{\log}$ positively, but the low frequency parts play an important role due to the logarithm, therefore neglecting the low frequency part is still not justifiable physically. The modelling of the low frequency part like shown for the structure at ambient pressures, is not repeated here, for they did not impact eh final result. In the following figure a description of the deployed substitution is shown:

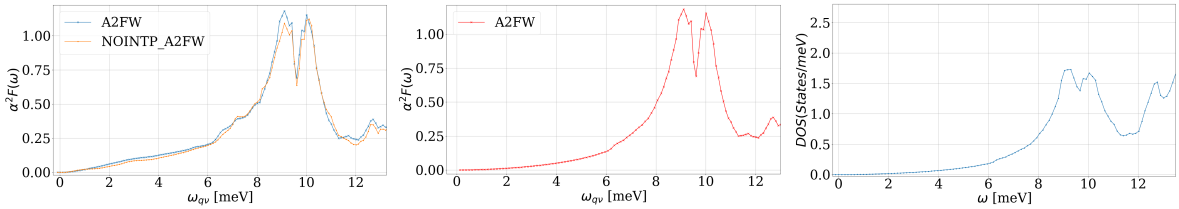

Figure 6.4.1: The spectral function α^2F as a function of the frequency ω is shown here for tetrahedron smearing. The left picture shows the original low frequency part of the spectral function. In the middle (red) the phonon DOS low frequency curve has been fitted to the spectral function until 8.1 meV in comparison with the phonon density of states beginning (right in blue).

Fitting the phonon DOS curve onto the spectral function curve, does lead to an improvement of the logarithmic frequency $\omega_{\log}$. The value rises almost in any case more then 10-times. The value is still very low, so that it is assumed that the numerical error does not only impact the low frequency part.

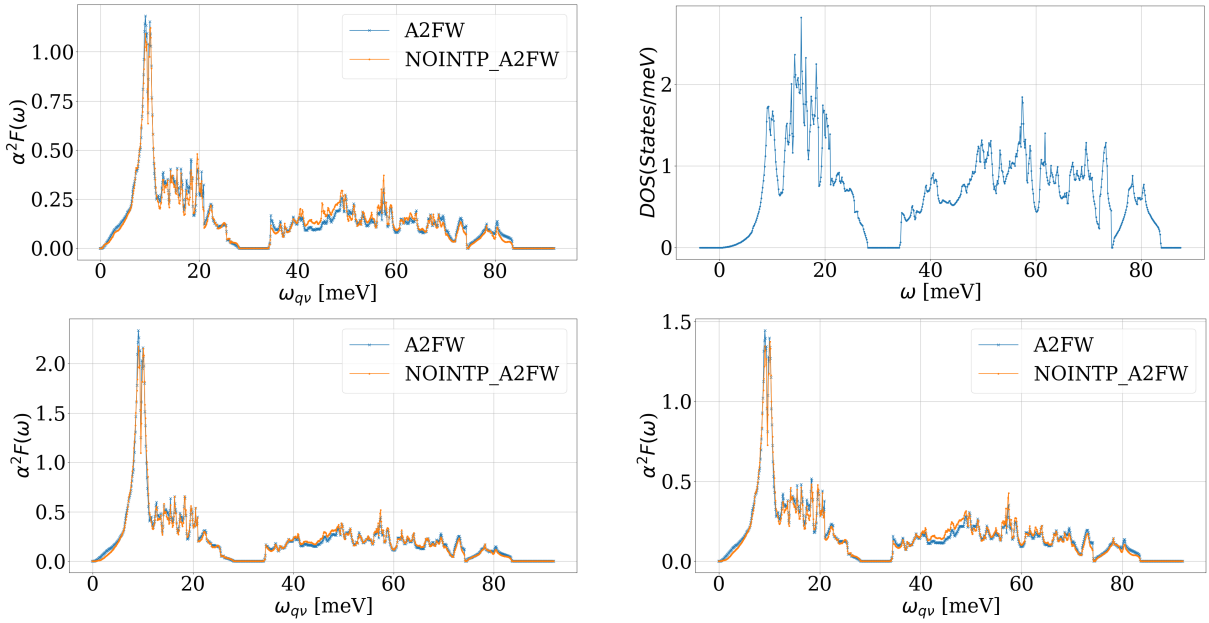

Figure 6.4.2: The spectral function α^2F as a function of the frequency ω is shown here for tetrahedron smearing (top,left) and Gaussian smearing with the factors 0.01 (bottom, left) and 0.005 (bottom,right) in comparison with the phonon density of states (top, right).A2FW stands for the additionally Fourier interpolated results, while NOINTP_A2FW stands for the explicitly interpolated results.

In figure 6.4.2 we can see how the low frequency part is indeed very linear and steep, while it should be more parabolic. In the following the results are listed. The smearing seems to be a very sensitive parameter and therefore, we just compared to the results achieved in similar fashion. The results are in good agreement, while the EPC seems to be higher for the structure under pressure. All in all all values are in similar ranges. For many compounds, one can see a rise in critical temperature with pressure applied. This could not be confirmed in our case, but it also can't be ruled out.

Table 6.4.2: Superconducting parameters compared for the η-Ta_2N_3 at ambient pressures and under 26.065 GPa pressure, while only data sets with 0.05 Ha smearing factor for the input files are taken into account.

	η-Ta_2N_3 at ambient pressure	η-Ta_2N_3 under pressure
Isotropic λ	0.77-0.97	0.82-1.35
$\omega_{\log}$	0.27-20.34 K	0.09-12.73 K
Empirical parameter μ^*	0.1	0.1
McMillan critical temperature	0.012-1.350 K	0.006-1.305 K
Debye-temperature from phDOS/partial sums	169.66-193.75 K	94.31-139.48 K
Critical temperature calculated from equation (3.79)	6.07-10.65 K	3.38-11.83 K

7 Tetragonal Ta_2N_3

Random search sampling performed by Jiang *et al.*[9] unveiled a low energy structure of the Ta_2N_3 displaying a less densely packed tetragonal structure of the space group 115 $P\bar{4}m2$. It is predicted to have a higher stability at ambient conditions then the orthorhombic Ta_2N_3. It is predicted that this structure transforms into the orthorhombic Ta_2N_3 at low pressures of 7.7 GPa.[9]
From previous work, a calculation was already conducted around this compound and superconductivity was predicted. In the following the old results calculated with Quantum Espresso are compared with the new ones that are obtained from Abinit to get to the bottom of the wrong logarithmic frequencies that are obtained.[16,17,10]

7.1 Convergence study

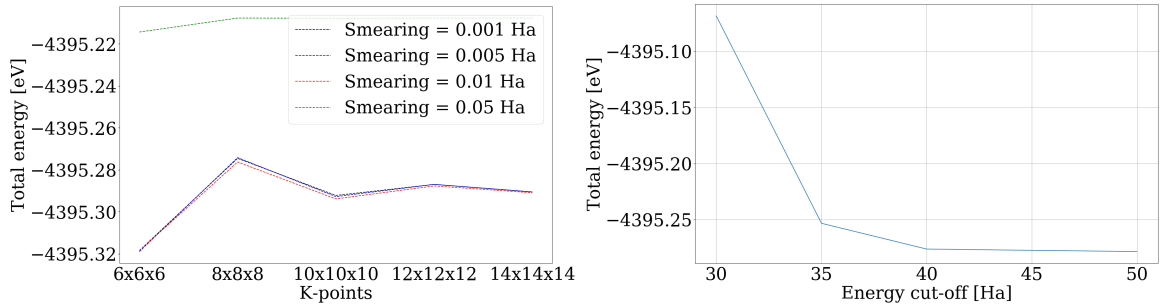

Figure 7.1.1: **K**-point and Smearing convergence (left) and Energy cut-off convergence (right).

Due to the size of the system, the variation of **k**-points was not limiting the calculation as much as for the big orthogonal Ta_2N_3 system. Therefore, a **k**-point set of 12x12x12 was chosen with a smearing of 0.01 Ha, for the curve converges and does not change much for higher a **k**-point grid. The error stemming from the difference towards the next higher total energy is $\pm\ 5 \cdot 10^{-6}$ eV. All in all, the **k**-point and smearing convergence does not look very typical. And also for very low smearing, the energy lays much higher while the other three smearing values show almost same behavior. For the energy cut-off, a value of 40 Ha has been chosen producing an error of $\pm\ 5 \cdot 10^{-4}$ eV.

7.2 Optimisation

In order to avoid forces acting onto the atoms, an optimization has been conducted giving the following atomic coordinates and cell parameter.

Table 7.2.1: Optimized atomic coordinates with the literature values shown in the brackets.[9]

Atom	x	y	z
V1	0.500	0.000	0.756 (0.756)
N1	0.500	0.000	0.140 (0.140)
N2	0.500	0.500	0.500

The atomic coordinates are exactly the same like in the literature, while one has to note that the results are rounded off to 3 significant digits.[9] The new cell parameter are the following:

- a = b = 2.98 Å
- c = 5.81 Å

Jiang *et al.*[9] found the unit cell parameter to be 2.99 Å and 5.82 Å, which differs 0.01 Å from our optimized factors. The cell volume is 51.59 Å which is around $\frac{1}{4}$th of the unit cell volume of the orthorhombic Ta_2N_3.

7.3 Electronic structure

The electronic parameters were further investigated and compared with previous results, while as mentioned earlier, a **k**-point grid of 12x12x12 was used in combination with a cold smearing factor of 0.01 Ha. The result is compared with previous results, that utilized the Quantum Espresso program, where a **k**-point grid of 8x8x8 was used in combination with Marzari-Vanderbilt smearing with a factor of 0.01 Ha for the band calculation.

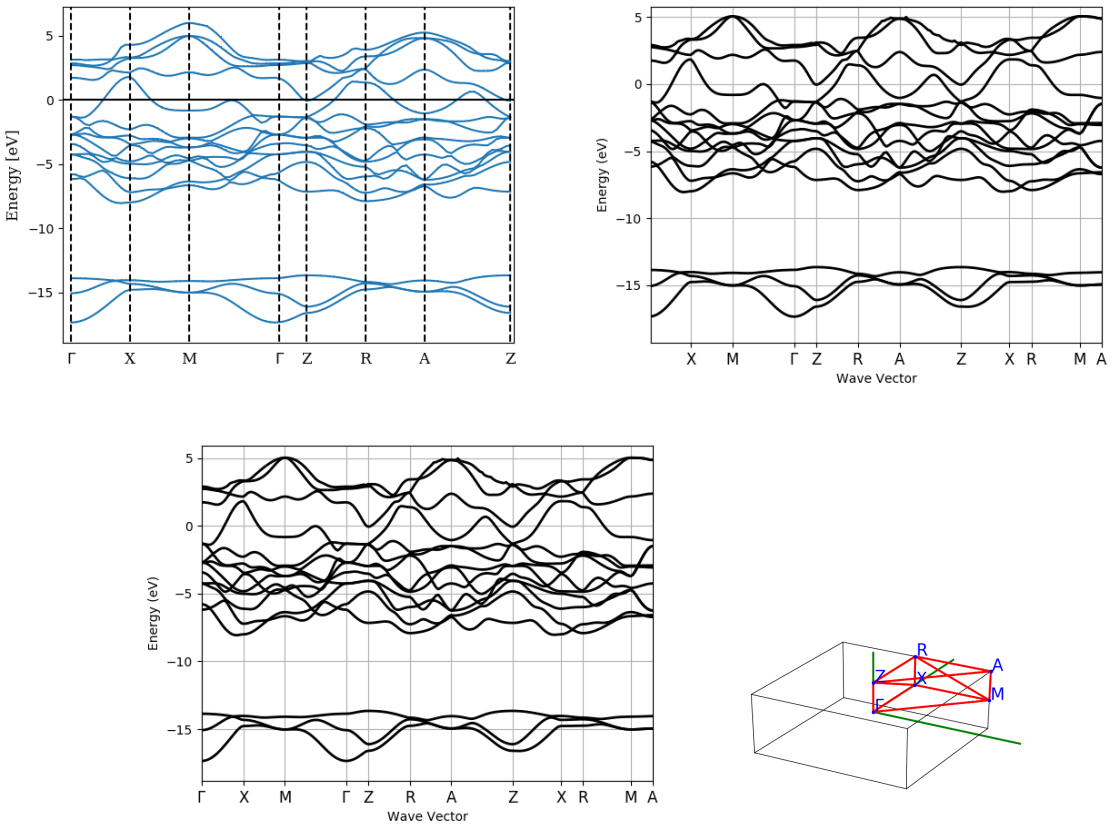

Figure 7.3.1: Calculated electron band structure for Ta_2N_3 with 8x8x8 **k**-points (top,right), on the bottom with a **k**-point grid of 12x12x12. And left, top in blue results of previous calculations with Quantum Espresso (**k**-points: 8x8x8).[10]

Differences between the electron band structures calculated with Abinit are negligible, while the bands structure calculated with Quantum Espresso does show slightly different behaviors and crossings. A electronic density of state is calculated for the **k**-point grid of 16x16x16 with a smearing of 0.01 Ha. Convergence is tested with a higher **k**-point set that did not influence the DOS meaningfully.

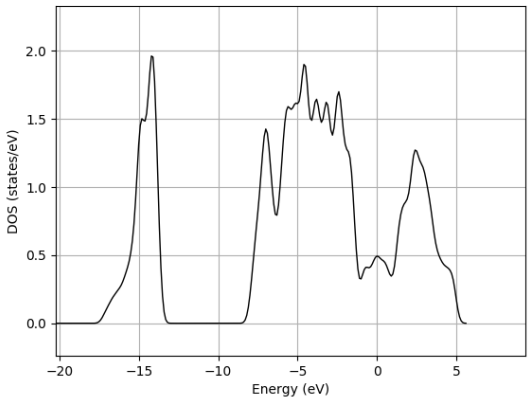

Figure 7.3.2: Density of states for the tetragonal Ta_2N_3 for a **k**-point grid of 16x16x16 with a smearing of 0.01 Ha, where the Fermi-level of 12.998 eV is set as zero point.

The density of states are in good agreement with previously calculated DOS from the literature.[9] Especially the important part around the Fermi-level that shows a small peak is of similar order and depicts a smaller DOS at Fermi level then for the orthorhombic Ta_2N_3.

7.4 Vibrational properties

The phonon frequencies are calculated and shown at the Γ-point.

Phonon energy[cm^{-1}]		
0.00	222.47	514.95
0.00	451.44	595.58
0.00	451.44	595.58
125.79	461.36	598.67
125.79	514.95	761.19

In order to calculate the phonon dispersion, a **q**-point grid of 4x4x4 was used with Abinit. A phonon dispersion was also calculated for 6x6x6 **q**-points and compared in order to prove convergence of the **q**-points:

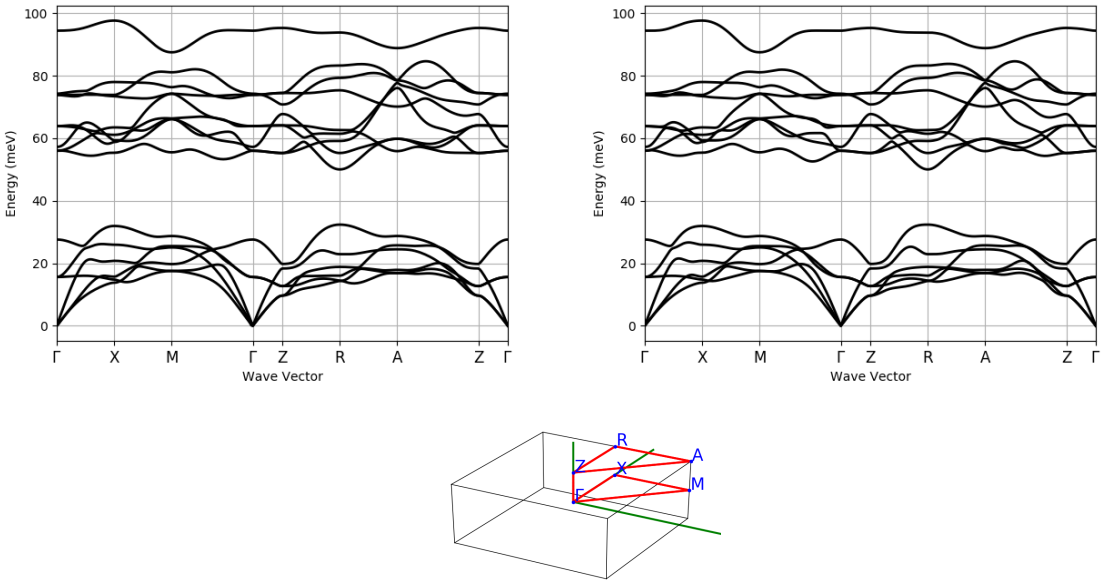

Figure 7.4.1: Phonon dispersion for tetragonal Ta_2N_3 for 4x4x4 **q**-points (left) and for 6x6x6 **q**-points.

One can see convergence because the phonon dispersion do not differ. The phonon DOS are also compared. A phonon density of states was calculated for a interpolated **k**-point grid of 36x36x36.

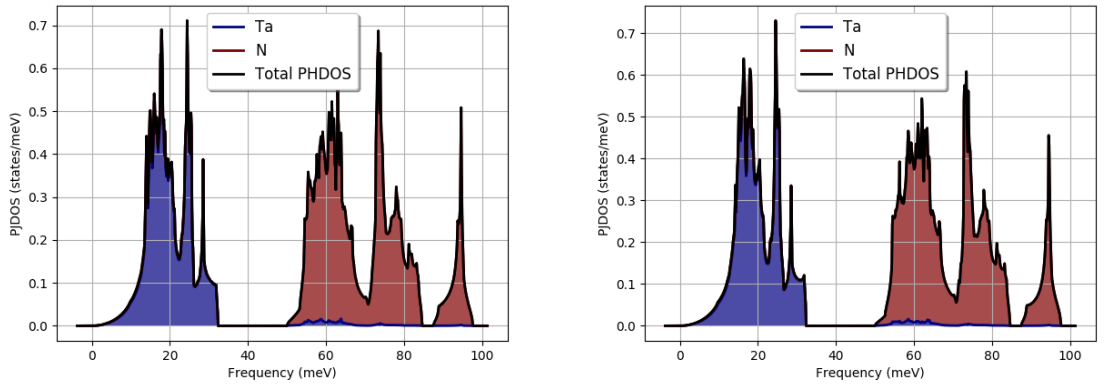

Figure 7.4.2: Phonon density of states for tetragonal Ta_2N_3 for 4x4x4 **q**-points and 6x6x6 **q**-points (right).

Furthermore, the calculation was also compared with last year's result that were produced with Quantum Espresso. They were not converged so a **q**-point grid of 2x2x2 was used with a **k**-point grid of 8x8x8.

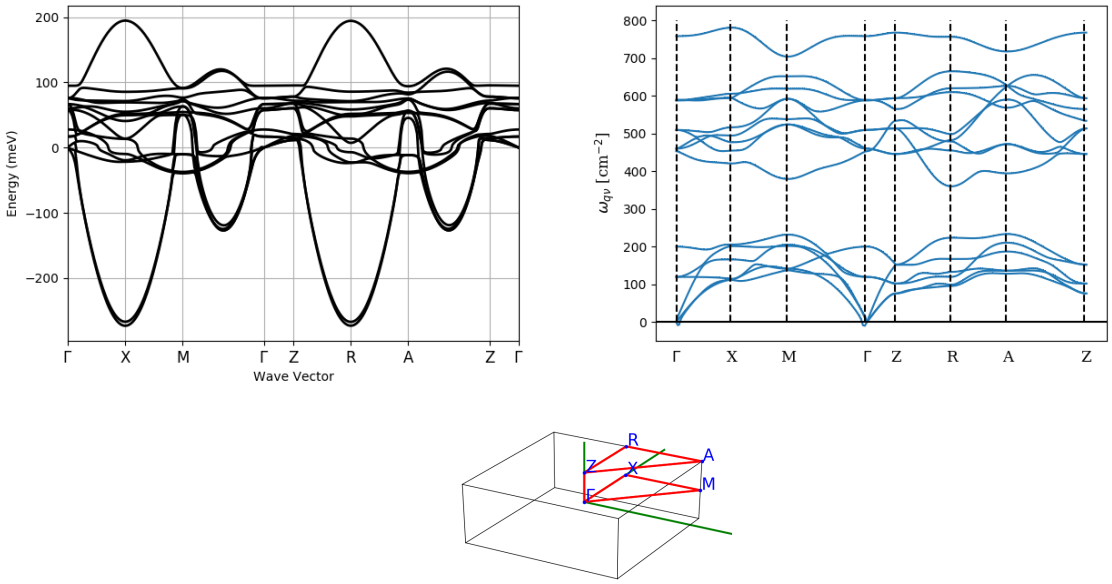

Figure 7.4.3: Phonon dispersion for tetragonal Ta_2N_3. Right in blue results of previous calculations with Quantum Espresso (**k**-points: 8x8x8, **q**-points 2x2x2) in comparison with new results produced in the frame of this work, also with **k**-points: 8x8x8, **q**-points 2x2x2.

One can see how the 2x2x2 **q**-points is not enough for the computation with Abinit, while the result through Quantum Espresso gives acceptable results that can be compared with the phonon dispersion in figure 7.4.1. Therefore, for the comparison between the superconductivity results, we use a **q**-point grid of 4x4x4 calculated with a **k** -point grid of 12x12x12

7.5 Superconductivity

One reason for recalculating the tetragonal Ta_2N_3 is to understand why the superconducting parameters, especially the logarithmic frequency are so low. Furthermore, these calculations attempt to predict more accurate superconducting parameter, for the calculations done with Quantum Espresso are rarely a broad estimation and not converged. We also do not attempt to prove perfect convergence but rather try to understand the numerical reasons for these big differences between the two outputs.

7.5.1 Convergence study

Nevertheless, a convergence study is conducted:

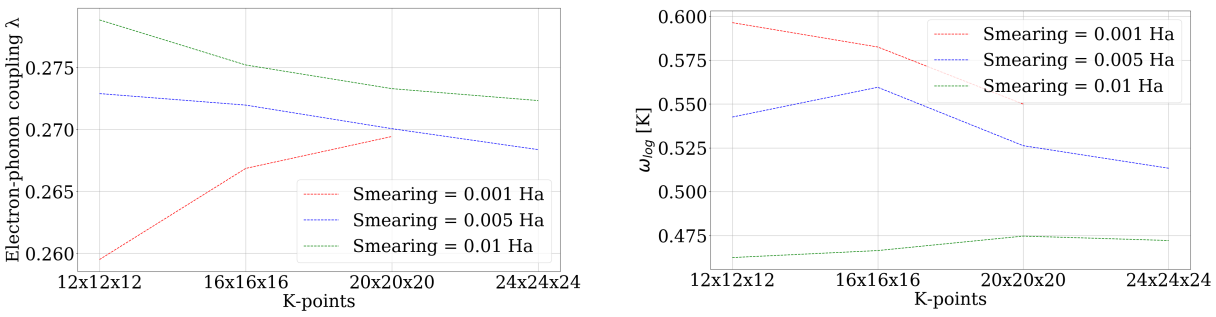

Figure 7.5.1: Convergence study with respect the the isotropic electron phonon coupling parameter λ and the logarithmic frequency $\omega_{\log}$.

We can see a very nice convergence towards the same value. It seems the tetragonal Ta_2N_3 is less sensitive with regards to the smearing then the other compounds. As seen are the two factor 0.005 Ha and 0.01 Ha quite well converged already for 12x12x12 **k**-points. The smearing 0.001 Ha shows more varying behavior.

7.5.2 Results and Comparison

First of all, the spectral densities are compared in figure 7.5.1:

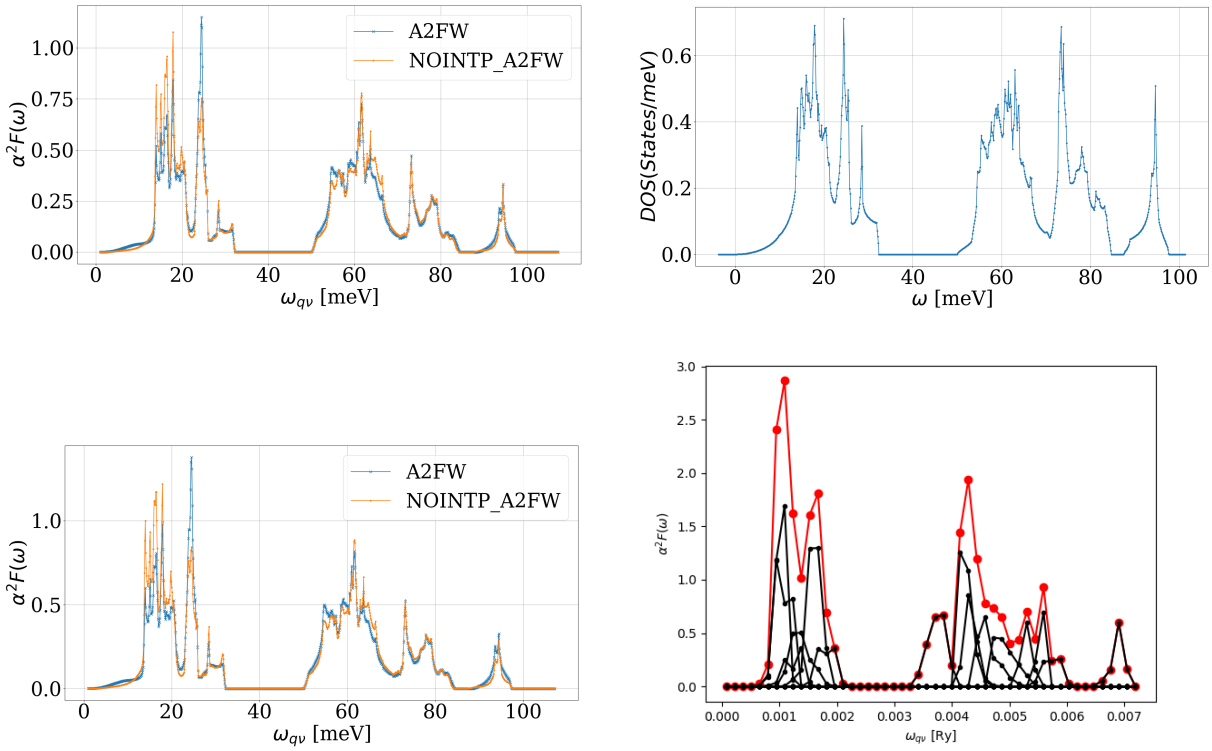

Figure 7.5.2: The predicted spectral function α^2F as a function of the frequency ω is calculated with Abinit with a **k**-point grid of 12x12x12, a **q**-point grid of 4x4x4 and a Gaussian smearing of 0.01 Ha (top,left). It is compared out phonon DOS calculation (top,right). On the bottom, left, the spectral density for a Gaussian smearing of 0.005 Ha is shown and compared with last years Quantum Espresso spectral density, whereas only a **k**-point grid of 8x8x8 and a **q**-point grid of 2x2x2 was used with a Gaussian smearing of 0.005 Ha. The red color denotes the total spectral density α^2F and the black lines show the mode resolved spectral density α^2F.

One can see how again the low frequency part of the spectral density function that is predicted with Abinit is too linear, even more linear then the broad estimation made by Quantum Espresso. The spectral density calculated by Quantum Espresso shows very little points in comparison with our result. Interestingly, the peaks themselves have a lot of linear character. The low frequency part seems highly parabolic. The logarithmic frequency is probably overestimated for the peaks have too much of a triangular form leading to higher spectral densities, although the peaks should have more of a form comparable for the phonon DOS. In the following the results are not only compared but again, it is tried to estimate the low frequency spectral function bit to find a good compromise leading to more exact results.

Table 7.5.1: Results for the isotropic parameters for different interpolation techniques and smearing techniques. The first column per smearing method called "Explicit interpolation" is interpolated but then the matrix elements are taken explicitly on the **k**-point grid and the second one is Fourier interpolated with respect to the DDB q-points (interpolated by ph_ngqpt). The different values for the logarithmic frequency $\omega_{\log}$ are recalculated results, while the isotropic λ is kept. The differently calculated $\omega_{\log}$ stand for when the spectral density is neglected until 13.6 meV (1. $\omega_{\log}$). The 2. $\omega_{\log}$ stands for when the first part until 13.6 meV is substituted by a phonon DOS-like curve. The following three $\omega_{\log}$-values stand for when the spectral density curve until 13.6 meV is substituted by a function $y = x^p$ with the power p= 1 (3.$\omega_{\log}$, linear), p = 3 (4. $\omega_{\log}$) and p = 100 (5. $\omega_{\log}$ upper limit).

	Quantum Espresso output		Abinit Output			
Gaussian smearing	0.005 Ha	0.01 Ha	0.005 Ha		0.01 Ha	
			Explicit	Fourier	Explicit	Fourier
λ	4.6127	3.093	0.5857	0.5425	0.4897	0.4624
$\omega_{\log}$ [K]	317.734	294.920	0.2560	0.2729	0.2670	0.2788
1. $\omega_{\log}$ [K]	/	/	14.9086	6.7474	0.2796	0.1230
2. $\omega_{\log}$ [K]	/	/	4.6940	1.9377	0.0817	0.0334
3. $\omega_{\log}$ [K]	/	/	0.5851	0.2047	0.0039	0.0013
4. $\omega_{\log}$ [K]	/	/	3.9325	1.6007	0.0473	0.0187
5. $\omega_{\log}$ [K]	/	/	8.2963	3.5836	0.1254	0.0526
T_c [K]	64.856	52.065	0.0022-0.3239			
Debye temperature [K]	/	/	343.64-588.03			
Debye T_c [K]	/	/	2.4287-10.5726			

One can see how the logarithmic frequency is 100 times smaller when calculated through Abinit then the result from Quantum Espresso. But also the EPC is 10 times smaller leading to completely different predictions. It is important to mention that the results acquired through Abinit are much more dependable for they are well converged. But looking the result, the risk of underestimation of the EPC is possible for the Abinit calculations. When trying to estimate the logarithmic frequency better through changing the low frequency part, one gets more realistic results. This is shown in detail in the following figure:

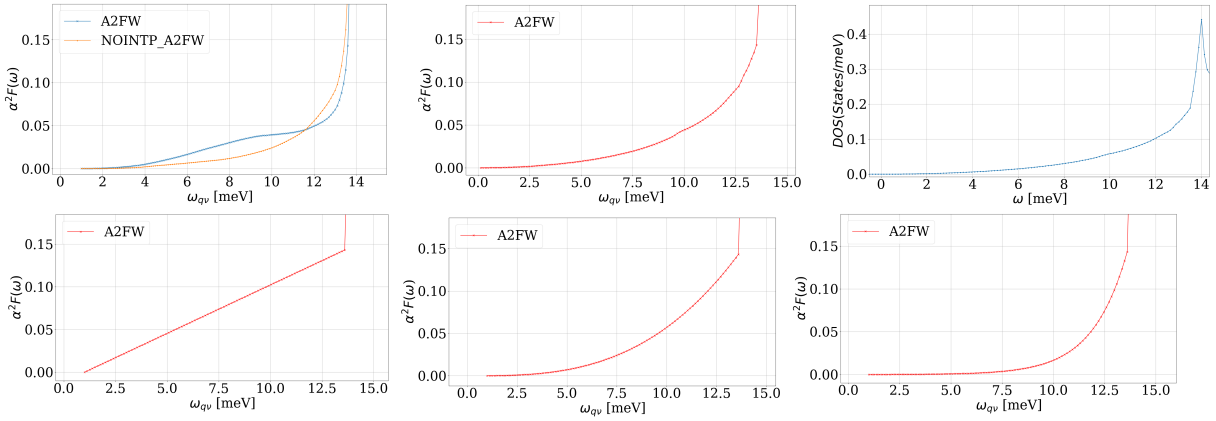

Figure 7.5.3: The spectral function α^2F as a function of the frequency ω is shown here for tetrahedron smearing with a smearing of 0.01 Ha. The left picture shows the original low frequency part of the spectral function. In the middle (red) the phonon DOS low frequency curve has been fitted to the spectral function until 13.6 meV in comparison with the phonon density of states beginning (right in blue). The bottom three spectral density estimations stand for when the spectral density curve until 13.6 meV is substituted by a function $y = x^p$ with the power p=1 (left, bottom 3.$\omega_{\log}$, linear), p=3 (middle, bottom 4. $\omega_{\log}$) and p=100 (right, bottom 5. $\omega_{\log}$ upper limit).

Again, the neglected part gave for previous calculations a more realistic $\omega_{\log}$, therefore it is taken into account although it is not physical. This leads to a very rough estimate of the $\omega_{\log}$. The second value is physically motivated, but still too low, implying that there is more to the numerical error then just the low frequency part. A function is applied to see how the logarithmic frequency varies showing how sensitive it is to the low frequency part change. The linear results are not taken into account for they are very far away from reality. Interestingly, these estimations give even smaller values for the logarithmic frequency $\omega_{\log}$ when taking a 0.01 Ha Gaussian smearing into account. The same framework was used like for the orthorhombic Ta_2N_3, but the result differ drastically from what one calculates with Quantum Espresso. But the Quantum Espresso results are a rough estimate and one can see on the spectral density function α^2F, that it is not accurate at all. Nevertheless, this big difference has to be investigated further. We see here on one side an overestimation and on the other side an underestimation. For a compound like the Ta_2N_3, the logarithmic frequency should be much higher then what is found. So again, it is proposed to use the Debye temperature instead of the logarithmic frequency, with the thought kept in mind that it usually also overestimates the critical temperature. With it one can predict superconductivity at very low critical temperature of about $\approx$ 2 K. But this prediction is not strong enough, so there is still a possibility that the compound is not superconductive at all.

Table 7.5.2: Superconducting parameters found from the electron-phonon calculation. The Debye temperature is an output from the phonon density of states calculation and the two values stem from the calculation from partial sums and the second value stems from the phDOS directly.

Isotropic λ	0.46-0.59
$\omega_{\log}$	0.26-14.91 K
Empirical parameter μ^*	0.1
McMillan critical temperature	0.00-0.32 K
Debye-temperature from phDOS-partial sums	343.64-588.03 K
Critical temperature calculated from equation (3.79)	2.43-10.57 K

8 Orthorhombic Nb_2N_3

Due to the successful synthesis of the η-Ta_2N_3, more attention was drawn towards this group of metal nitrides. The possibility to use it at ambient conditions and their display of exceptional properties like high hardness and superconductivity, these materials are interesting for applications are hard and fracture-resistant materials etc.[3] Jiang *et al.*[3] investigated with the help of first principle methods the class of metal nitrides with the stoichiometry M_2N_3 whereas M=Nb, V. They identified their structure with the help of random structure search of the η-Nb_2N_3 which will be investigated in the following regarding its superconductivity. Therefore, the electronic and vibrational parameters are firstly deduced. It is a promising candidate due to its lower atomic mass atom Niobium which was assumed to lead to a higher critical temperature then for the η-Ta_2N_3.

8.1 Convergence study

Like for Ta_2N_3, convergence tests regarding the k-point grid, the smearing and the energy cut-off were conducted:

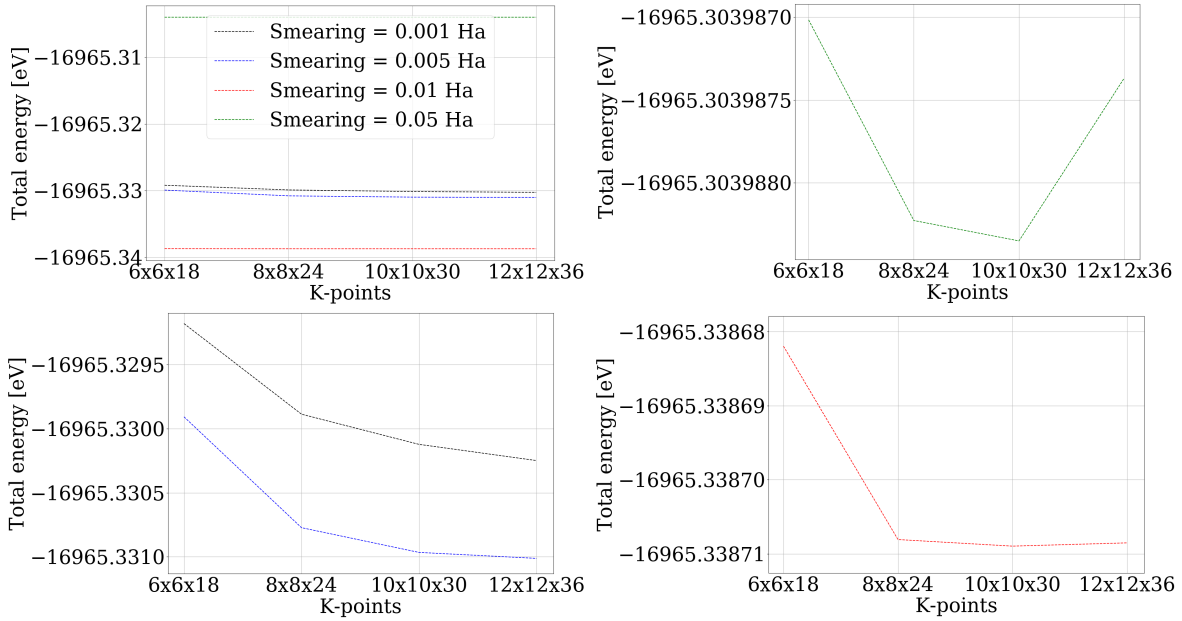

Figure 8.1.1: K-points convergence for different smearing values. The smearing factors of 0.001 Ha (black), 0.005 Ha (blue), 0.01 Ha (red) and 0.05 Ha (green) are explored for Cold smearing.

For the smearing factor 0.001,0.005 and 0.01 Ha, one can say that the higher the smearing is, the faster a convergence is reached. The differences in the total energy are of the order of 10^{-4} eV. Therefore, a k-point grid of 8x8x24 is used with 0.01 Ha smearing for further calculations. The smearing of 0.05 Ha leads to a different, divergent behavior. It seems this structure is also quite sensitive to the smearing for the convergence values are differing per smearing factor/method.

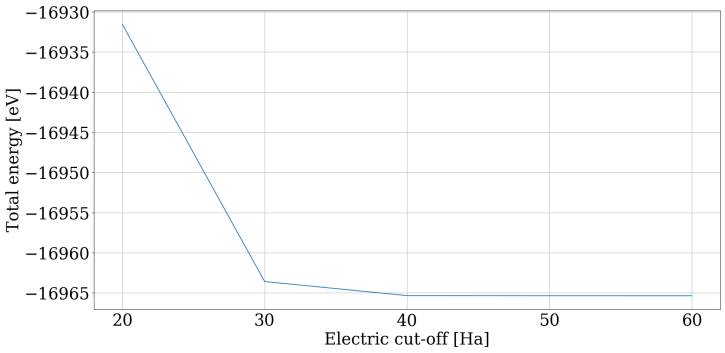

Figure 8.1.2: Energy cut-off convergence test.

An energy cut-off of 40 Ha was chosen for the value converged an error of $\pm 5 \cdot 10^{-3}$.

8.2 Optimisation

A optimisation was conducted of the atomic coordinates and the unit cell parameter, where the optimised values for Ta_2N_3 were used.

Table 8.2.1: Optimized atomic coordinates and previous theoretical results in brackets by Jiang *et al.*[3]

Atom	x	y	z
Nb1	0.313 (0.313)	-0.022 (-0.022)	0.25 (0.25)
Nb2	0.504 (0.504)	0.305 (0.305)	0.25 (0.25)
N1	0.874 (0.874)	0.046 (0.046)	0.25 (0.25)
N2	0.548 (0.548)	0.879 (0.879)	0.25 (0.25)
N3	0.202 (0.202)	0.221 (0.221)	0.25 (0.25)

The literature atomic coordinates resemble the found optimized values.
The new cell parameter are the following:

- a = 8.14 Å
- b = 8.25 Å
- c = 3.00 Å

The cell parameter are in good agreement with previous theoretical result by Jiang *et al.*[3] (a = 8.20 Å, b = 8.31 Å, c = 3.02 Å) and by Zhang *et al.*[54] (a = 8.14 Å, b = 8.24 Å, and c = 3.00 Å at). This leads to a volume of the unit cell of 201.47 $Å^3$.

8.3 Electronic structure

The electronic structure and density of states was calculated for 8x8x24 and smearing of 0.01 Ha. It was compared to the calculation with smearing 0.05 Ha and like for the Ta_2N_3 one could could only find a difference in Fermi-level.

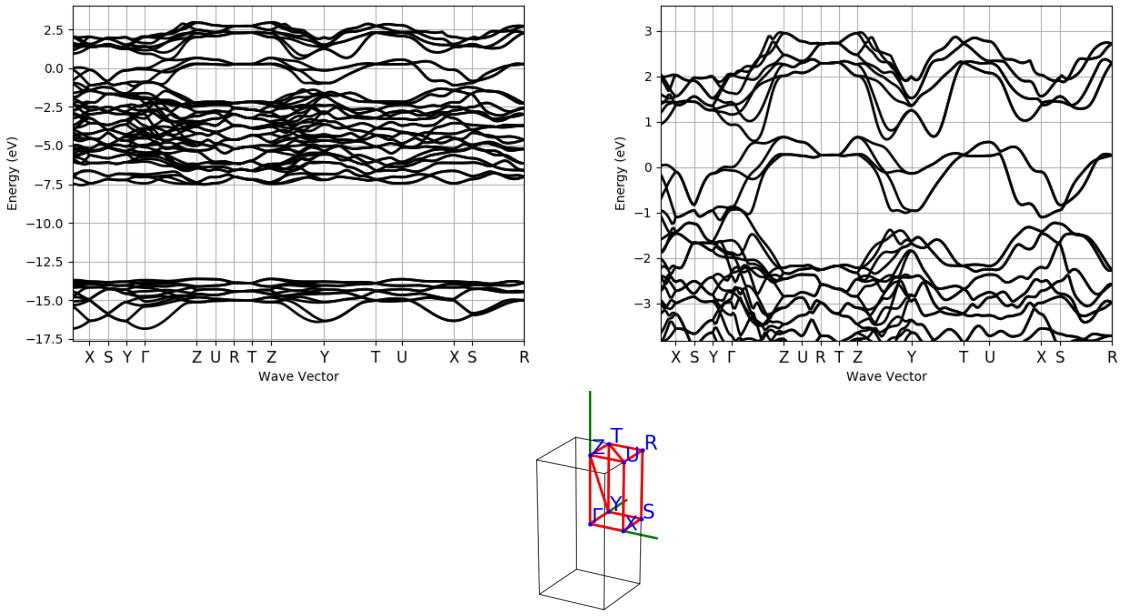

Figure 8.3.1: Electron band structure for Nb_2N_3 with a Fermi-level of 14.049 eV set to the zero point.

The DOS are an important parameter to predict superconductivity. Specifically, the DOS at the Fermi-level is importnat which can be found in the DOS of Nb_2N_3.

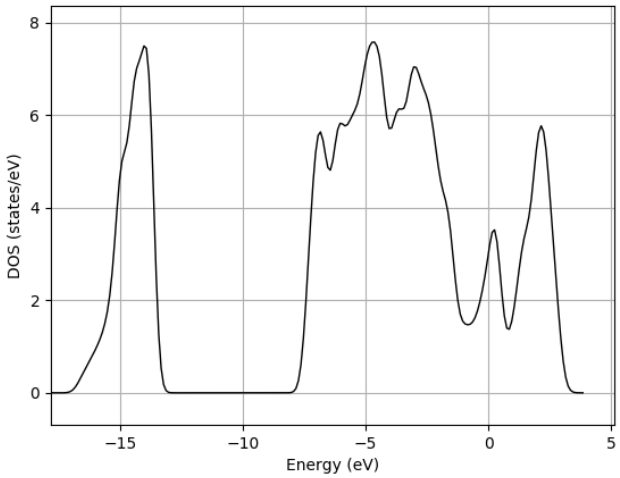

Figure 8.3.2: Density of states for Nb_2N_3 with a Fermi-level of 14.049 eV set to the zero point.

8.4 Vibrational properties

The Phononfrequencies at Γ-point were calculated and listed in the following. A **k**-point grid of 8x8x24 was used with a smearing factor of 0.01 Ha.

Table 8.4.1: 22 IR-active Phononmodes at Γ-point.

Phonon energy [cm^{-1}]	Activity	D_{2h}	Phonon energy[cm^{-1}]	Activity	D_{2h}
106.2	y	B_{1u}	483.1	y	B_{1u}
168.6	x	B_{3u}	514.8	y	B_{1u}
178.6	z	B_{1u}	523.9	x	B_{3u}
237.0	y	B_{1u}	532.9	z	B_{1u}
255.3	x	B_{3u}	553.2	x	B_{3u}
273.1	y	B_{1u}	593.2	z	B_{1u}
284.4	x	B_{3u}	594.7	y	B_{1u}
352.3	y	B_{1u}	617.7	x	B_{3u}
372.8	y	B_{1u}	629.8	y	B_{1u}
387.3	x	B_{3u}	648.5	y	B_{1u}
470.1	x	B_{3u}	743.3	x	B_3u

Table 8.4.2: Silent modes at Γ-point.

Phonon energy [cm^{-1}]	Activity	D_{2h}	Phonon energy[cm^{-1}]	Activity	D_{2h}
0.00	/	/	170.6	/	A_u
0.00	/	/	429.5	/	A_u
0.00	/	/	506.3	/	A_u
150.3	/	A_u	577.8	/	A_u
155.8	/	A_u			

Table 8.4.3: Raman active modes at Γ-point.

Phonon energy [cm^{-1}]	Activity	D_{2h}	Phonon energy[cm^{-1}]	Activity	D_{2h}
102.6	xy, J_z	B_{1g}	456.3	xy, J_z	B_{1g}
133.6	xz, J_y	B_{2g}	462.1	x^2,y^2,z^2	A_g
165.1	xz, J_y	B_{2g}	483.4	xz,J_y	B_{2g}
169.7	x^2,y^2,z^2	A_g	507.7	xy,J_z	B_{1g}
188.9	yz,J_x	B_3g	535.1	yz, J_x	B_{3g}
207.1	x^2,y^2,z^2	A_g	536.6	xz,J_y	B_{2g}
211.5	x^2,y^2,z^2	A_g	564.0	x^2, y^2, z^2	A_g
235.7	xy,J_z	B_{1g}	579.6	xy, J_z	B_{1g}
252.8	xy,J_z	B_{1g}	596.0	x^2,y^2,z^2	A_g
292.1	xy,J_z	B_{1g}	604.1	xy,J_z	B_{1g}
314.3	x^2,y^2,z^2	A_g	634.9	xy, J_z	B_{1g}
373.0	xz, J_y	B_{2g}	638.1	x^2, y^2, z^2	A_g
376.5	x^2,y^2,z^2	A_g	683.3	xy, J_z	B_{1g}
416.9	yz, J_x	B_{3g}	701.5	x^2, y^2, z^2	A_g
446.0	yz, J_x	B_{3g}			

After producing the phonondispersion with the same experimental set-up, a soft mode at Z-point could be seen. Therefore, the phonondispersion with a smearing factor of 0.05 Ha was also produced and both results were compared.

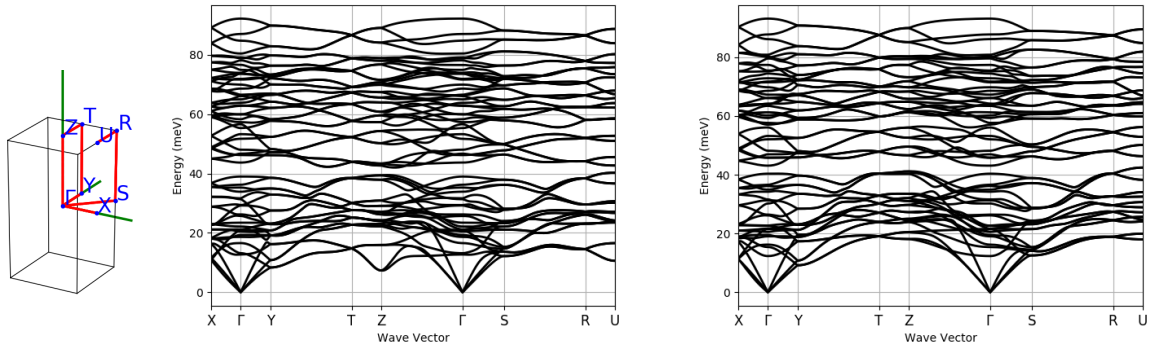

Figure 8.4.1: Phonondispersion for Nb_2N_3 at ambient pressure for k-point grid 8x8x24 with smearing 0.01 Ha and k-point grid 6x6x18 with a smearing of 0.05 Ha

One can see a soft mode appearing at the Z-point, that disappears for higher smearing like for the Ta_2N_3. This also impacts the phonon density of states.

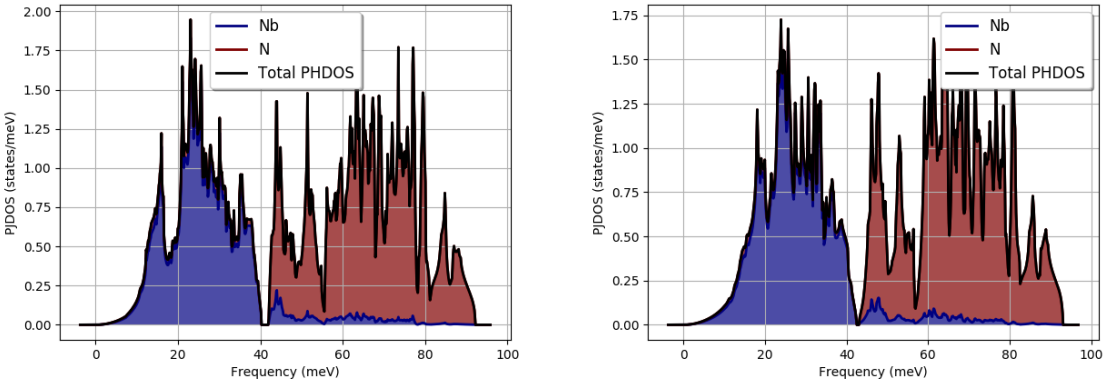

Figure 8.4.2: Density of states for Nb_2N_3 at ambient pressure for k-point grid 8x8x24 with smearing 0.01 Ha and k-point grid 6x6x18 with a smearing of 0.05 Ha

8.5 Superconductivity

8.5.1 Convergence study

Like in the previous chapter, a convergence study is conducted in order to produce realistic superconducting parameter. In the following, the dataset with 0.05 Ha is taken into account for the convergence study and it is assumed to produce the same results for 0.01 Ha.

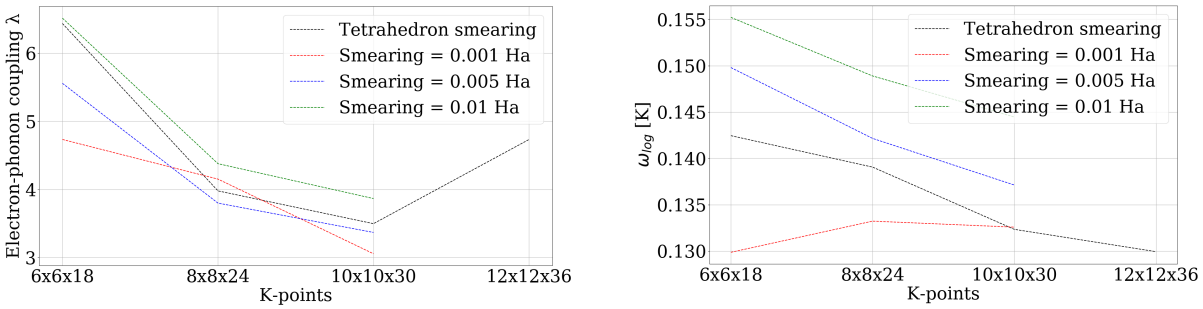

Figure 8.5.1: Convergence study for different set-up's with respect to the calculated EPC λ (left) and the logarithmic frequency $\omega_{\log}$ (right). The **k**-point grid and the smearing factor and method are varied to choose the most accurate set-up. If there are smearing factors given, then the smearing method is the Gaussian smearing. One does not need a smearing factor for the tetrahedron smearing. The Fourier interpolated results are featured in this convergence study.

One can see how the values converge slowly for the EPC. The only value for a **k**-point grid of 12x12x36 that is accessible shows divergent behavior. Also for the Gaussian smearing factor 0.001 Ha, the behavior is less convergent like for the other smearing values. When looking at the right figure 7.5.1, one can see for the Gaussian smearing method, how the values tend to converge towards a around 0.135 K. The tetrahedron smearing shows a different behavior in which it tends to go towards lower logarithmic frequencies. It is still possible that it would rise again and oscillate around the same value. For the following, the **k**-point grid of 10x10x30 is used for further calculations, while a smearing factor of 0.005 Ha is used and compared to the tetrahedron smearing.

8.5.2 Further investigation and Results

Data set smearing 0.05 Ha

After isotropic evaluation of the parameters from the electron-phonon coupling, the following indicators were found regarding the superconductivity. A Coulomb screening of 0.12 was chosen for the calculation of the critical temperature via Abinit. One can see again how the $\omega_{\log}$ is unrealistically small again. The first column per smearing method called "Explicit interpolation" is interpolated but then the matrix elements are taken explicitly on the **k**-point grid (NOINTP_A2FW) and the second one is Fourier interpolated with respect to the DDB q-points (interpolated by ph_ngqpt (A2FW)).

Table 8.5.1: Results for the isotropic parameters for different interpolation techniques and smearing techniques. The numbered $\omega_{\log}$ are recalculated results, while the isotropic λ is kept. The differently calculated $\omega_{\log}$ stand for when the spectral density is neglected until 9.5 meV (1), 10.9 meV (2) and 12 meV (3). The forth $\omega_{\log}$ stands for when the first part until 12 meV is substituted by a phonon DOS-like curve. The values 5-7. $\omega_{\log}$ stand for substitution of the low frequency bit until 12 meV with a function $x = y^p$ with the power of $p = 1$ (5.$\omega_{\log}$, strictly linear, lower limit), $p = 3$ (6.$\omega_{\log}$, cubic) and $p = 100$ (6.$\omega_{\log}$,, upper limit).

	Tetrahedron smearing		Gaussian smearing 0.005 Ha	
	Explicit Interpolation	Fourier interpolation	Explicit Interpolation	Fourier interpolation
T_c [K]	$2.74 \cdot 10^{-2}$	$2.46 \cdot 10^{-2}$	$2.84 \cdot 10^{-2}$	$2.51 \cdot 10^{-2}$
Isotropic λ	3.3406	3.4957	3.2116	3.3666
$\omega_{\log}$ [K]	0.1502	0.1323	0.1581	0.1371
1. $\omega_{\log}$ [K]	1.0311	1.8061	0.8915	1.6052
2. $\omega_{\log}$ [K]	1.6739	2.8696	1.4097	2.4854
3. $\omega_{\log}$ [K]	3.5352	5.0906	2.3874	4.1082
4. $\omega_{\log}$ [K]	0.2642	0.4915	0.1968	0.3799
5. $\omega_{\log}$ [K]	0.0076	0.0165	0.0082	0.0183
6. $\omega_{\log}$ [K]	0.4098	0.7478	0.3678	0.6898
7. $\omega_{\log}$ [K]	1.7036	2.9182	1.4313	2.9182
Positive moments of $\alpha^2F(\omega)$				
λ (ω^2)	$3.64 \cdot 10^{-6}$	$3.64 \cdot 10^{-6}$	$3.58 \cdot 10^{-6}$	$3.58 \cdot 10^{-6}$
λ (ω^3)	$6.58 \cdot 10^{-9}$	$6.57 \cdot 10^{-9}$	$6.49 \cdot 10^{-9}$	$6.48 \cdot 10^{-9}$
λ (ω^4)	$1.47 \cdot 10^{-11}$	$1.47 \cdot 10^{-11}$	$1.448395 \cdot 10^{-11}$	$1.46 \cdot 10^{-11}$
λ (ω^5)	$3.64 \cdot 10^{-14}$	$3.69 \cdot 10^{-14}$	$3.60 \cdot 10^{-14}$	$3.65 \cdot 10^{-14}$

Again, one can see how the $\omega_{\log}$ is too small. Therefore, a similar approach is again used to make a better approximation of the low frequency bit of the spectral function. Firstly, the low frequency parts are neglected again, which is as explained not very physical. But this leads to higher, more realistic logarithmic frequencies $\omega_{\log}$. Secondly the phonon DOS is fitted. This is the most physically useful result, but the values become up to 5 times bigger not reaching very realistic results showing how the assumed wrong interpolation does probably affect more then just the low frequency bit. Furthermore, obviously the phonon DOS is not electron-phonon coupling weighted. Lastly it is tried to fit a new low frequency bit, to explore the sensitivity of the logarithmic frequency $\omega_{\log}$. The logarithmic frequency does not rise as much as for the Ta_2N_3-analogue. The linear function does lead to much smaller values, while the extremely steep applied function of $y = x^{100}$ leads to values up to around 3 K, which is more probable. The values are much more stable between the different experimental set-up's and sensitivity to smearing is also lower. In the next figure one can see the spectral function and how the low frequency part is linear, while the phonon DOS shows parabolic behavior.

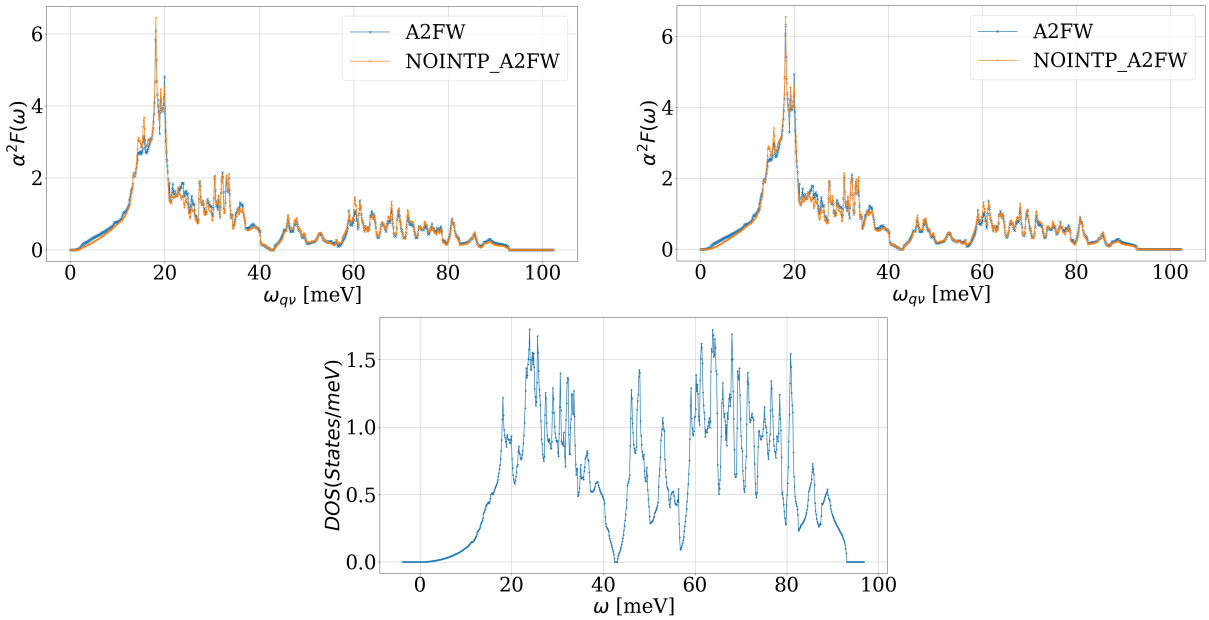

Figure 8.5.2: The spectral function α^2F as a function of the frequency ω is shown here for tetrahedron smearing (top,left) and Gaussian smearing with the factor 0.005 (top,right) in comparison with the phonon density of states (bottom).A2FW stands for the additionally Fourier interpolated results, while NOINTP_A2FW stands for the explicitly interpolated results.

Again, we try to fit a new kind of function in order to investigate the change of logarithmic frequency. Interestingly, it does not change as massively as for the previous Ta_2N_3-analogue. This leads to the conclusion that the numerical issue might not only be one of the low frequency components. Further investigations to answer that question are needed.

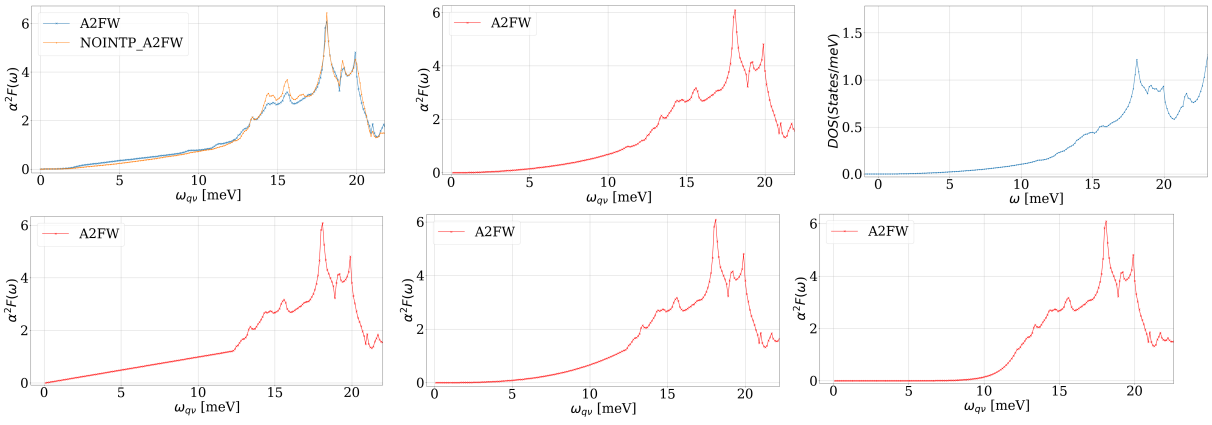

Figure 8.5.3: The spectral function α^2F as a function of the frequency ω is shown here for tetrahedron smearing. The top, left picture shows the original low frequency part of the spectral function giving $\omega_{\log}$. In the top, middle (red) the phonon DOS low frequency curve has been fitted to the spectral function until 12 meV (4. $\omega_{\log}$) in comparison with the phonon density of states beginning (top,right in blue). On the bottom we see the case for which a function $y = x^p$was fitted (power p= 1 (5. $\omega_{\log}$), p=3 (6. $\omega_{\log}$), p=100 (7. $\omega_{\log}$)).

The superconducting parameters found for taking into account a smearing for the input phonon files of 0.05 Ha are shown in table 7.5.2. The Debye temperature is an output from the phonon density of states calculation and the two values stem from the calculation from partial sums and the second value stems from the phonon DOS directly.

Table 8.5.2: superconducting parameters found for taking into account a smearing for the input phonon files of 0.05 Ha. The Debye temperature is an output from the phonon density of states calculation and the two values stem from the calculation from partial sums and the second value stems from the phDOS directly.

Isotropic λ	3.21-3.50
$\omega_{\log}$	0.13-5.09 K
Empirical parameter μ^*	0.1
McMillan critical temperature	0.02-0.97 K
Debye-temperature from phDOS-partial sums	218.12-263.36 K
Critical temperature calculated from equation (3.79)	33.43 - 41.75 K

Data set smearing 0.01 Ha

The behavior is investigated for another smearing factor used for generation of the input files to see how that will impact the superconductive behavior. For the orthorhombic Ta_2N_3 the results with this smearing impacted the final results positively by letting them be closer to experimental values. We assume same convergence behavior like for the data set of 0.05 Ha smearing.

Table 8.5.3: Results for the isotropic parameters for different interpolation techniques and smearing techniques. The numbered $\omega_{\log}$ are recalculated results, while the isotropic λ is kept. The differently calculated $\omega_{\log}$ stand for when the spectral density is neglected until 9.5 meV (1), 10.9 meV (2) and 12 meV (3). The forth $\omega_{\log}$ stands for when the first part until 12 meV is substituted by a phonon DOS-like curve.

	Tetrahedron smearing		Gaussian smearing 0.005 Ha	
	Explicit Interpolation	Fourier interpolation	Explicit Interpolation	Fourier interpolation
T_c [K]	$2.300408 \cdot 10^{-2}$	$2.18 \cdot 10^{-2}$	$2.56 \cdot 10^{-2}$	$2.34 \cdot 10^{-2}$
Isotropic λ	5.6941	5.8213	8.2774	8.5293
$\omega_{\log}$ [K]	0.1067	0.1007	0.1103	0.1006
1. $\omega_{\log}$ [K]	0.7175	0.9531	0.5004	0.7423
2. $\omega_{\log}$ [K]	1.5717	2.0523	1.0944	1.5864
3. $\omega_{\log}$ [K]	5.1950	6.6086	3.8080	5.3204
4. $\omega_{\log}$ [K]	0.6717	0.8935	0.0541	0.0857
Positive moments of $\alpha^2F(\omega)$				
λ (ω^2)	$4.33 \cdot 10^{-6}$	$4.33 \cdot 10^{-6}$	$5.88 \cdot 10^{-6}$	$5.88 \cdot 10^{-6}$
λ (ω^3)	$7.19 \cdot 10^{-9}$	$7.23 \cdot 10^{-9}$	$9.26 \cdot 10^{-9}$	$9.33 \cdot 10^{-9}$
λ (ω^4)	$1.54 \cdot 10^{-11}$	$1.57 \cdot 10^{-11}$	$1.93 \cdot 10^{-11}$	$1.96 \cdot 10^{-11}$
λ (ω^5)	$3.74 \cdot 10^{-14}$	$3.84 \cdot 10^{-14}$	$4.61 \cdot 10^{-14}$	$4.74 \cdot 10^{-14}$

We see much higher values for the EPC λ indicating a strong electron-phonon coupling. Furthermore, the electron phonon coupling parameter λ varies strongly between the tetrahedron and Gaussian smearing ($\approx .5.7 \longleftarrow \approx 8.5$ indicating that the convergence might have a different form then for the 0.01 Ha smearing data set. The logarithmic frequency is again attempted to be estimated, while here the same low frequency parts are either neglected or the phonon DOS is fitted onto the function, which is the most physical estimate. Neglecting parts of the low frequency components it justified just so that the logarithmic frequency takes on more realistic values comparable to the other calculations made in this work.

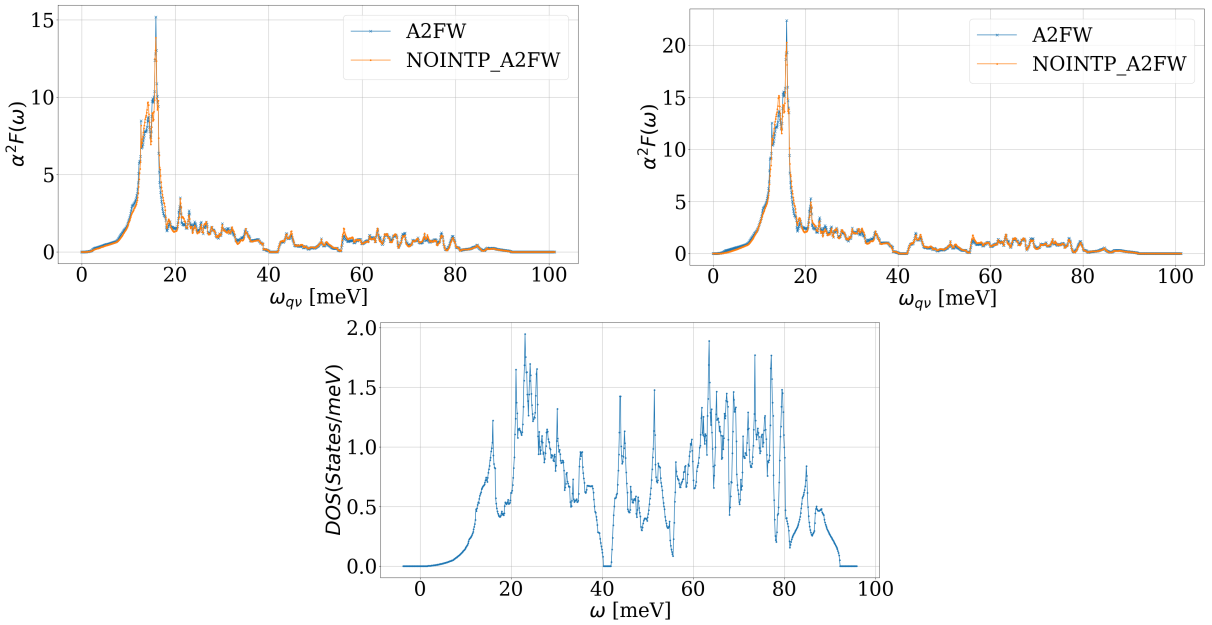

Figure 8.5.4: The spectral function α^2F as a function of the frequency ω is shown here for tetrahedron smearing (top,left) and Gaussian smearing with the factor 0.005 (top,right) in comparison with the phonon density of states (bottom).A2FW stands for the additionally Fourier interpolated results, while NOINTP_A2FW stands for the explicitly interpolated results.

The Eliashberg function α^2F looks unusual. The low frequency peak is is reaching very high values. Main contributor to this peak is the Niobium, which can be seen in figure 7.4.2. In the next figure, the low frequency bit is shown and its estimates:

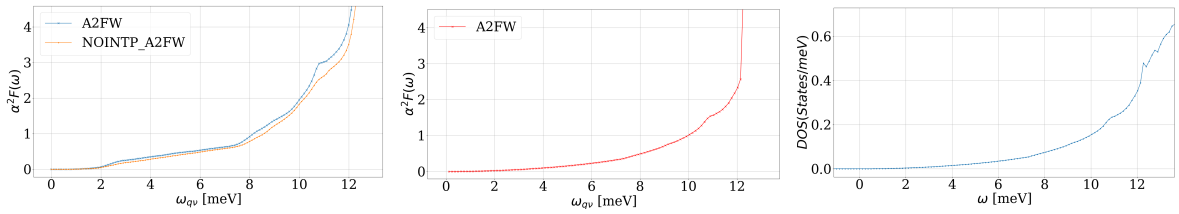

Figure 8.5.5: The spectral function α^2F as a function of the frequency ω is shown here for tetrahedron smearing. The left picture shows the original low frequency part of the spectral function giving $\omega_{\log}$. In the middle (red) the phonon DOS low frequency curve has been fitted to the spectral function until 12 meV (4. $\omega_{\log}$) in comparison with the phonon density of states beginning (right in blue).

The results of this data set are summarized in table 7.5.4 and the critical temperature is recalculated. One can see the McMillan critical temperature being very low, which is due to the very low logarithmic frequency $\omega_{\log}$ that is just roughly approximated and is certainly still too low. The critical temperature calculated through equation (3.79) is much closer to what can be expected for a value with such a high EPC and low atomic mass atoms like Niobium and nitrogen.

Table 8.5.4: Superconducting parameters found for taking into account a smearing for the input phonon files of 0.01 Ha. The Debye temperature is an output from the phonon density of states calculation and the two values stem from the calculation from partial sums and the second value stems from the phDOS directly.

Isotropic λ	5.69-8.53
$\omega_{\log}$	0.05-6.61 K
Empirical parameter μ^*	0.1
McMillan critical temperature	0.011-1.57 K
Debye-temperature from phDOS-partial sums	215.16-262.17 K
Critical temperature calculated from equation (3.79)	39.30-51.57 K

Final result

Finally, all results from the two data set's are presented together in the following. They are compared to the results for the η-Ta_2N_3.

Table 8.5.5: superconducting parameters for the η-Nb_2N_3 in comparison with the η-Ta_2N_3.

	η-Ta_2N_3 at ambient pressure	η-Nb_2N_3
Isotropic λ	0.77-1.16	3.21-8.53
$\omega_{\log}$	0.04-36.54 K	0.05-6.61 K
Empirical parameter μ^*	0.1	0.1
McMillan critical temperature	0.00-3.144 K	0.01-1.57 K
Debye-temperature from phDOS/partial sums	82.06-193.75 K	215.16-263.36 K
Critical temperature calculated from equation (3.79)	3.74-10.65 K	32.97-51.81 K

The result of the EPC is surprisingly high. It is very probable that this structure does show a very high EPC. The logarithmic frequency is a vague approximations, while the upper limit is achieved through neglecting parts of the Eliashberg function which can't be justified physically. Therefore, this leads to a very low overall critical temperature. Again, the critical temperature calculated through calculation (3.79) is much more realistic, although probably overestimated.

9 Orthorhombic V_2N_3

In parallel with the structural investigations of the η-Nb_2N_3, Jiang *et al.* investigated the η-V_2N_3. It was shown how there are other structures then the orthorhombic one that are energetically more favorable, whereas the most energetically stable is the trigonal V_2N_3. Nevertheless, in the following sections, the η-V_2N_3 is further investigated regarding its vibational and electronic parameters.

9.1 Convergence study

Like previously, convergence tests were conducted to get the optimal values for the k-point grid, the smearing and the energy cut-off.

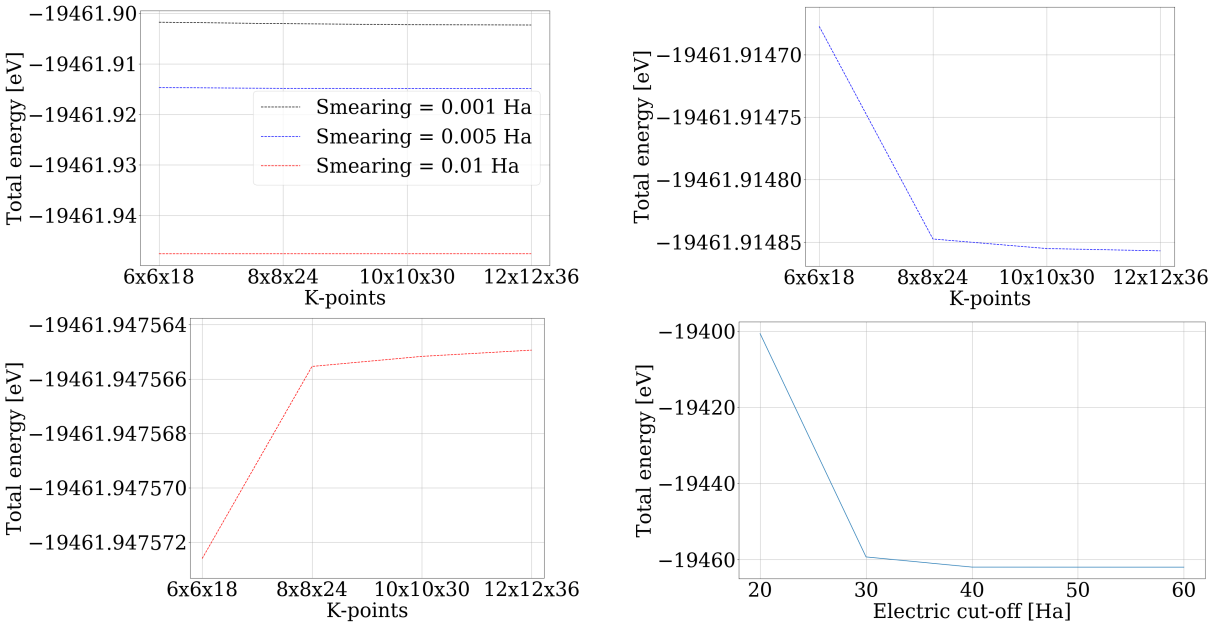

Figure 9.1.1: **K**-points and Smearing convergence study seen in the top left. One can see on the top, right the **k**-points convergence for Smearing=0.005 and bottom, left the **k**-points convergence for Smearing=0.05. On the bottom right, one can see the energy cut-off convergence.

Following calculations were conducted with a grid of 8x8x24 k-points, 0.01 Ha smearing and an energy cut-off of 40 Ha. The energy cut-off introduces an error of $\pm\, 5 \cdot 10^{-4}$ eV.

9.2 Optimisation

The atomic parameter and the atomic coordinates of the η-Nb_2N_3 were used and optimized to give the structural information for the η-V_2N_3.

Table 9.2.1: Optimized atomic coordinates.

Atom	x	y	z
V1	3.123	-2.506	0.25
V2	4.994	3.030	0.25
N1	0.872	0.044	0.25
N2	0.549	0.881	0.25
N3	0.195	0.220	0.25

The new cell parameter are the following:

- a = 7.69 Å
- b = 7.74 Å
- c = 2.79 Å

The new volume is 166.00 $Å^3$, which is smaller then the previous unit cell volumes found which makes sense due to the low atomic mass atom Vanadium.

9.3 Electronic structure

The density of states for the electronic structure were calculated.

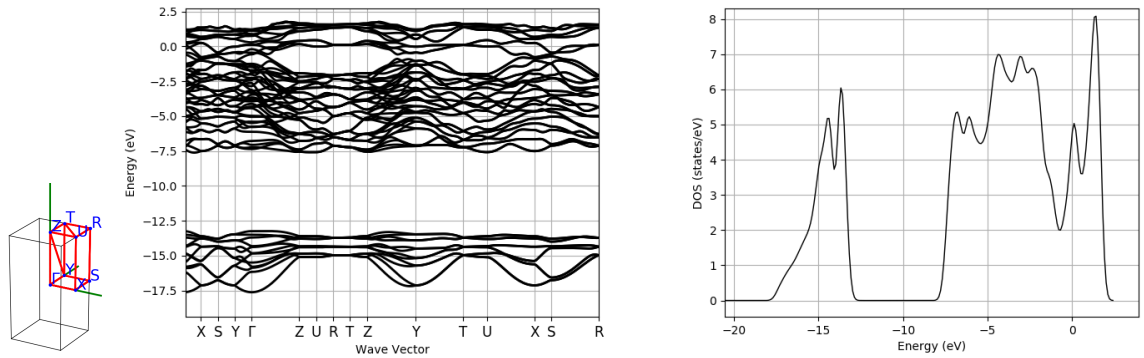

Figure 9.3.1: Electronic band structure and DOS for V_2N_3

9.4 Vibrational properties

The phononfrequencies at the Γ point were calculated and two unstable modes were found. This is an indicator that the structure is not stable, like previously predicted by Jiang *et al.*[3].

Table 9.4.1: Calculated phonon frequencies at the Γ-point.

Phonon energy [cm^{-1}]			
-79.9	446.8	278.6	567.8
-63.1	452.8	284.2	575.9
0.0	464.4	291.7	577.4
0.0	479.0	292.8	583.7
0.0	487.7	322.1	591.1
161.5	494.7	344.1	603.0

181.2	499.1	348.6	621.4
193.0	503.4	351.4	624.5
199.7	519.5	357.3	641.2
212.6	539.7	369.6	651.0
212.8	545.3	377.7	657.9
223.9	547.3	379.8	669.8
234.0	563.4	381.2	698.5
236.6	564.6	405.4	725.6
257.2	567.6	428.2	743.9

The phonon dispersion is calculated in the following and one can see instabilities in at Γ and instabilities going towards the Y-point.

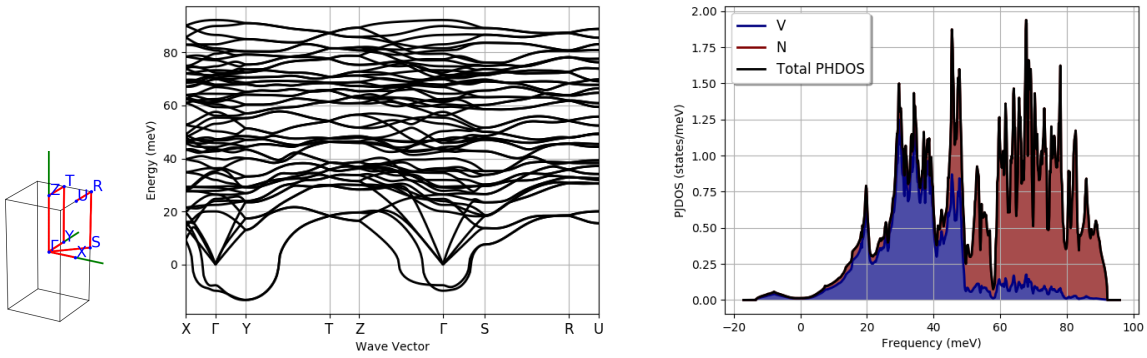

Figure 9.4.1: Phonon dispersion and the phonon DOS for V_2N_3 at ambient pressure for 8x8x24 and 0.05 smearing.

The structure is not further investigated, and the instability of the orthorhombic V_2N_3 is in agreement with predictions of Jiang *et al.*[3]

10 Trigonal V_2N_3

The stable trigonal V_2N_3 is investigated for its superconductivity in the following. Jiang *et al.*[3] found this stable form of the V_2N_3 in a random search as mentioned previously.

10.1 Convergence study

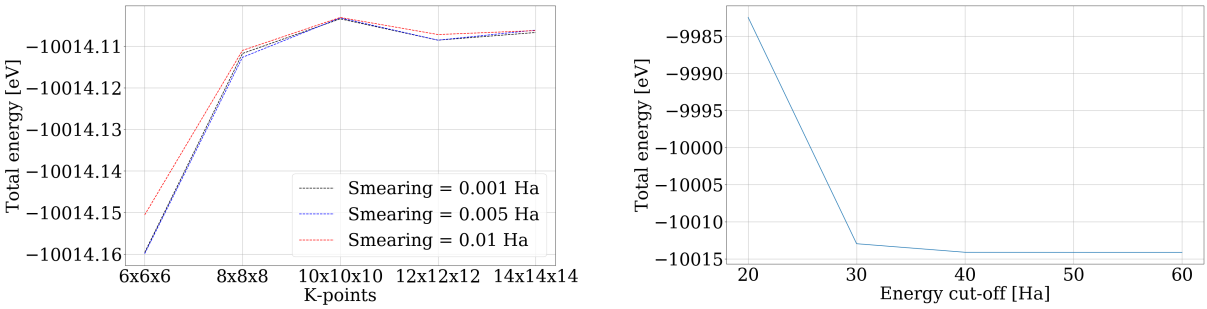

Figure 10.1.1: **K**-points and Smearing factor convergence (left). The smearing factor is chosen for the Cold smearing method. The energy cut-off convergence is also shown (right).

A **k**-point grid of 8x8x8 was chosen, which introduced an error of $\pm\ 5 \cdot 10^{-3}$ eV. A smearing of 0.01 Ha seemed to be converged faster for energy diverges less with respect to an increse in **k**-point grid then for other lower smearing factor. An energy cut-off of 40 Ha was chosen for further calculations giving the same accuracy like the **k**-point/smearing convergence.

10.2 Optimisation

An optimisation was conducted in order to find the ground state structure, while the input were the values produced by Jiang *et al.*[3]

Table 10.2.1: Optimized atomic coordinates in comparison with the literature findings in brackets.[3]

Atom	x	y	z
V1	$\frac{1}{3}$	$\frac{2}{3}$	0.698 (0.698)
N1	0.000	0.000	$\frac{1}{2}$
N2	0.000	0.000	0.892 (0.893)

The new cell parameter are the following:

- a = b = 2.81 Å
- c = 6.24 Å

The new volume is 109.51 $Å^3$, which is smaller then the previous unit cell volumes found. The cell parameter are in good agreement with previous theoretical result by Jiang et al.[3] (a = b = 2.82 Å, c = 6.25 Å).

10.3 Comparison with the orthorhombic V_2N_3

The structure for the orthorhombic V_2N_3 is compared with the trigonal structure. One can see how the trigonal structure shows alternating V-N-V stacking and a N-N dimer layer in the z-direction. This is a major difference for the orthorhombic structures do not form N-N dimers, that are anyways unusual for the transition metal nitrides.[3] The orthorhombic structure, as well as the tetragonal structure, shows a helpta-coordinated metal atom by nitrogen atoms. For the trigonal V_2N_3, the Vanadium is coordinated by just six nitrogen atoms leading to a octahedron.

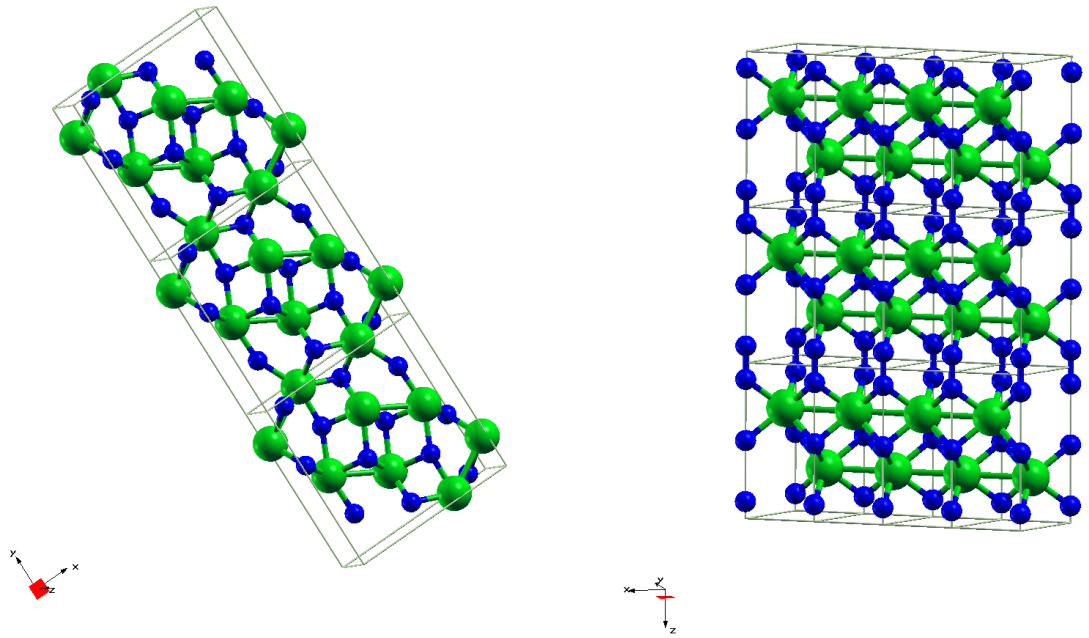

Figure 10.3.1: Orthorhombic structure (left) in comparison with the trigonal structure (right).

10.4 Electronic structure

The electronic bands structure and density of states for the were calculated for the electron density at Fermi-level plays an important role for the electron-phonon calculation.

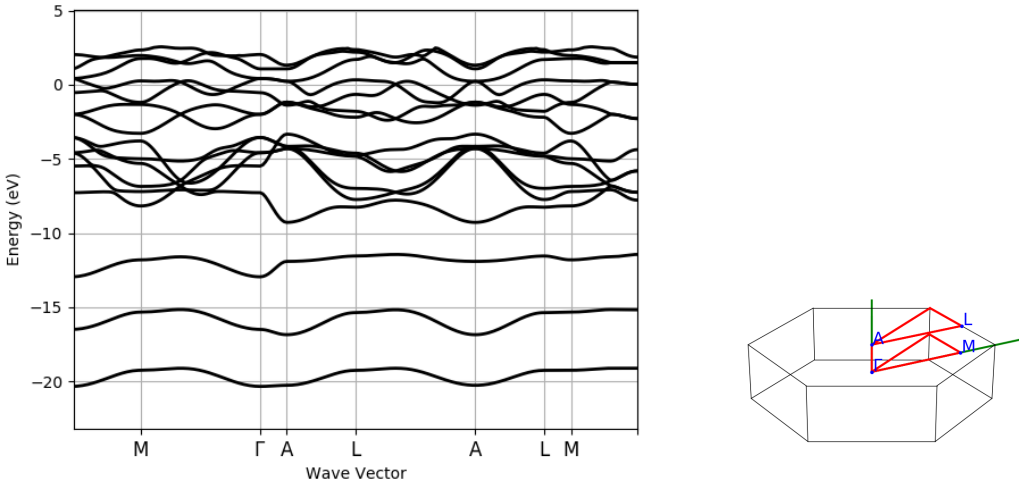

Figure 10.4.1: Electron band structure for V_2N_3

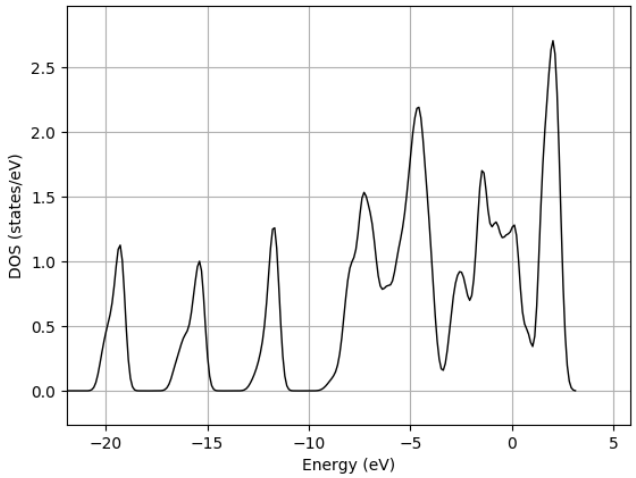

Figure 10.4.2: Density of states for the trigonal V_2N_3

The DOS is not perfectly in agreement with the literature DOS. The DOS all together lay in much lower DOS levels then in the literature.[3] While the highest peak can be found here at over 2.5 states/eV, the same peak reaches over 6 states/eV in the literature. The position of the peaks is in good agreement, while the intensities differ.

10.5 Vibrational properties

The Phononfrequencies at Γ-point are calculated and shown in the following table:

Phonon energy[cm^{-1}]	
0.0	526.53
0.0	526.53
0.0	557.89
200.52	557.89

200.52	637.22
415.19	714.26
415.19	1132.1
424.60	

In the next step, the phonondispersion is also produced for a **q**-point grid of 4x4x4.

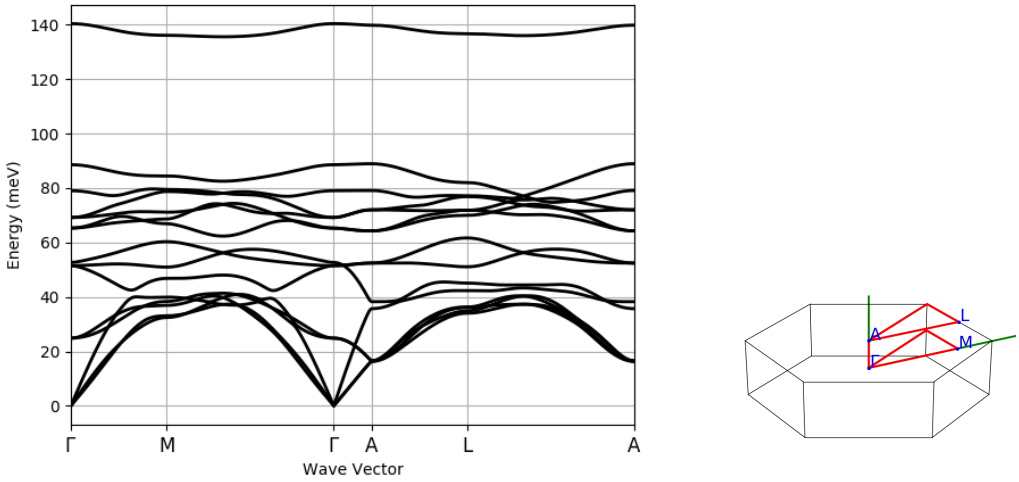

Figure 10.5.1: Phonondispersion for trigonal V_2N_3 at ambient pressure.

The phonon density of states were calculated with a interpolation to a grid of 48x48x48 q-points. A convergence test was conducted with 40x40x40 q-points showing no difference.

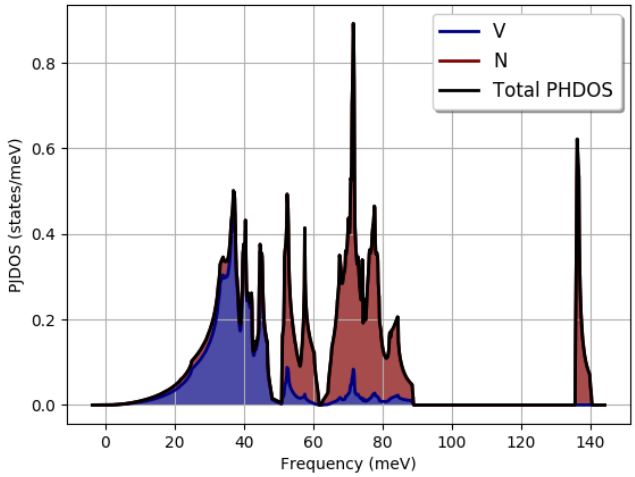

Figure 10.5.2: Phonon density of states for trigonal V_2N_3.

The phononmodes are stable for the trigonal V_2N_3, while 4x4x4 q-points are needed for a correct representation.

10.6 Superconductivity

The DDB-file and DVDB-files were produced from a calculation with 8x8x8 **k**-points, Smearing: 0.01 Ha and 4x4x4 **q**-points. They were used in the following to get a correct electron phonon calculation.

10.6.1 Convergence study

In order to converge the system, the ground state wave function was taken as an input and a new non self consistent calculation was performed with high **k**-point grids to get a new, more exact ground state wave function for the electron-phonon calculation. In that fashion, a convergence study with respect to the **k**-point grid and the smearing for tetrahedron smearing and the Gaussian smearing was conducted.

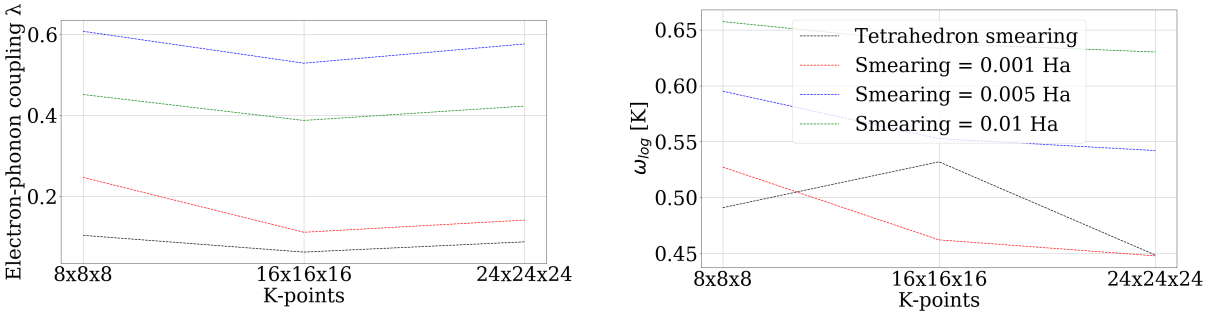

Figure 10.6.1: The convergence of the **k**-point grid and the smearing was conducted for the superconducting parameter EPC λ and for the logarithmic frequency $\omega_{\log}$.

One can see how the the value varies strongly for the tetrahedron smearing method. It seems the values are quite well converged, but it becomes clear how the values converge towards a different final value per smearing type. Therefore, we will investigate the tetrahedron smearing and also the Gaussian smearing with a smearing factor of 0.005 and a **k**-point grid of 24x24x24 to get behind the difference of there superconductive parameters.

10.6.2 Further Investigations and Results

After isotropic evaluation of the parameters from the electron-phonon coupling, the following indicators were found regarding the superconductivity. A Coulomb screening of 0.1 was chosen. The change of the Coulomb screening to 0.12 does not impact the results noteworthy.

Table 10.6.1: Results for the isotropic parameters for different interpolation techniques. The first one is interpolated but then the matrix elements are taken explicitly on the **k**-point grid and the second one is Fourier interpolated with respect to the DDB q-points (interpolated by ph_ngqpt). A **k**-point grid of 24x24x24 is used.

	Tetrahedron smearing		Gaussian smearing 0.005 Ha	
	Explicit Interpolation	Fourier interpolation	Explicit Interpolation	Fourier interpolation
T_c [K]	$2.45 \cdot 10^{8}$	$1.87 \cdot 10^{12}$	$6.22 \cdot 10^{-3}$	$8.59 \cdot 10^{-3}$
Isotropic λ	0.06899729	0.08784677	0.4887713	0.5768210
$\log(\omega)$ [K]	0.7377	0.4487	0.7871	0.5421
Positive moments of $\alpha^2F(\omega)$				
λ (ω^2)	$2.78 \cdot 10^{-7}$	$2.82 \cdot 10^{-7}$	$1.76 \cdot 10^{-6}$	$1.77 \cdot 10^{-6}$
λ (ω^3)	$6.90 \cdot 10^{-10}$	$6.84 \cdot 10^{-10}$	$4.13 \cdot 10^{-9}$	$4.07 \cdot 10^{-9}$
λ (ω^4)	$1.84 \cdot 10^{-12}$	$1.81 \cdot 10^{-12}$	$1.08 \cdot 10^{-11}$	$1.05 \cdot 10^{-11}$
λ (ω^5)	$5.29 \cdot 10^{-15}$	$5.13 \cdot 10^{-15}$	$3.09 \cdot 10^{-14}$	$2.97 \cdot 10^{-14}$

The McMillan temperature exploded due to the Coulomb repulsion being bigger then the electron-phonon coupling parameter λ for the tetrahedron smearing.

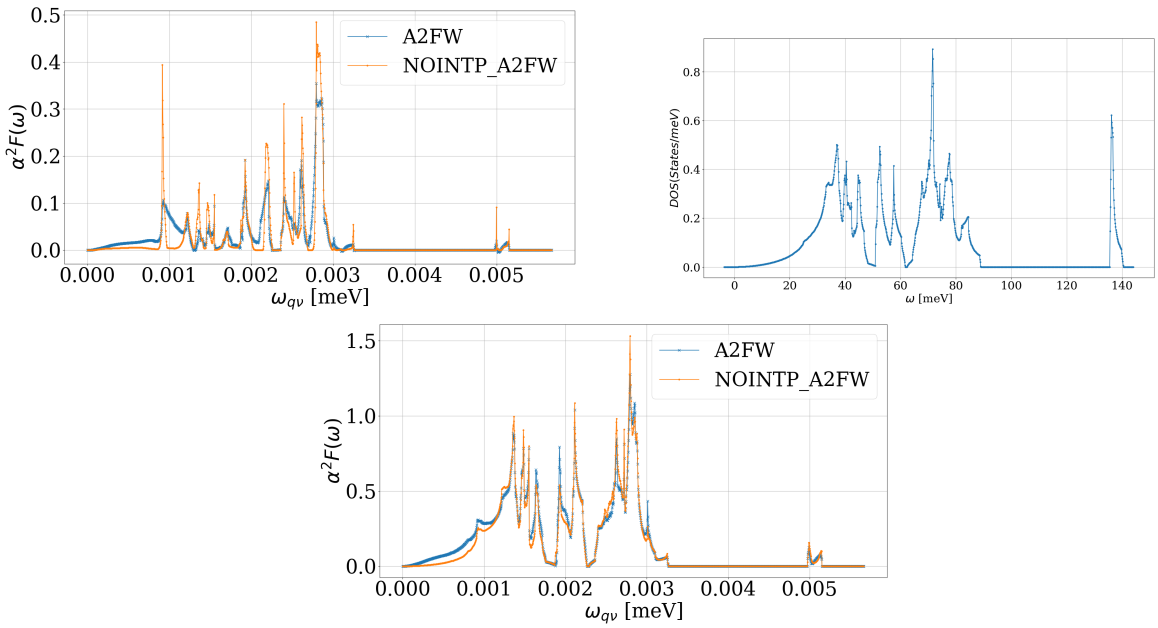

Figure 10.6.2: The spectral function α^2F as a function of the frequency ω calculated with tetrahedron smearing (top,left) and Gaussian smearing with a factor of 0.005 Ha (bottom) in comparison with the phonon DOS. A2FW denotes the explicit interpolation while NOINTP_A2FW shows the Fourier interpolation.

The spectral density does look very unusual for the tetrahedron smearing. Not only is the low frequency bit extremely linear, but also in comparison with the phonon DOS, the characteristics do differ massively, especially in between the peaks. Based on the result obtained through using tetrahedron method, which leads to the very low EPC λ, the trigonal V_2N_3 does not display superconducting behaviors. But tests with Gaussian smearing were conducted, giving very low superconducting parameters, but a sligthy higher EPC going up to 0.58. Furthermore, due to the low atomic mass, the logarithmic frequency should be much higher then the value obtained. But as seen previously, the logarithmic frequency calculated is massively underestimated. And the very high Debye temperature is another indicator that superconductivity might still be present, although it does not include the low frequencies sufficiently. The Eliash-

berg function for the Gaussian smearing looks much more dependable and it is very similar to the phonon DOS. When looking at the results, for the Explicitly interpolated (NOINPT_A2FW) Eliashberg function one can see a parabolic low frequency part for the Gaussian smearing function, which comes close to reality. Therefore, the results from the Gaussian smeared calculations will be taken and a EPC will be approximated. All three different Gaussian smearing factor results are taken into account to gain a range for the EPC. Further investigations are needed. A prediction of the logarithmic frequency will not be given and the same problem like in previous calculations remains, while the EPC remains questionable. All in all, it is probable that this structure does not display superconductivity or superconductivity with very low critical temperature. This could also be explained with the N-N dimers that are present in this structure. They might play a major role in lowering the electron phonon coupling.

Table 10.6.2: Superconducting parameters found for taking into account a Gaussian smearing for the electron-phonon calculation. The Debye temperature is an output from the phonon density of states calculation and the two values stem from the calculation from partial sums and the second value stems from the phDOS directly.

Isotropic λ	0.11-0.58
$\omega_{\log}$	/
Empirical parameter μ^*	0.1
McMillan critical temperature	/
Debye-temperature from phDOS-partial sums	551.64 - 606.92 K
Critical temperature calculated from equation (3.79)	0.00-9.40 K

11 Conclusion

The research around superconductivity at room temperature is still an ongoing venture, while superconductors under pressure play a major role since the discovery of superconductivity in sulfur hydride in 2014 because they still display a high and unknown potential. This project is motivated by exactly this potential of novel superconductors.
This project sheds light on one group of novel materials, the metal nitrides with a stoichiometry of M_2N_3 while the following group 5 metals are investigated: M = Tantalum, Niobium and Vanadium. Density functional theory is used to explore the electronic structure of the materials. The vibrational properties are then extracted with the help of perturbation approaches, that also give all the crucial input to calculate the superconducting parameter. For that reason, the first principle software Abinit was used.[11,12,13,14,15]
For all compounds, the following systematic framework was used: Firstly, a **k**-point and smearing convergence study was conducted, while a Cold smearing method was used, followed by a convergence of the energy cut-off. An optimization of the unit cell parameter is important to find the ground state atomic parameters and atomic coordinates. Once the correct set-up was picked, the electronic structure and vibrational properties were investigated, which give crucial input to the electron-phonon calculations. It was attempted then to use the following McMillan formula to gain information about the critical temperature, while all the parameter were accessible through first principles:

$$T_c = \frac{\omega_{\log}}{1.2} \exp\left[-\frac{1.04(1+\lambda)}{\lambda - \mu^*(1+0.62\lambda)}\right] \tag{11.1}$$

Due to the lack of accuracy of the logarithmic frequency, the following, original McMillan formula was taken into account for prediction:

$$T_c = \frac{\omega_D}{1.45} \exp\left[-\frac{1.04(1+\lambda)}{\lambda - \mu^*(1+0.62\lambda)}\right] \tag{11.2}$$

It uses the Debye temperature to gain a second critical temperature estimation. The Debye temperature is given by the very well converged phonon DOS calculation and it just varied due to two different methods used to gain it leading to another range. This prediction of superconductivity does not fully take the low frequency components of the spectral function into account and so it leads to an overestimation of the critical temperature, which is partially fixed due to the higher divisor ($1.2 \Longrightarrow 1.45$). The superconductivity has been explored for the material class M_2N_3, with M=Ta,Nb,V and to put all the results in a nutshell, a final table is produced.

Table 11.0.1: superconducting parameters predicted in this work for a μ^*=0.1. The range is gained by summarizing various experimental set-up's and approximations that lead to different values. It indicates that the results are not perfectly converged and a final value can not be given.

	Details	Isotropic λ	$\omega_{\log}$ [K]	McMillan Critical temperature (Eq. 11.1) [K]	Debye temperature [K]	McMillan Critical temperature (Eq. 11.2) [K]
η-Ta_2N_3	Input smearing: 0.01	0.87-1.16	0.13-36.54	0.01-3.14	82.06-161.20	3.74-11.46

η-Ta_2N_3	Input smearing: 0.05	0.77-0.97	0.27-20.34	0.012-1.350	169.66-193.75	6.07-10.65
η-Ta_2N_3 under pressure	Input smearing: 0.05	0.82-1.35	0.09-12.73	0.006-1.305	94.31-139.48	3.38-11.83
Tetragonal Ta_2N_3	Quantum Espresso	3.09-4.62	294.92-317.73	52.07-64.85	/	/
Tetragonal Ta_2N_3	Abinit	0.46-0.59	0.26-14.91	0.00-0.32	343.64-588.03	2.43-10.57
η-Nb_2N_3	Input smearing: 0.05	3.21-3.50	0.13-5.09	0.02-0.97	218.12-263.36	33.43-41.75
η-Nb_2N_3	Input smearing: 0.01	5.69-8.53	0.05-6.61	0.011-1.57	215.16-262.17	39.30-51.57
η-V_2N_3	Unstable					
Trigonal V_2N_3		0.11-0.58	/	/	551.64-606.92	0.00-9-40

Making predictions about superconducting behavior is still a challenging task, that has been just recently been made possible due to the development of new numerical and computational methods. It is still complicated to give definite numbers as results, especially predicting the critical temperature has to be always handled with highest care. The materials that are investigated in this work all had a complicated unit cell with up to 20 atoms which lead to very long computational times and less accurate results. As explained does density functional theory and density perturbation include various approximations, one noteworthy is the harmonic approximation, that might introduce an error source due to the fairly low atomic mass nitrogen. Furthermore, the McMillan formula itself is of empirical character, that might not be fully legitimate for our complicated systems, especially for systems with a high electron-phonon coupling like the Nb_2N_3 might be. There are more error sources, that can be further mentioned, like e.g. the lack of introduction of doping that apparently might play a major role for these structures. Nevertheless, it was possible to get close the experimental results and first tendencies of these materials were predicted. The electron phonon calculation, especially the interpolation used, has to be reviewed further to lead to more accurate values, as it is explained in this work. In the end, meaningful results could be obtained, the numerical power of Abinit was tested and the superconductivity of the η-Ta_2N_3 was confirmed. Especially the η-Nb_2N_3 is a promising candidate as a superconductor at ambient pressures with a very high electron-phonon coupling. The tetragonal Ta_2N_3 and the trigonal V_2N_3 are probably not showing superconductivity at all or just at rather low critical temperatures, but the vibrational properties were predicted and stability confirmed, making them potential candidates for industrial use due to their interesting mechanical properties, like e.g. high elastic stiffness, described by Jiang *et al.*.[3] In the following, the presented predictions are concluded and evaluated per material investigated.

Orthorhombic Tantalumnitride [Chapter 5,6,7]

This work was motivated by the high pressure and high temperature synthesis of the novel η-Ta_2N_3 superconductor, that has a critical temperature of ≈ 3 K.[7,2]. Therefore, a thorough investigation of the orthorhombic Ta_2N_3 was conducted. The found electronic structure and the ground state structure are in good agreement with literature.[97] A predicted Raman spectrum is produced for the η- Ta_2N_3 being in agreement with experimental Raman spectra.[2] For the orthorhombic Ta_2N_3, an interesting behavior was found. For low smearing, an unstable mode

appeared at the Z-point, which became stable for higher smearing. The compound is found to be very sensitive with regards to the smearing. Therefore, Fermi-Dirac smearing was also tested in order to gain valuable information about the potential physics leading to this behavior. Various tests made sure that the instability is tightly bound to the smearing and not another parameter. The Fermi-surface shows high sensitivity in Z-direction. Another set of calculations was conducted for the same material but at 26.065 GPa. For that compound a higher smearing was needed for stabilization. One possible explanation is, that the compound could be unstable at very low temperature, which is also dependent on the pressure. It could be explained through a pressure and temperature dependent stability curve. Another reason could also be, that the calculation itself does not take e.g. the doping into account that, as proposed by Jiang *et al.*[9], stabilizes the orthorhombic structure.
The electron-phonon calculation that followed strongly tends to underestimate the logarithmic frequency $\omega_{\log}$ and potentially also the electron-phonon coupling parameter λ which was carefully investigated. A numerical error, probably a wrong interpolation, leads to a bad estimation of the low frequency spectral density. In order to correct it, the low frequency components were neglected, substituted with more parabolic like curves or directly with a phonon DOS-like curve. To neglect the low frequency part of the curve is highly nonphysical and not very close to reality, but it leads to the most realistic values for the logarithmic frequency $\omega_{\log}$, while fitting the phonon DOS curve is an acceptable approximation because the spectral density function or Eliashberg function is the phonon DOS weighted by the electron-phonon coupling. The fitting of a function $y = x^p$ with different powers p was conducted to test the limits of the logarithmic frequency that can be gained with just changing the low frequency part. With the help of these estimations, a range of the logarithmic frequency $\omega_{\log}$ is predicted. The electron phonon coupling constant λ is taken from the original calculation without further approximations because it shows realistic values. It also varies, depending on which smearing method is used for the electron phonon calculation and therefore, a range is given. Therefore, a critical temperature range is recalculated that contains the experimental critical temperature. Although a good estimation of the EPC can be stated, the logarithmic coupling and the spectral function do need further investigation and tests to prove their accuracy. The values are shown in table 11.0.1. Interestingly, the electron-phonon coupling and critical temperature estimated tends to be lower if a high smearing factor is used for the input files, which is also the case for the η-Nb_2N_3 that will be discussed later. For the η-Ta_2N_3 under pressure, a high smearing had to be used due to its instability at low smearing. The results gained are comparable to the results for the ambient structure. The electron-phonon coupling parameter λ seems converged well enough and with all of that in mind, it is proposed to use the critical temperature calculated with formula 11.2 instead of formula 11.1 in order to predict the superconducting temperature.

Tetragonal Tantalumnitride [Chapter 7]

In order to fully understand the numerical background and its effects on the result, the tetragonal Ta_2N_3 was also taken into account. Previously calculated result with the software Quantum Espresso were accessible and were used for comparison.[16,17,10] Furthermore, this structure is of interest for it was shown how the structure is energetically more stable then the orthorhombic Ta_2N_3 leading to a potential to be synthesized. Again, the atomic parameters, coordinates and the electronic structure are in good agreement with literature.[9] The vibrational properties are comparable to the results gained by Quantum Espresso. The electron-phonon coupling calculation differ very strongly. Both results displayed questionable behaviors. The results from Quantum Espresso are not converged enough, so that the spectral density function and the superconducting parameters are roughly estimated. Interestingly, the superconducting parameters seems to be overestimated, showing opposite behavior then what is found for the results gained with Abinit. On the other hand, Abinit strongly underestimates the logarithmic frequency in every electron-phonon calculation conducted in this work. Again, the low frequency

part of the spectral density function α^2F seems to be too linear and an attempt to estimate it better was conducted and the logarithmic frequency $\omega_{\log}$ was recalculated leading to more realistic results that are probably still too low. Finally, the calculation made by Quantum Espresso is less accurate then the Abinit calculation due to the fact that the Abinit calculation is well converged. Following equation 11.1, the tetragonal Ta_2N_3 is rather not superconducting or superconducting at very low temperatures. Using the Equation 11.2 utilizing the more accurate Debye temperature, one can predict a critical temperature of around 2-3 K, because the real critical temperature is usually a tad below the predicted critical temperature by Equation (11.2). The possibility that the tetragonal Ta_2N_3 is not superconducting at all cannot be excluded.

Orthorhombic Niobiumnitride [Chapter 8]

Now that the accuracy of the electron phonon calculation is known more, the next compounds of interest were explored. The main driving force behind conducting these calculations is, that due to the exchange with lower atomic mass atoms, it is assumed that also the phonon frequencies are of higher order leading to a higher critical temperature. The next material that was investigated was the orthorhombic Nb_2N_3, whose predicted atomic parameter and coordinates, as well as the electronic structure are in agreement with the literature.[3] Noteworthy here is, that the Z-point soft mode did appear again for low smearing values, but less dominantly like for the η-Ta_2N_3. Like explained previously, a unrealistically low logarithmic frequency $\omega_{\log}$ was produced again. However, the electron-phonon coupling constant λ was much higher than for the Ta_2N_3-analog indicating strongly coupled behavior of electrons and phonons. Following the same framework like before, the logarithmic frequency is tried to be estimated more accurately, still leading to very low values, being against all expectations lower then for the η-Ta_2N_3. It seems that due to the weighting by the EPC, the low frequency components are highly favored. Due to the very low accuracy of the logarithmic frequency $\omega_{\log}$ and furthermore, due to the yet partially unknown origin of that numerical issue, it is proposed to use the Debye-temperature again to predict a critical temperature in the order of around 30 K. Further calculations have to be conducted to back up this hypothesis.

Vanadiumnitride [Chapter 9, 10]

Now following the principle that lower atomic mass atoms lead to higher frequencies and therefore higher critical temperatures, the Niobium atom was further substituted and the orthorhombic V_2N_3 was investigated. Literature predicts the η-V_2N_3 to be unstable, which is confirmed in this work. Jiang *et al.* predicted a stable trigonal form for the V_2N_3.[3] Again, the structural parameters as well as the electrical parameters are in acceptable agreement with the literature values, although the electron DOS does display lower levels. The superconductivity calculation varies a lot with the smearing method and factor chosen. The tetrahedron smearing shows unusual behavior of the Eliashberg function, while the Gaussian smearing seems to be giving a more realistic depiction. Therefore, the Gaussian smearing is used to predict a range for the electron-phonon coupling parameter, that seems to be very low and variable. The logarithmic frequency $\omega_{\log}$ is again massively underestimated. Due to the lower atomic mass of Vanadium and the low atomic mass nitrogen, one would expect much higher averaged logarithmic frequencies $\omega_{\log}$. Therefore, no estimate is given for this superconducting parameter. The Debye temperature is as expected very high and with equation (11.2), on can get a critical temperature up to around 9 K. As previously stated, this equation tends to overestimate the critical temperature. Finally, it is predicted that this compound is either not superconducting or superconducting with a very low critical temperatures. This could be due to the different structure. As explained in section 10.3, one can find N-N dimers in the unit cell, which is not the case for all the other structures investigated in this work. This might lower the EPC leading to a low superconducting potential for the N-N dimers do not display superconducting behavior.

12 Appendix

12.1 General

Abinit is run with the help of a file indicating the the input and output, called in the following t.files:

```
ta2n3.in
ta2n3.out
ta2n3_xi
ta2n3_xo
ta2n3_x
Ta.psp8
N.psp8
```

The psp8-files are Pseudopotentials downloaded from PseudoDojo.[51,50]

12.2 Case study: Orthorhombic Ta_2N_3

12.2.1 Groundstate (GS) calculation with varying k-points and smearing-values

```
autoparal 1
paral_kgb 1

ndtset 16 udtset  4 4
getwfk -1
getden -1

occopt 4

tsmear?1  0.001
tsmear?2  0.005
tsmear?3  0.01
tsmear?4  0.05

#Definition of the k-point grids
nshiftk 1
shiftk  0. 0. 0.

kptopt 1

ngkpt1?   6  6 18
ngkpt2?   8 8 24
ngkpt3?   10 10  30
ngkpt4?   12 12  36


#Definition of the unit cell
acell 8.19 8.24 3.00 Angstr
rprim  1.0  0.0  0.0
       0.0  1.0  0.0
       0.0  0.0  1.0

dilatmx 1.05
ecutsm  0.5
```

```
#Definition of the atom types
ntypat 2
znucl 73 7

#Defnition of the atoms
natom 20
typat 8*1 12*2
xred
  0.313  -0.021  0.25
  0.505   0.306  0.25
  0.813   0.521  0.75
  1.005   0.194  0.75
  -0.313  0.021  0.75
  -0.505  -0.306 0.75
  0.187   0.479  0.25
  -0.0050 0.806  0.25
  0.875   0.046  0.25
  0.549   0.879  0.25
  0.2     0.22   0.25
  1.375   0.454  0.75
  1.049   -0.379 0.75
  0.7     0.28   0.75
  -0.875  -0.046 0.75
  -0.549  -0.879 0.75
  -0.2    -0.22  0.75
  -0.375  0.546  0.25
  -0.0490 1.379  0.25
  0.3     0.72   0.25

#Definition of the planewave basis set
ecut  40.0

#Definition of the SCF procedure
nstep 100
toldfe 1.0d-12
```

12.2.2 GS calculation with varying energy cut-off

```
autoparal 1
paral_kgb 1

ndtset 5

getwfk -1
getden -1

occopt 4

tsmear  0.01

#Definition of the k-point grids
nshiftk 1
shiftk  0. 0. 0.

kptopt 1
ngkpt   10 10  30


#Definition of the unit cell
```

```
#acell 15.57134 15.47686  5.66918
acell 8.19 8.24 3.00 Angstr
rprim  1.0  0.0  0.0
       0.0  1.0  0.0
       0.0  0.0  1.0


dilatmx 1.05
ecutsm  0.5

#Definition of the atom types
ntypat 2

#Defnition of the atoms
natom 20
typat 8*1 12*2
xred
  0.313  -0.021  0.25
  0.505   0.306  0.25
  0.813   0.521  0.75
  1.005   0.194  0.75
 -0.313   0.021  0.75
 -0.505  -0.306  0.75
  0.187   0.479  0.25
 -0.0050  0.806  0.25
  0.875   0.046  0.25
  0.549   0.879  0.25
  0.2     0.22   0.25
  1.375   0.454  0.75
  1.049  -0.379  0.75
  0.7     0.28   0.75
 -0.875  -0.046  0.75
 -0.549  -0.879  0.75
 -0.2    -0.22   0.75
 -0.375   0.546  0.25
 -0.0490  1.379  0.25
  0.3     0.72   0.25

#Definition of the electronic cut-off
ecut?1  20.0
ecut?2  30.0
ecut?3  40.0
ecut?4  50.0
ecut?5  60.0


#Definition of the SCF procedure
nstep 100
toldfe 1.0d-12
```

12.2.3 Optimisation

```
autoparal 1
paral_kgb 1

getwfk -1
getden -1

occopt 4
```

```
tsmear  0.01

#Definition of the k-point grids
nshiftk 1
shiftk  0. 0. 0.

kptopt 1

ngkpt  10 10  30

#Definition of the unit cell
acell 8.19 8.24 3.00 Angstr
rprim  1.0  0.0  0.0
       0.0  1.0  0.0
       0.0  0.0  1.0

#Optimization of the lattice parameters
optcell 2
ionmov  2
ntime  30

dilatmx 1.05
ecutsm  0.5

#Definition of the atom types
ntypat 2
znucl 73 7

#Defnition of the atoms
natom 20
typat 8*1 12*2
xred
  0.313  -0.021  0.25
  0.505   0.306  0.25
  0.813   0.521  0.75
  1.005   0.194  0.75
 -0.313   0.021  0.75
 -0.505  -0.306  0.75
  0.187   0.479  0.25
 -0.0050  0.806  0.25
  0.875   0.046  0.25
  0.549   0.879  0.25
  0.2     0.22   0.25
  1.375   0.454  0.75
  1.049  -0.379  0.75
  0.7     0.28   0.75
 -0.875  -0.046  0.75
 -0.549  -0.879  0.75
 -0.2    -0.22   0.75
 -0.375   0.546  0.25
 -0.0490  1.379  0.25
  0.3     0.72   0.25

#Definition of the electronic cutt-off
ecut  40.0

#Definition of the SCF procedure
nstep 100
toldfe 1.0d-12
```

12.2.4 Vibrational properties

A GS-calculation was performed a priori and the WFK/DEN output filename was changed into a input filename and indicated in the t.files-file (ta2n3_xo_WFK to ta2n3_xi_WFK). The calculation for the frequencies at Γ-point were split into 15 calculations representing three degrees of freedom per irreducible atom (3N (N = number of atoms)), defined by $rfatpol$ and $rfdir$. The irreducible representation can be acquired through running a quick calculation with $nstep$ 1, $rfatpol$ 1 2 (over all atoms) and $rfdir$ 1 1 1 (all directions). This step was necessary in order to be able to split the calculation due to the big unit cell to increase efficiency. In the following the script is shown for one perturbation at the Γ-point (qpt 0 0 0).

```
utoparal 1
paral_kgb 1

#Response-function calculation
  rfphon   1
 rfatpol   1 1
   rfdir   1 0 0
    nqpt   1
     qpt   0 0 0

optdriver  1

prtpot 1

getwfk  1
getden  1

occopt 4

tsmear  0.005

#Definition of the k-point grids
nshiftk 1
shiftk  0. 0. 0.

kptopt 3
ngkpt   12 12 36


#Definition of the unit cell
acell 1.5460538263E+01  1.5534456499E+01   5.6626368033E+00
rprim  1.0  0.0  0.0
       0.0  1.0  0.0
       0.0  0.0  1.0

dilatmx 1.05
ecutsm  0.5

#Definition of the atom types
ntypat 2
znucl 73 7

#Defnition of the atoms
natom 20
typat 8*1 12*2
xred
  3.1289205513E-01 -2.0733250545E-02  2.5000000000E-01
  5.0511572192E-01  3.0574506751E-01  2.5000000000E-01
  8.1289205513E-01  5.2073325055E-01  7.5000000000E-01
  1.0051157219E+00  1.9425493249E-01  7.5000000000E-01
```

```
  -3.1289205513E-01  2.0733250545E-02  7.5000000000E-01
 -5.0511572192E-01 -3.0574506751E-01  7.5000000000E-01
  1.8710794487E-01  4.7926674945E-01  2.5000000000E-01
 -5.1157219200E-03  8.0574506751E-01  2.5000000000E-01
  8.7474076014E-01  4.6457910000E-02  2.5000000000E-01
  5.4910275390E-01  8.7922858942E-01  2.5000000000E-01
  1.9984580594E-01  2.1996617194E-01  2.5000000000E-01
  1.3747407601E+00  4.5354209000E-01  7.5000000000E-01
  1.0491027539E+00 -3.7922858942E-01  7.5000000000E-01
  6.9984580594E-01  2.8003382806E-01  7.5000000000E-01
  -8.7474076014E-01 -4.6457910000E-02  7.5000000000E-01
  -5.4910275390E-01 -8.7922858942E-01  7.5000000000E-01
  -1.9984580594E-01 -2.1996617194E-01  7.5000000000E-01
  -3.7474076014E-01  5.4645791000E-01  2.5000000000E-01
  -4.9102753901E-02  1.3792285894E+00  2.5000000000E-01
   3.0015419406E-01  7.1996617194E-01  2.5000000000E-01

#Definition of the planewave basis set
ecut  40.0

#Definition of the SCF procedure
nstep 100
toldfe  1.0d-10
```

After finishing the calculations for all the perturbations needed, one needs to merge the DDB-files to acquire the full dynamical matrix. The MRGDDB-utility is here used:

```
Ta2n3_total_DDB

15
../ta1/ta2n3_xo_DDB
../ta2/ta2n3_xo_DDB
../ta3/ta2n3_xo_DDB
../ta4/ta2n3_xo_DDB
../ta5/ta2n3_xo_DDB
../ta6/ta2n3_xo_DDB
../ta7/ta2n3_xo_DDB
../ta8/ta2n3_xo_DDB
../ta9/ta2n3_xo_DDB
../ta10/ta2n3_xo_DDB
../ta11/ta2n3_xo_DDB
../ta12/ta2n3_xo_DDB
../ta13/ta2n3_xo_DDB
../ta14/ta2n3_xo_DDB
../ta15/ta2n3_xo_DDB
```

This is then followed by running ANADDB with the help of the "ddb.files" to get the phonon-frequencies:

```
i.anaddb
o.anaddb
ta2n3_total_DDB
ta2n3band2eps
ta2n3dummy1
ta2n3dummy2
ta2n3dummy3
```

"ANADDB-file" to calculate the phononmodes at Γ-point for which one just has to merge the 15 perturbations at *qpt* 0 0 0:

```
asr 2
dipdip 0
chneut 0
ifcflag 1
ifcana 1
brav 1

nqpath 1
qpath
0 0 0

ngqpt 1 1 1
q1shft 0 0 0
```

The phonondispersion are calculated in the same style like the phononfrequencies at the Γ-point. But the variable qpt is varied according to how many q-points one wants to include. These can be gained through running a quick GS-calculation ($nstep$ =1) with a **k**-point grid that equals the wanted **q**-point grid. The log-file will contain the wanted q-point grid under kpt. Again, the DDB-files are all merged and the ANADDB-utility is used to acquire the phonondispersion:

```
ifcflag   1
ifcout    0

brav    1
ngqpt   2  2  6
nqshft  1
q1shft  3*0.0

chneut   1

dipdip  0
eivec  4

nqpath 9
qpath
0.5 0 0     # X
0 0 0       # Gamma
0 0.5 0     # Y
0 0.5 0.5   # MYZ
0 0 0.5     # Z
0 0 0       # Gamma
0.5 0.5 0   # MXY
0.5 0.5 0.5 # R
0.5 0 0.5   # MXZ
```

In order to obtain the phonon density of states, one includes in the "i.anaddb"-file the variables $ng2qpt$ 24 24 72 and $prtdos$ 2 so that a interpolation onto 24 24 72 **q**-points is achieved and the phonon density of states is printed.

```
ifcflag   1
ifcout    0

brav    1
ngqpt   2  2  6
nqshft  1

ng2qpt 24 24 72

prtdos 2
```

```
chneut   1
dipdip  0

eivec  4

nqpath 9
qpath
0.5 0 0 #X
0 0 0   #Gamma
0 0.5 0 # Y
0 0.5 0.5 #MYZ
0 0 0.5 #Z
0 0 0 #Gamma
0.5 0.5 0 #MXY
0.5 0.5 0.5 #R
0.5 0 0.5 #MXZ
```

12.2.5 Superconductivity

To calculate the critical temperature based on the electron-phonon coupling, one has to merge the DDB-files to gain a xi_DDB input file with mrgddb and all the POT-files to get a xi_DVDB input file with mrgdv. One also needs a file describing the wavefunction (xi_WFK) and the density (xi_DEN), whereas a groundstate calculation was conducted with kptopt 1, which means that the symmetry is taken fully into account to generate the k points in the Irreducible Brillouin Zone only, with the appropriate weights. After all four input files are obtained, the electron-phonon calculation can be started with the following script:

```
optdriver  7

irdwfk 1
eph_np_pqbks 12 1 1 20 1

ddb_ngqpt 2 2 6

ddb_shiftq 0 0 0
getddb 1

eph_mustar 0.12
eph_ngqpt_fine 8 8 24
eph_intmeth 2 # Tetrahedron smearing = 2, Gaussian smearing = 1
#eph_fsmear 0.005


ph_nqpath  16
ph_ngqpt 8 8 24
ph_nqshift 1
ph_qshift 0 0 0
ph_qpath
5.00000000E-01  0.00000000E+00  3.33333333E-01
0.00000000E+00  5.00000000E-01  3.33333333E-01
5.00000000E-01  5.00000000E-01  3.33333333E-01
0.00000000E+00  0.00000000E+00  5.00000000E-01
5.00000000E-01  0.00000000E+00  5.00000000E-01
0.00000000E+00  5.00000000E-01  5.00000000E-01
5.00000000E-01  5.00000000E-01  5.00000000E-01
0 0 0
5.00000000E-01  0.00000000E+00  0.00000000E+00
0.00000000E+00  5.00000000E-01  0.00000000E+00
5.00000000E-01  5.00000000E-01  0.00000000E+00
```

```
0.00000000E+00  0.00000000E+00  1.66666667E-01
5.00000000E-01  0.00000000E+00  1.66666667E-01
0.00000000E+00  5.00000000E-01  1.66666667E-01
5.00000000E-01  5.00000000E-01  1.66666667E-01
0.00000000E+00  0.00000000E+00  3.33333333E-01

dipdip 0
chneut 1

tsmear 0.01

#Definition of the k-point grids
nshiftk 1
shiftk  0. 0. 0.

kptopt 1
ngkpt   8 8 24

#Definition of the unit cell
acell 1.5460538263E+01  1.5534456499E+01   5.6626368033E+00
rprim  1.0  0.0  0.0
       0.0  1.0  0.0
       0.0  0.0  1.0

dilatmx 1.05
ecutsm  0.5

#Definition of the atom types
ntypat 2
znucl 73 7

#Defnition of the atoms
natom 20
typat 8*1 12*2
xred
   3.1289205513E-01 -2.0733250545E-02  2.5000000000E-01
   5.0511572192E-01  3.0574506751E-01  2.5000000000E-01
   8.1289205513E-01  5.2073325055E-01  7.5000000000E-01
   1.0051157219E+00  1.9425493249E-01  7.5000000000E-01
  -3.1289205513E-01  2.0733250545E-02  7.5000000000E-01
  -5.0511572192E-01 -3.0574506751E-01  7.5000000000E-01
   1.8710794487E-01  4.7926674945E-01  2.5000000000E-01
  -5.1157219200E-03  8.0574506751E-01  2.5000000000E-01
   8.7474076014E-01  4.6457910000E-02  2.5000000000E-01
   5.4910275390E-01  8.7922858942E-01  2.5000000000E-01
   1.9984580594E-01  2.1996617194E-01  2.5000000000E-01
   1.3747407601E+00  4.5354209000E-01  7.5000000000E-01
   1.0491027539E+00 -3.7922858942E-01  7.5000000000E-01
   6.9984580594E-01  2.8003382806E-01  7.5000000000E-01
  -8.7474076014E-01 -4.6457910000E-02  7.5000000000E-01
  -5.4910275390E-01 -8.7922858942E-01  7.5000000000E-01
  -1.9984580594E-01 -2.1996617194E-01  7.5000000000E-01
  -3.7474076014E-01  5.4645791000E-01  2.5000000000E-01
  -4.9102753901E-02  1.3792285894E+00  2.5000000000E-01
   3.0015419406E-01  7.1996617194E-01  2.5000000000E-01

#Definition of the planewave basis set
ecut  40.0
```

For the convergence, a NSCF-calculation was started for higher **k**-point grids with including a lower **k**-point xi_WFK input file. The NSCF-calculation is started with the flags $iscf$ -2, $getwfk$ 1 and $getden$ 1. The new WFK- and DEN-file can then be used for the electron-phonon

calculation. In order to change the smearing method, one has to change the flag $eph\_intmeth$ 2 (tetrahedron method) to 1 and for the Gaussian smearing which is turned on when defining $eph\_intmeth$ 1, one has to define a smearing factor with e.g. eph_fsmear 0.005.

12.3 Tetragonal Ta_2N_3

12.3.1 Groundstate calculation

The groundstate calculation input file is shown in the following after conducted **k**-point, smearing, energy cut-off convergence and optimization in the same fashion like for the orthorhombic Ta_2N_3.

```
occopt 4

tsmear  0.01

#Definition of the k-point grids
nshiftk 1
shiftk  0. 0. 0.

kptopt 1

ngkpt 12 12 12

getwfk 1
getden 1

#Definition of the unit cell
acell 5.6402825167E+00  5.6402825167E+00  1.0971498106E+01
rprim  1.0  0.0  0.0
       0.0  1.0  0.0
       0.0  0.0  1.0

dilatmx 1.05
ecutsm  0.5

#Definition of the atom types
ntypat 2
znucl 73 7

#Defnition of the atoms
natom 5
typat 2*1 3*2
xred
5.0000000000E-01  0.0000000000E+00  7.5635027836E-01
0.0000000000E+00  5.0000000000E-01 -7.5635027836E-01
5.0000000000E-01  0.0000000000E+00  1.4028931669E-01
0.0000000000E+00  5.0000000000E-01 -1.4028931669E-01
5.0000000000E-01  5.0000000000E-01  5.0000000000E-01

#Definition of the planewave basis set
ecut  40.0

#Definition of the SCF procedure
nstep 100
toldfe 1.0d-12
```

12.3.2 Vibrational properties

The rest of the calculations are conducted in the same order like for the orthorhombic Ta_2N_3, just that for the vibrational property calculations, the calculation was only split into one calculation per **q**-point while all the irreducible perturbations were always calculated at once:

```
#Response-function calculation
  rfphon   1
  rfatpol   1 5
  rfdir   1 1 1
  nqpt   1
  qpt 0.00000000E+00  0.00000000E+00  0.00000000E+00

optdriver  1

prtwf 0
prtpot 1

getwfk  1
getden  1

occopt 4

tsmear 0.01

#Definition of the k-point grids
nshiftk 1
shiftk  0. 0. 0.
kptopt 3

ngkpt 12 12 12

#Definition of the unit cell
acell 5.6402825167E+00  5.6402825167E+00  1.0971498106E+01
rprim  1.0  0.0  0.0
       0.0  1.0  0.0
       0.0  0.0  1.0

dilatmx 1.05
ecutsm  0.5

#Definition of the atom types
ntypat 2
znucl 73 7

#Defnition of the atoms
natom 5
typat 2*1 3*2
xred
5.0000000000E-01  0.0000000000E+00  7.5635027836E-01
0.0000000000E+00  5.0000000000E-01 -7.5635027836E-01
5.0000000000E-01  0.0000000000E+00  1.4028931669E-01
0.0000000000E+00  5.0000000000E-01 -1.4028931669E-01
5.0000000000E-01  5.0000000000E-01  5.0000000000E-01


#Definition of the planewave basis set
ecut  40.0

#Definition of the SCF procedure
nstep 100
toldfe 1.0d-12
```

The "i.anaddb" input file for ANADDB, looked like the following for the 4x4x4 **q**-point case:

```
ifcflag   1
ifcout    0

brav    1
ngqpt   4  4  4
nqshft  1
q1shft  3*0.0

chneut   1

dipdip  0

eivec  4

nqpath 9
qpath
 0.00000   0.00000   0.00000             # $\Gamma$
 0.0000000000 0.5000000000 0.0000000000  #X
 0.5000000000 0.5000000000 0.0000000000  #M
 0.00000   0.00000   0.00000             # $\Gamma$
 0.0000000000 0.0000000000 0.5000000000  #Z
 0.0000000000 0.5000000000 0.5000000000  #R
 0.5000000000 0.5000000000 0.5000000000  #A
 0.0000000000 0.0000000000 0.5000000000  #Z
```

For calculating the phonon DOS, the flags $ng2qpt$ 48 48 48 and $prtdos$ 2 were simply included.

12.4 Orthorhombic Nb_2N_3

For the orthorhombic Nb_2N_3, the same framework like the the Orthorhombic Ta_2N_3 was used except that the atomic coordinates ($xred$), atomic parameter ($acell$) and the atomic mass was changed to $znucl$ 41 7. Due to the same symmetry of the unit cell and similar size, the scripts are easily reused. Therefore, just a ground state calculation script is presented after **k**-point, smearing and energy cut-off convergence.

```
occopt 4

tsmear  0.05

#Definition of the k-point grids
nshiftk 1
shiftk  0. 0. 0.

kptopt 1
ngkpt   6 6 18

#Definition of the unit cell
acell  1.5394867066E+01  1.5598921780E+01  5.6695759203E+00
rprim  1.0  0.0  0.0
       0.0  1.0  0.0
       0.0  0.0  1.0

dilatmx 1.05
ecutsm  0.5

#Definition of the atom types
ntypat 2
znucl 41 7
```

```
#Defnition of the atoms
natom 20
typat 8*1 12*2
xred
       3.1317926267E-01 -2.1631480756E-02  2.5000000000E-01
       5.0429140654E-01  3.0561764278E-01  2.5000000000E-01
       8.1317926267E-01  5.2163148076E-01  7.5000000000E-01
       1.0042914065E+00  1.9438235722E-01  7.5000000000E-01
      -3.1317926267E-01  2.1631480756E-02  7.5000000000E-01
      -5.0429140654E-01 -3.0561764278E-01  7.5000000000E-01
       1.8682073733E-01  4.7836851924E-01  2.5000000000E-01
      -4.2914065412E-03  8.0561764278E-01  2.5000000000E-01
       8.7352233205E-01  4.6194995046E-02  2.5000000000E-01
       5.4813385178E-01  8.7877990050E-01  2.5000000000E-01
       2.0151345075E-01  2.2143572274E-01  2.5000000000E-01
       1.3735223321E+00  4.5380500495E-01  7.5000000000E-01
       1.0481338518E+00 -3.7877990050E-01  7.5000000000E-01
       7.0151345075E-01  2.7856427726E-01  7.5000000000E-01
      -8.7352233205E-01 -4.6194995046E-02  7.5000000000E-01
      -5.4813385178E-01 -8.7877990050E-01  7.5000000000E-01
      -2.0151345075E-01 -2.2143572274E-01  7.5000000000E-01
      -3.7352233205E-01  5.4619499505E-01  2.5000000000E-01
      -4.8133851778E-02  1.3787799005E+00  2.5000000000E-01
       2.9848654925E-01  7.2143572274E-01  2.5000000000E-01


#Definition of the planewave basis set
ecut  40.0

#Definition of the SCF procedure
nstep 100
toldfe  1.0d-12
```

12.5 Orthorhombic V_2N_3

A ground state calculation script is presented after **k**-point, smearing and energy cut-off convergence.

```
getwfk  1
getden  1

occopt 4

tsmear  0.01

#Definition of the k-point grids
nshiftk 1
shiftk  0. 0. 0.

kptopt 3
ngkpt   8 8 24

#Definition of the unit cell

acell      1.4535038632E+01  1.4625149356E+01  5.2696875045E+00
rprim  1.0  0.0  0.0
       0.0  1.0  0.0
       0.0  0.0  1.0
```

```
dilatmx 1.05
ecutsm  0.5

#Definition of the atom types
ntypat 2
znucl 23 7

#Defnition of the atoms
natom 20
typat 8*1 12*2
xred
       3.1232931698E-01 -2.5061906728E-02  2.5000000000E-01
       4.9943017558E-01  3.0302227673E-01  2.5000000000E-01
       8.1232931698E-01  5.2506190673E-01  7.5000000000E-01
       9.9943017558E-01  1.9697772327E-01  7.5000000000E-01
      -3.1232931698E-01  2.5061906728E-02  7.5000000000E-01
      -4.9943017558E-01 -3.0302227673E-01  7.5000000000E-01
       1.8767068302E-01  4.7493809327E-01  2.5000000000E-01
       5.6982441832E-04  8.0302227673E-01  2.5000000000E-01
       8.7210464357E-01  4.4330388663E-02  2.5000000000E-01
       5.4966442446E-01  8.8132024789E-01  2.5000000000E-01
       1.9515383776E-01  2.2062015556E-01  2.5000000000E-01
       1.3721046436E+00  4.5566961134E-01  7.5000000000E-01
       1.0496644245E+00 -3.8132024789E-01  7.5000000000E-01
       6.9515383776E-01  2.7937984444E-01  7.5000000000E-01
      -8.7210464357E-01 -4.4330388663E-02  7.5000000000E-01
      -5.4966442446E-01 -8.8132024789E-01  7.5000000000E-01
      -1.9515383776E-01 -2.2062015556E-01  7.5000000000E-01
      -3.7210464357E-01  5.4433038866E-01  2.5000000000E-01
      -4.9664424456E-02  1.3813202479E+00  2.5000000000E-01
       3.0484616224E-01  7.2062015556E-01  2.5000000000E-01


#Definition of the planewave basis set
ecut  40.0

#Definition of the SCF procedure
nstep 100
toldfe  1.0d-10
```

12.6 Trigonal V_2N_3

12.6.1 Ground state calculation

A ground state calculation script is presented after **k**-point, smearing and energy cut-off convergence.

```
occopt 4

tsmear 0.01

#Definition of the k-point grids
nshiftk 1
shiftk  0. 0. 0.

kptopt 1
ngkpt   8 8 8
```

```
#Definition of the unit cell
acell 5.3182111211E+00  5.3182111211E+00  1.1796921858E+01
rprim  0.86602540378  0.5  0.0
      -0.86602540378  0.5  0.0
       0.0            0.0  1.0

dilatmx 1.05
ecutsm  0.5

#Definition of the atom types
ntypat 2
znucl 23 7

#Defnition of the atoms
natom 5
typat 2*1 3*2
xred
    3.3333333333E-01  6.6666666667E-01  6.9822313377E-01
    6.6666666667E-01  3.3333333333E-01 -6.9822313377E-01
    1.5745180509E-28  3.1490361018E-28  5.0000000000E-01
    1.4170137260E-28  2.4466185515E-28  8.9240154632E-01
    1.0792355752E-28  2.5458800511E-28 -8.9240154632E-01

#Definition of the planewave basis set
ecut  40.0


#Definition of the SCF procedure
nstep 100
toldfe  1.0d-10
```

12.6.2 Vibrational calculation

Like for the tetragonal Ta_2N_3 case, we have a small sized system. Therefore, only the **q**-point flag (*qpt*) is changed.

```
#Response-function calculation
  rfphon   1
 rfatpol   1 5
   rfdir   1 1 1
    nqpt   1
     qpt   0 0 0

optdriver  1

prtwf 0
prtpot 1

getwfk  1
getden  1

occopt 4

tsmear 0.01

#Definition of the k-point grids
nshiftk 1
shiftk  0. 0. 0.

kptopt 3
```

```
ngkpt   8 8 8


#Definition of the unit cell
acell 5.3182111211E+00  5.3182111211E+00  1.1796921858E+01
rprim  0.86602540378  0.5  0.0
      -0.86602540378  0.5  0.0
       0.0            0.0  1.0

dilatmx 1.05
ecutsm  0.5

#Definition of the atom types
ntypat 2
znucl 23 7

#Defnition of the atoms
natom 5
typat 2*1 3*2
xred
```

The "i.anaddb" input file for ANADDB, looked like the following for the 4x4x4 **q**-point case. For calculating the phonon DOS, the flags $ng2qpt$ 48 48 48 and $prtdos$ 2 were simply included.

```
ifcflag   1
ifcout    0

brav    1
ngqpt   4  4  4
nqshft  1
q1shft  3*0.0

!ng2qpt 48 48 48
!prtdos 2

chneut   1

dipdip  0

eivec  4

nqpath 8
qpath
    +0.00000  +0.00000  +0.00000  # $\Gamma$
    +0.50000  +0.00000  +0.00000  # M
    +0.33333  +0.33333  +0.00000  # K
    +0.00000  +0.00000  +0.00000  # $\Gamma$
    +0.00000  +0.00000  +0.50000  # A
    +0.50000  +0.00000  +0.50000  # L
    +0.33333  +0.33333  +0.50000  # H
    +0.00000  +0.00000  +0.50000  # A
```

12.6.3 Superconductivity

A electron-phonon calculation script is included in the following. Like for the previous cases, the smearing method and factor were varied and the **k**-points were also varied (after production of a new xi_WFK with the help of a NSCF-ground state calculation (indicated with $iscf$ -2, $getwfk$ 1 and $getden$ 1).

```
optdriver  7

irdwfk 1

ddb_ngqpt 4 4 4
ddb_shiftq 0 0 0
getddb 1

eph_mustar 0.1
eph_intmeth 2 #Tetrahedron method (1 Gaussian method)
#eph_fsmear 0.001

eph_ngqpt_fine 8 8 8

ph_nqpath  11
ph_ngqpt 8 8 8
ph_nqshift 1
ph_qshift 0 0 0
ph_qpath
    +0.00000  +0.00000  +0.00000  # $\Gamma$
    +0.50000  +0.00000  +0.00000  # M
    +0.33333  +0.33333  +0.00000  # K
    +0.00000  +0.00000  +0.00000  # $\Gamma$
    +0.00000  +0.00000  +0.50000  # A
    +0.50000  +0.00000  +0.50000  # L
    +0.33333  +0.33333  +0.50000  # H
    +0.00000  +0.00000  +0.50000  # A
    +0.50000  +0.00000  +0.50000  # L
    +0.50000  +0.00000  +0.00000  # M
    +0.33333  +0.33333  +0.00000  # K
    +0.33333  +0.33333  +0.50000  # H

dipdip 0
chneut 1

tsmear 0.01

#Definition of the k-point grids
nshiftk 1
shiftk  0. 0. 0.

kptopt 1
ngkpt   8 8 8

#Definition of the unit cell
acell 5.3182111211E+00  5.3182111211E+00  1.1796921858E+01
rprim  0.86602540378  0.5  0.0
      -0.86602540378  0.5  0.0
       0.0            0.0  1.0

dilatmx 1.05
ecutsm  0.5

#Definition of the atom types
ntypat 2
znucl 23 7

#Defnition of the atoms
natom 5
typat 2*1 3*2
xred
    3.3333333333E-01  6.6666666667E-01  6.9822313377E-01
```

```
    6.6666666667E-01  3.3333333333E-01 -6.9822313377E-01
    1.5745180509E-28  3.1490361018E-28  5.0000000000E-01
    1.4170137260E-28  2.4466185515E-28  8.9240154632E-01
    1.0792355752E-28  2.5458800511E-28 -8.9240154632E-01

#Definition of the planewave basis set
ecut  40.0

#Definition of the SCF procedure
nstep 100
toldfe  1.0d-10
```

13 Bibliography

[1]J. A. Flores-Livas, L. Boeri, A. Sanna, G. Profeta, R. Arita, and M. Eremets, *A perspective on conventional high-temperature superconductors at high pressure: methods and materials*, 2020.

[2]A. Zerr and M. A. Méasson, *(private communication)*, (accessed: 01.06.2020).

[3]C. Jiang, Z. Lin, and Y. Zhao, "First principles prediction of vanadium and niobium nitrides with M2N3 stoichiometry", Scr. Mater. **63**, 532–535 (2010).

[4]R. Parks, *Superconductivity* (Marcel Dekker, INC.,New York, 1969).

[5]C. J. Pickard, I. Errea, and M. I. Eremets, "Superconducting hydrides under pressure", Annual Review of Condensed Matter Physics **11**, 57–76 (2020).

[6]K. M. Shen and J. Seamus Davis, "Cuprate high-tc superconductors", Materials today **11**, 14–21 (2008).

[7]A Zerr, G Miehe, J Li, D. A. Dzivenko, V. K. Bulatov, H. Hoefer, N. Bolfan-Casanova, M. Fialin, G. Brey, R. Watanabe, and M. Yoshimura, "High-pressure synthesis of tantalum nitride having orthorhombic u_2s_3 structure", Advanced Functional Materials **19**, 2282–2288 (2009).

[8]A. Friedrich, B. Winkler, L. Bayarjargal, E. A. Juarez Arellano, W. Morgenroth, J. Biehler, F. Schröder, J. Yan, and S. M. Clark, "In situ observation of the reaction of tantalum with nitrogen in a laser heated diamond anvil cell", J. Alloys Compd. **502**, 5–12 (2010).

[9]C. Jiang, Z. Lin, and Y. Zhao, "Thermodynamics and mechanical stabilities of tantalum nitride", Physical Review letters **103**, 185501 (28 October 2009).

[10]A. Dudzinski, "Theoretical investigation of superconductivity in Ta and Ta-based materials from first-principles calculations", 1–47 (2019).

[11]X. Gonze, B. Amadon, G. Antonius, F. Arnardi, L. Baguet, J.-M. Beuken, J. Bieder, F. Bottin, J. Bouchet, E. Bousquet, N. Brouwer, F. Bruneval, G. Brunin, T. Cavignac, J.-B. Charraud, W. Chen, M. Côté, S. Cottenier, J. Denier, G. Geneste, P. Ghosez, M. Giantomassi, Y. Gillet, O. Gingras, D. R. Hamann, G. Hautier, X. He, N. Helbig, N. Holzwarth, Y. Jia, F. Jollet, W. Lafargue-Dit-Hauret, K. Lejaeghere, M. A. L. Marques, A. Martin, C. Martins, H. P. C. Miranda, F. Naccarato, K. Persson, G. Petretto, V. Planes, Y. Pouillon, S. Prokhorenko, F. Ricci, G.-M. Rignanese, A. H. Romero, M. M. Schmitt, M. Torrent, M. J. van Setten, B. V. Troeye, M. J. Verstraete, G. Zérah, and J. W. Zwanziger, "The abinit project: impact, environment and recent developments", Comput. Phys. Commun. **248**, 107042 (2020).

[12]X. Gonze, F. Jollet, F. Abreu Araujo, D. Adams, B. Amadon, T. Applencourt, C. Audouze, J.-M. Beuken, J. Bieder, A. Bokhanchuk, E. Bousquet, F. Bruneval, D. Caliste, M. Côté, F. Dahm, F. Da Pieve, M. Delaveau, M. Di Gennaro, B. Dorado, C. Espejo, G. Geneste, L. Genovese, A. Gerossier, M. Giantomassi, Y. Gillet, D. Hamann, L. He, G. Jomard, J. Laflamme Janssen, S. Le Roux, A. Levitt, A. Lherbier, F. Liu, I. Lukačević, A. Martin, C. Martins, M. Oliveira, S. Poncé, Y. Pouillon, T. Rangel, G.-M. Rignanese, A. Romero, B. Rousseau, O. Rubel, A. Shukri, M. Stankovski, M. Torrent, M. Van Setten, B. Van Troeye, M. Verstraete, D. Waroquiers, J. Wiktor, B. Xu, A. Zhou, and J. Zwanziger, "Recent developments in the ABINIT software package", Comput. Phys. Commun. **205**, 106–131 (2016).

[13]X. Gonze, B. Amadon, P.-M. Anglade, J.-M. Beuken, F. Bottin, P. Boulanger, F. Bruneval, D. Caliste, R. Caracas, M. Côté, T. Deutsch, L. Genovese, P. Ghosez, M. Giantomassi, S. Goedecker, D. Hamann, P. Hermet, F. Jollet, G. Jomard, S. Leroux, M. Mancini, S. Mazevet, M. Oliveira, G. Onida, Y. Pouillon, T. Rangel, G.-M. Rignanese, D. Sangalli, R. Shaltaf, M. Torrent, M. Verstraete, G. Zerah, and J. Zwanziger, "ABINIT: First-principles approach to material and nanosystem properties", Comput. Phys. Commun. **180**, 2582–2615 (2009).

[14]X. Gonze, G.-M. Rignanese, M. Verstraete, J.-M. Beuken, Y. Pouillon, R. Caracas, F. Jollet, M. Torrent, G. Zerah, M. Mikami, P. Ghosez, M. Veithen, J.-Y. Raty, V. Olevano, F. Bruneval, L. Reining, R. Godby, G. Onida, and D. H. D.C. Allan, "A brief introduction to the ABINIT software package", Zeitschrift für Kristallographie - Crystalline Materials **220**, 558–562 (2005).

[15]X. Gonze, J.-M. Beuken, R. Caracas, F. Detraux, M. Fuchs, G.-M. Rignanese, L. Sindic, M. Verstraete, G. Zerah, F. Jollet, M. Torrent, A. Roy, M. Mikami, P. Ghosez, J.-Y. Raty, and D. Allan, "First-principles computation of material properties: The ABINIT software project", Computational Materials Science **25**, 478–492 (2002).

[16]P Giannozzi, O Andreussi, T Brumme, O Bunau, M. B. Nardelli, M Calandra, R Car, C Cavazzoni, D Ceresoli, M Cococcioni, N Colonna, I Carnimeo, A. D. Corso, S de Gironcoli, P Delugas, R. A. D. Jr, A Ferretti, A Floris, G Fratesi, G Fugallo, R Gebauer, U Gerstmann, F Giustino, T Gorni, J Jia, M Kawamura, H.-Y. Ko, A Kokalj, E Küçükbenli, M Lazzeri, M Marsili, N Marzari, F Mauri, N. L. Nguyen, H.-V. Nguyen, A. O. de-la Roza, L Paulatto, S Poncé, D Rocca, R Sabatini, B Santra, M Schlipf, A. P. Seitsonen, A Smogunov, I Timrov, T Thonhauser, P Umari, N Vast, X Wu, and S Baroni, "Advanced capabilities for materials modelling with quantum espresso", Journal of Physics: Condensed Matter **29**, 465901 (2017).

[17]P. Giannozzi, S. Baroni, N. Bonini, M. Calandra, R. Car, C. Cavazzoni, D. Ceresoli, G. L. Chiarotti, M. Cococcioni, I. Dabo, A. Dal Corso, S. de Gironcoli, S. Fabris, G. Fratesi, R. Gebauer, U. Gerstmann, C. Gougoussis, A. Kokalj, M. Lazzeri, L. Martin-Samos, N. Marzari, F. Mauri, R. Mazzarello, S. Paolini, A. Pasquarello, L. Paulatto, C. Sbraccia, S. Scandolo, G. Sclauzero, A. P. Seitsonen, A. Smogunov, P. Umari, and R. M. Wentzcovitch, "Quantum espresso: a modular and open-source software project for quantum simulations of materials", Journal of Physics: Condensed Matter **21**, 395502 (19pp) (2009).

[18]A. D. Grockowiak, M. Ahart, T. Helm, W. A. Coniglio, R. Kumar, M. Somayazulu, Y. Meng, M. Oliff, V. Williams, N. W. Ashcroft, R. J. Hemley, and S. W. Tozer, *Hot hydride superconductivity above 550 k*, 2020.

[19]E. P. Wigner and H. B. Huntington, *On the possibility of a metallic modification of hydrogen*, 1935.

[20]R. P. Dias and I. F. Silvera, *Observation of the wigner-huntington transition to metallic hydrogen*, 2017.

[21]A. Goncharov and V. Struzhkin, "Comment on observation of the wigner-huntington transition to metallic hydrogen", Science **357** (2017).

[22]S. Desgreniers, *A milestone in the hunt for metallic hydrogen*, 2020.

[23]J. Feng, W. Grochala, T. Jaroń, R. Hoffmann, A. Bergara, and N Ashcroft, "Structures and potential superconductivity in sih 4 at high pressure: en route to "metallic hydrogen"", Physical review letters **96**, 017006 (2006).

[24]A. P. Drozdov, V. S. Minkov, S. P. Besedin, P. P. Kong, M. A. Kuzovnikov, D. A. Knyazev, and M. I. Eremets, *Superconductivity at 215 k in lanthanum hydride at high pressures*, 2018.

[25]M. Somayazulu, M. Ahart, A. K. Mishra, Z. M. Geballe, M. Baldini, Y. Meng, V. V. Struzhkin, and R. J. Hemley, "Evidence for superconductivity above 260 k in lanthanum superhydride at megabar pressures", Phys. Rev. Lett. **122**, 027001 (2019).

[26]A. P. Drozdov, P. P. Kong, V. S. Minkov, S. P. Besedin, M. A. Kuzovnikov, S. Mozaffari, L. Balicas, F. F. Balakirev, D. E. Graf, V. B. Prakapenka, and et al., "Superconductivity at 250 k in lanthanum hydride under high pressures", Nature **569**, 528–531 (2019).

[27]X.-J. Chen, V. V. Struzhkin, Z. Wu, M. Somayazulu, J. Qian, S. Kung, A. N. Christensen, Y. Zhao, R. E. Cohen, H.-k. Mao, and R. J. Hemley, "Hard superconducting nitrides", Proceedings of the National Academy of Sciences **102**, 3198–3201 (2005).

[28]D. V. Semenok, A. G. Kvashnin, A. G. Ivanova, V. Svitlyk, V. Y. Fominski, A. V. Sadakov, O. A. Sobolevskiy, V. M. Pudalov, I. A. Troyan, and A. R. Oganov, "Superconductivity at 161k in thorium hydride thh10: synthesis and properties", Materials Today **33**, 36–44 (2020).

[29]P. P. Kong, V. S. Minkov, M. A. Kuzovnikov, S. P. Besedin, A. P. Drozdov, S. Mozaffari, L. Balicas, F. F. Balakirev, V. B. Prakapenka, E. Greenberg, D. A. Knyazev, and M. I. Eremets, *Superconductivity up to 243 k in yttrium hydrides under high pressure*, 2019.

[30]*Popular information*, `https://www.nobelprize.org/prizes/physics/2003/popular-information/`, 2003.

[31]R. Heid, "Electron-phonon coupling", Autumn school on correlated electrons (2017).

[32]C. J. Cramer, *Essentials of computational chemsitry theories and models*, 2nd ed. (John Wiley & Sons, Ltd, 2004).

[33]A. Cano, "Notes of superconductivity", (2019).

[34]S. Ponce, "Electron-phonon coupling using quantum espresso, tutorial tue.5, hands-on session", (2018).

[35]A. Sanna, J. Flores-Livas, A. Davydov, G. Profeta, K. Dewhurst, and E. Gross, "Ab initio eliashberg theory: making genuine predictions of superconducting features", Journal of the Physical Society of Japan **87**, 041012 (2018).

[36]D. Arovas and C. Wu, "Lecture notes on superconductivity (a work in progress)", (2016).

[37]G. A. Ummarino, "Eliashberg theory", Autumn school on correlated electrons (September 2013).

[38]M. Wierzbowska, S. Gironcoli, and P. Giannozzi, "Origins of low- and high-pressure discontinuities of t_c in niobium", **v1** (7 Feb 2006).

[39]*Bloch's Theorem and Plane Wave Basis Sets*, S. Clark , 15.05.2019.

[40]C. J. Cramer, *Essentials of computational chemsitry theories and models*, 2nd ed. (John Wiley & Sons, Ltd, 2004).

[41]A. G. Pueyo, M. A. L. Marques, A. Rubio, and A. Castro, "Propagators for the time-dependent kohn–sham equations: multistep, runge–kutta, exponential runge–kutta, and commutator free magnus methods", Journal of Chemical Theory and Computation **14**, 3040–3052 (2018).

[42]J. P. Perdew and K. Schmidt, "Jacob's ladder of density funcitonal approximations for the exchange-correlation energy", AIP Conference Proceedings **577**, 1–20 (2001).

[43]P. A. M. Dirac, "Quantum mechanics of many-electron systems", Proc. Royal Soc. (London) A **123**, 714–733 (1929).

[44]J. C. Slater, "A simplification of the hartree-fock method", Phys. Rev. **81**, 385–390 (1951).

[45]J. P. Perdew and Y. Wang, "Accurate and simple analytic representation of the electron-gas correlation energy", Phys. Rev. B **45**, 13244–13249 (1992).

[46]J. P. Perdew, K. Burke, and M. Ernzerhof, "Generalized gradient approximation made simple", Phys. Rev. Lett. **77**, 3865–3868 (1996).

[47]J. Tao, J. P. Perdew, V. N. Staroverov, and G. E. Scuseria, "Climbing the density functional ladder: nonempirical meta-generalized gradient approximation designed for molecules and solids", Phys. Rev. Lett. **91**, 146401 (2003).

[48]V. N. Staroverov, G. E. Scuseria, J. Tao, and J. P. Perdew, "Comparative assessment of a new nonempirical density functional: molecules and hydrogen-bonded complexes", J. Chem. Phys. **119**, 12129–12137 (2003).

[49]A. Mercy, "5 theoretical background and methods", (2019).

[50]K. L. et al., Science **351 (6280)**, 1415 (2016).

[51]G. Prandini, I. E. C. A. Marrazzo, N. Mounet, and N. Marzari, "Quantum espresso: a modular and open-source software project for quantum simulations of materials", npj Computational Materials 4 **72** (2018).

[52]M. Giantomassi and the AbiPy group, *Abipy*, `https://abinit.github.io/abipy/index.html`, (accessed: 01.06.2020).

[53]J. G. C. Milne, "Superconducting transition temperature of high-purity tantalum metal", Phys. Rev. **122**, 387–388 (1961).

[54]J. D. Zhang and X. Y. Huang, "Theoretical investigations of structural, electronic and elastic properties of U2S3type Nb2N3under high pressure", Phys. B Condens. Matter **456**, 5–8 (2015).